

An isolated mass gap black hole or neutron star detected with astrometric microlensing

CASEY Y. LAM,¹ JESSICA R. LU,¹ ANDRZEJ UDALSKI,^{2,*} IAN BOND,^{3,†} DAVID P. BENNETT,^{4,5,†} JAN SKOWRON,^{2,*}
PRZEMEK MRÓZ,^{2,*} RADEK POLESKI,^{2,*} TAKAHIRO SUMI,^{6,†} MICHAŁ K. SZYMAŃSKI,^{2,*} SZYMON KOZŁOWSKI,^{2,*}
PAWEŁ PIETRUKOWICZ,^{2,*} IGOR SOSZYŃSKI,^{2,*} KRZYSZTOF ULACZYK,^{2,7,*} ŁUKASZ WYRZYKOWSKI,^{2,*} SHOTA MIYAZAKI,^{6,†}
DAISUKE SUZUKI,^{6,†} NAOKI KOSHIMOTO,^{4,5,8,†} NICHOLAS RATTENBURY,^{9,†} MATTHEW W. HOSEK, JR.,¹⁰ FUMIO ABE,^{11,†}
RICHARD BARRY,^{4,†} APARNA BHATTACHARYA,^{4,5,†} AKIHIKO FUKUI,^{12,13,†} HIROSANE FUJII,^{11,†} YUKI HIRAO,^{6,†}
YOSHITAKA ITOW,^{11,†} RINTARO KIRIKAWA,^{6,†} IONA KONDO,^{6,†} YUTAKA MATSUBARA,^{11,†} SHO MATSUMOTO,^{6,†}
YASUSHI MURAKI,^{11,†} GREG OLMSCHENK,^{4,†} CLÉMENT RANC,^{14,†} ARISA OKAMURA,⁶ NICHOLAS J. RATTENBURY,^{9,†}
YUKI SATOH,⁶ STELA ISHITANI SILVA,^{15,4,†} TAIGA TODA,^{6,†} PAUL J. TRISTRAM,^{16,†} AIKATERINI VANDOROU,^{4,5,†}
HIBIKI YAMA,^{6,†} NATASHA S. ABRAMS,¹ SHRIHAN AGARWAL,¹ SAM ROSE,¹ AND SEAN K. TERRY¹

¹University of California, Berkeley, Department of Astronomy, Berkeley, CA 94720

²Astronomical Observatory, University of Warsaw, Al. Ujazdowskie 4, 00-478 Warszawa, Poland

³School of Natural and Computational Sciences, Massey University, Private Bag 102-904 North Shore Mail Centre, Auckland 0745, New Zealand

⁴Code 667, NASA Goddard Space Flight Center, Greenbelt, MD 20771, USA

⁵Department of Astronomy, University of Maryland, College Park, MD 20742, USA

⁶Department of Earth and Space Science, Graduate School of Science, Osaka University, Toyonaka, Osaka 560-0043, Japan

⁷Department of Physics, University of Warwick, Gibbet Hill Road, Coventry, CV4 7AL, UK

⁸Department of Astronomy, Graduate School of Science, The University of Tokyo, 7-3-1 Hongo, Bunkyo-ku, Tokyo 113-0033, Japan

⁹Department of Physics, University of Auckland, Private Bag 92019, Auckland, New Zealand

¹⁰University of California, Los Angeles, Department of Astronomy, Los Angeles, CA 90095, USA

¹¹Institute for Space-Earth Environmental Research, Nagoya University, Nagoya 464-8601, Japan

¹²Department of Earth and Planetary Science, Graduate School of Science, The University of Tokyo, 7-3-1 Hongo, Bunkyo-ku, Tokyo 113-0033, Japan

¹³Instituto de Astrofísica de Canarias, Vía Láctea s/n, E-38205 La Laguna, Tenerife, Spain

¹⁴Zentrum für Astronomie der Universität Heidelberg, Astronomisches Rechen-Institut, Mönchhofstr. 12-14, 69120 Heidelberg, Germany

¹⁵Department of Physics, The Catholic University of America, Washington, DC 20064, USA

¹⁶University of Canterbury Mt. John Observatory, P.O. Box 56, Lake Tekapo 8770, New Zealand

(Received; Revised; Accepted)

Submitted to

ABSTRACT

We present the analysis of five black hole (BH) candidates identified from gravitational microlensing surveys. HST astrometric data and densely sampled lightcurves from ground-based microlensing surveys are fit with a single-source, single-lens microlensing model in order to measure the mass and luminosity of each lens and determine if it is a black hole. One of the five targets (OGLE-2011-BLG-0462/MOA-2011-BLG-191 or OB110462 for short) shows a significant > 1 mas coherent astrometric shift, little to no lens flux, and has an inferred lens mass of $1.6 - 4.2 M_{\odot}$. This makes OB110462 the first definitive discovery of a compact object through astrometric microlensing and it is most likely either a neutron star or a low-mass black hole. This compact object lens is relatively nearby (690 - 1370 pc) and has a slow transverse motion of < 25 km/s. OB110462 shows significant tension between models well-fit to photometry vs. astrometry, making it currently difficult to distinguish between a neutron star and a black hole. Additional observations and modeling with more complex system geometries, such as binary sources are needed to resolve the puzzling nature of this object. For the remaining four candidates, the lens masses are $< 2M_{\odot}$ and they are unlikely to be black holes; but two of the four

are likely white dwarfs or neutron stars. We compare the full sample of 5 candidates to theoretical expectations on the number ($\sim 10^8$) of BHs in the Milky Way and find reasonable agreement given the small sample size.

1. INTRODUCTION

Stellar-mass black holes are produced when massive stars collapse under their own gravity. Observations of black holes (BHs) are a key ingredient for understanding outstanding questions in massive stellar evolution, such as which stars explode, which stars produce neutron stars vs. BHs, and whether there is a gap between the heaviest neutron stars and the lightest BHs.

Back-of-the-envelope calculations predict $\sim 10^8$ BHs in the Milky Way (Shapiro & Teukolsky 1983). Other estimates using supernovae and galactic chemical evolution models (Samland 1998; Timmes et al. 1996) or photometric microlensing (Agol et al. 2002; Sartore & Treves 2010) also predict $\sim 10^7 - 10^9$ BHs. Despite the large predicted number of BHs, only about two dozen have dynamical mass measurements (Corral-Santana et al. 2016; Thompson et al. 2019; Jayasinghe et al. 2021). These BHs are not a representative sample of the Galactic BH population, as they are all in binary systems.

While most massive stars exist in binary or multiple systems (Sana 2017), the majority of the BH population is expected to be isolated due to the disruption of the progenitor systems (Belczynski et al. 2004; Fender et al. 2013; Wiktorowicz et al. 2019). However, to date there are no confirmed isolated BH detections. Attempts have been made to detect X-rays from ISM accretion onto a BH, but they have been unsuccessful and even future X-ray missions may not be sensitive enough to make such a detection (Tsuna et al. 2018). As almost all other BH detection methods require a companion (e.g. X-ray binaries, astrometric binaries, gravitational waves), microlensing is the ideal way to detect and measure the masses of isolated BHs.

Paczynski (1986) first proposed monitoring the Galactic halo to search for the characteristic brightening of microlensing events to constrain the properties of dark massive compact halo objects (MACHOs). Several years later Paczynski (1991) and Griest et al. (1991) proposed monitoring the Galactic bulge for microlensing events, calculating a lensing rate of $\sim 10^{-6}$ /star/year. Presently, thirty years later, ground-based microlensing surveys such as OGLE (Udalski et al. 1994), MOA (Bond et al. 2001), and KMTNet (Kim et al. 2016) monitor hundreds of millions of stars toward the Galactic

bulge, identifying thousands of photometric microlensing events each year. Although microlensing has been used to try and detect BHs (e.g. Bennett et al. (2002); Mao et al. (2002); Wyrzykowski et al. (2016)), most searches only use photometry, which alone cannot constrain the mass of the lens objects, unless rare higher-order effects such as finite-source effects are detected.

As mentioned briefly at the end of Paczynski (1986), microlensing also has an astrometric signature, in which the centroid of the image is displaced from the source's true position (Hog et al. 1995; Miyamoto & Yoshii 1995; Walker 1995). In contrast to the now-routine measurements of photometric microlensing, detections of astrometric microlensing are still at the forefront of our technical capabilities. Typical astrometric shifts toward the Bulge are $O(0.01 - 1)$ mas, and few existing facilities are currently capable of the astrometric precision to perform this measurement. Only a handful of astrometric measurements of the gravitational deflection of light have ever been made, all for nearby (< 10 pc) lenses that were astrometrically anticipated (Eddington 1919; Sahu et al. 2017; Zurlo et al. 2018). However, a combination of photometric and astrometric microlensing together can determine the mass of the lensing object, making detection of astrometric microlensing important for BH searches.

To date, there have been two endeavors to measure lens masses by combination of photometric and astrometric microlensing. Lu et al. (2016) attempted a measurement with Keck LGS AO, but no detections of astrometric microlensing were made. Kains et al. (2017) reported a detection of astrometric microlensing with HST, but the signal was very weak and no lens masses were well constrained. The currently operating Gaia mission is also anticipated to make measurements of astrometric microlensing, which can be searched for once per-epoch astrometry is released (McGill et al. (2020) and references therein). A handful of these deflections should be due to BHs (Rybicki et al. 2018).

If there are $\sim 10^8$ BHs in the Milky Way, they should contribute only about 0.1% to stellar-mass Milky Way objects (stars, WDs, NSs, BHs). However, they make up around 1% of all Milky Way microlensing events due to their larger lensing cross section. Thus of the thousands of microlensing events detected each year, ten or so should be due to BHs (Gould 2000; Lam et al. 2020). However, this is like looking for BH needles in a Galactic haystack. By limiting to long duration microlensing

* OGLE collaboration

† MOA collaboration

events¹, the probability of a microlensing event being a BH rises to $\sim 40\%$ (Lam et al. 2020).

In this paper, we present an analysis of five BH candidates, which constitute a sufficient sample to place early constraints on the number of isolated black holes in the Milky Way. All five BH candidates were identified in ground-based microlensing surveys and followed up astrometrically with HST. The HST data is used to perform an astrometric analysis and then combined with MOA and OGLE photometry to fit the events and produce mass constraints on the lenses. By combining the mass, distance, and photometry constraints on the lenses with stellar evolution and Galactic models, we determine the probability that the lenses are stars, white dwarfs, neutron stars, or black holes. This is used to determine whether the number of BHs from this sample is consistent with a population of 10^8 Galactic BHs.

This paper is organized as follows. In §2, the datasets and reduction processes are described, and in §3 the photometric and astrometric analysis of the HST data is explained. In §4, the microlensing modeling and fitting procedure are described, and §5 presents the results of those fits, in particular the inferred lens masses for the five candidates. Constraints on the Milky Way BH population and future BH microlensing searches are discussed in §6. Conclusions are presented in §7.

2. OBSERVATIONS

2.1. Targets and Selection Criteria

Five targets² were selected from the OGLE Early Warning System³ (Udalski et al. 2015) and MOA Alerts⁴ to be imaged with HST. These targets were selected to have long ($t_E > 200$ days) duration, no light contribution from the lens, and high amplifications to allow detection of parallax signals, making them good isolated BH candidates (Sahu 2009). Three of the targets, OGLE-2011-BLG-0037/MOA-2011-BLG-039, OGLE-2011-0310/MOA-2011-BLG-332, and OGLE-2011-BLG-0462/MOA-2011-BLG-191 (hereafter OB110037, OB110310, and OB110462), were alerted by both OGLE and MOA. The other two targets, MOA-2009-BLG-260 and MOA-2010-BLG-364 (hereafter MB09260 and MB10364), were only alerted by MOA. Table 1 lists their coordinates. Figures 3 - 8 show the lightcurves of the targets.

¹ Einstein crossing times $t_E > 120$, see §4.1 for the definition of t_E .

² Three additional other targets were initially observed with HST, but dropped from the target list after a year (Sahu 2012).

³ <http://ogle.astrouw.edu.pl/ogle4/ews/ews.html>

⁴ <https://www.massey.ac.nz/~iabond/moa/alerts/>

2.2. MOA

The MOA-II survey is carried out with a 1.8-m telescope at Mt. John University Observatory in New Zealand (Hearnshaw et al. 2006; Sumi 2008). The median seeing at the site is $\sim 2.5''$. The telescope has a 2.2 deg^2 FOV, with a 10-chip CCD camera with a plate scale $0.57''/\text{pixel}$. The main observations are taken using the MOA-Red (630-1000 nm) filter (Bond et al. 2001).

MOA data for MB09260 and MB10364 were reduced as described in Sumi et al. (2011) and Bond et al. (2001).⁵ The MOA lightcurves are photometrically calibrated to the OGLE-III I-band.

2.3. OGLE

The OGLE-IV survey is carried out at the 1.3-m Warsaw telescope at Las Campanas Observatory in Chile (Udalski et al. 2015). The median seeing at the site is $\sim 1.3''$. The telescope has a 1.4 deg^2 FOV, with a 32-chip CCD camera with a plate scale of $0.26''/\text{pixel}$. The main observations are taken using the OGLE-I filter, which is similar to Cousins I-band. The data was reduced using the Difference Image Analysis technique as implemented by Wozniak (2000).

OGLE data is only available for OB110037, OB110310, and OB110462. The magnification of MB09260 was not observed by OGLE as it occurred during the OGLE-III to OGLE-IV upgrade. MB10364 is located in a gap in the detectors of the OGLE camera.

2.4. HST

HST observations come from a multi-year campaign following up these five targets (GO-11707, GO-12322, GO-12670, GO-12986, GO-13458, GO-14783; PI: K. C. Sahu). Observations were taken with the UVIS channel on the Wide Field Camera 3 (WFC3) in two different wide-band filters, F606W (V-band) and F814W (I-band). Table 3 summarizes the HST observations.

The WFC3 UVIS channel is composed of two $2k \times 4k$ CCDs and has a $162'' \times 162''$ field of view with a plate scale $0.04''/\text{pixel}$. WFC3 UVIS supports sub-arraying, in which only a portion of the entire detector is read out, which can reduce data volume or exposure time and increase observational efficiency. All observations prior to 2011-07-22 were taken with the UVIS1-2K4-SUB subarray mode. Beginning HST Cycle 18, more subarray sizes were made available, and observations after 2011-07-22

⁵ OB110037, OB110310, and OB110462 also have MOA lightcurves. For simplicity we only present the OGLE lightcurve fits for those events, since the seeing at OGLE is better. However, we use the MOA lightcurves to validate our results.

Table 1. Target Summary

Short Name	OGLE Alert Name	MOA Alert Name	RA (2000)	Dec (2000)
MB09260	–	MOA-2009-BLG-260	17:58:28.561	-26:50:20.88
MB10364	–	MOA-2010-BLG-364	17:57:05.401	-34:27:05.01
OB110037	OGLE-2011-BLG-0037	MOA-2011-BLG-039	17:55:55.83	-30:33:39.7
OB110310	OGLE-2011-BLG-0310	MOA-2011-BLG-332	17:51:25.39	-30:24:35.0
OB110462	OGLE-2011-BLG-0462	MOA-2011-BLG-191	17:51:40.19	-29:53:26.3

were taken with the UVIS2-2K2C-SUB subarray mode, a 2k×2k subarray.

Additional observations of OB110462 commenced in Cycle 29 (GO-16760; PI: C. Lam). These were taken in as similar a configuration as possible to the later epochs of the archival program, using WFC3 UVIS in UVIS2-2K2C-SUB subarraying mode, with observations in F606W and F814W filters. The first set of observations from this program was taken October 2021 and is presented here; an additional set of observations is anticipated to be taken Fall 2022 (Lam & Lu 2021a).

2.5. *Gaia*

Gaia is an all-sky scanning astrometric space mission (Gaia Collaboration et al. 2016). All of the targets, with the exception of OB110462, are found in Gaia Early Data Release 3 (EDR3, Table 2). Gaia EDR3 covers the period from 25 July 2014 to 28 May 2017 (Gaia Collaboration et al. 2020). MB10364, OB110037, and OB110310 have proper motions and parallaxes, while MB09260 does not. OB110462 was not in Gaia as it is too faint. We note that there is a Gaia source located $\sim 0.35''$ away from OB110462 (Gaia EDR3 Source ID 4056442477683080960), which coincides with the bright star directly west of the target seen in the HST images (Figure 1).

3. HST DATA ANALYSIS

3.1. *Reduction*

The HST archival data was accessed from the Mikulski Archive for Space Telescopes⁶ (MAST) in June 2021. The Cycle 29 data was accessed October 2021. For the following analysis, we employed the calibrated, flat-fielded, individual exposures corrected for charge transfer efficiency (CTE, HST files with suffix `_flc`⁷). The archival data was processed with Version 3.6.0 (Dec-31-2020) of the `calwf3` pipeline, using Version 2.0 of the CTE correction algorithm.

⁶ <https://archive.stsci.edu/hst/>

⁷ See Gennaro (2018) for a full description of the different file name suffixes.

CTE can alter astrometry at the milliarcsecond level, hence it is important to use `_flc` files. However, even the `_flc` files do not necessarily fix all problems associated with CTE (Kuhn & Anderson 2021). Exploration of other methods of CTE correction will be explored in future work. At the present we mitigate CTE effects via other methods (§3.2.2) and validate our astrometry to ensure it is not distorted by CTE.

Images were converted into calibrated star lists via the following steps.

1. *Star list extraction from individual frames.* Star lists were extracted from the individual `_flc` exposures by modeling the PSFs of sources with `hst1pass`, an updated version of the software described in Anderson & King (2006). Empirical filter-dependent PSF models as described in Anderson (2016) and geometric distortion solutions as described in Bellini et al. (2011) were used when performing source extraction with `hst1pass`.
2. *Combined star list for one epoch.* Within a single epoch and filter, multiple star lists were aligned to a common coordinate system in an iterative manner using `xym2mat` and `xym2bar` (Anderson & King 2006), which include the distortion solution for the WFC3 camera and filters (Bellini et al. 2011) to produce a single matched star list.
3. *Photometric calibration.* Lastly, a zero-point is applied to the star lists to convert from instrumental to Vega magnitudes. Star lists were calibrated against photometrically calibrated star lists on the Hubble Legacy Archive, Data Release 10 (HLA DR10). A magnitude offset is applied later during the astrometric alignment (§3.3) to obtain more precise relative photometry.

Note that data taken in F606W and F814W filters are treated as independent measurements. That is, observations taken on the same date are treated as distinct epochs, and are not combined into a single star list, as the importance of filter dependence in astrometry is not

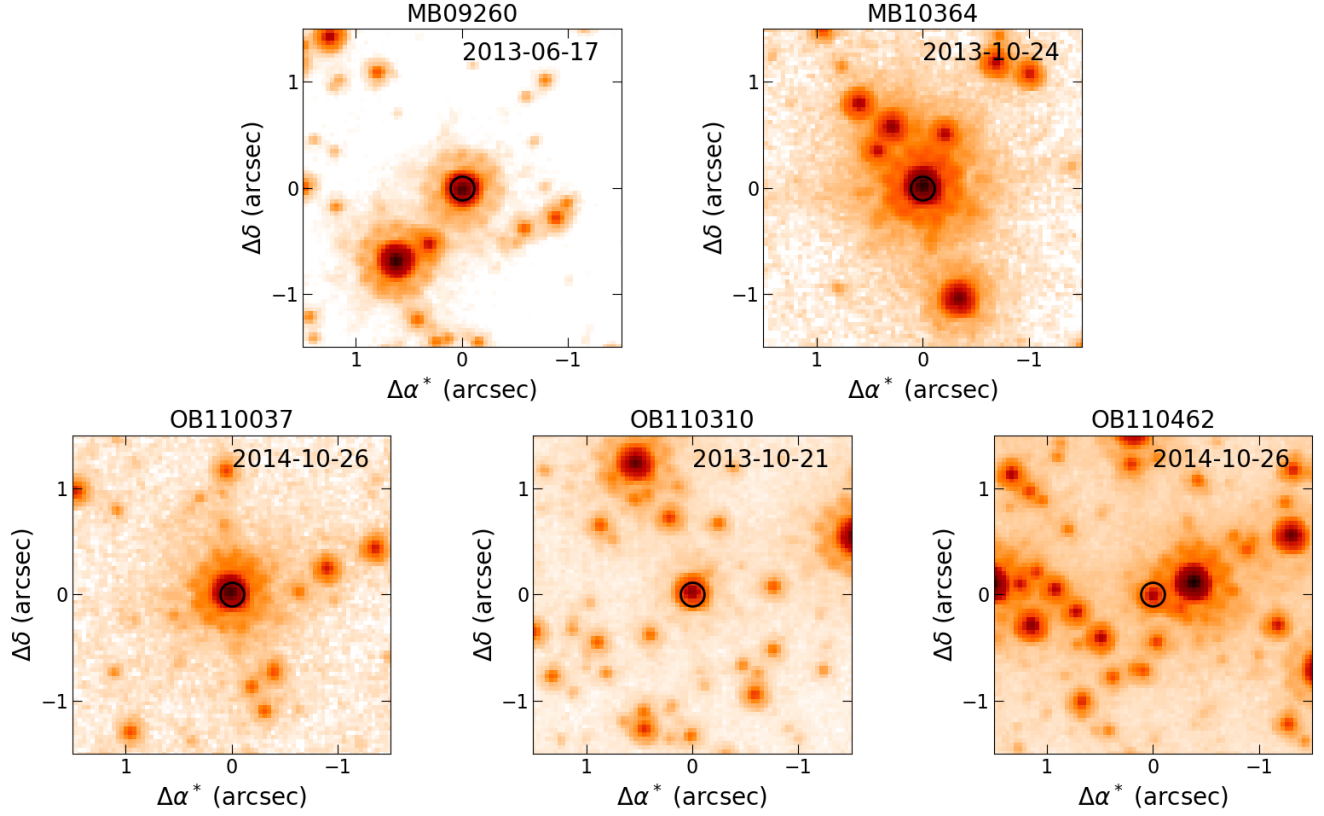


Figure 1. Central $3'' \times 3''$ of HST WFC3-UVIS F814W combined images of the observed fields, centered on the target (circled). These images are of the target at or near baseline, i.e. unmagnified. The color stretch is logarithmic. Note that the color scale is not the same across panels.

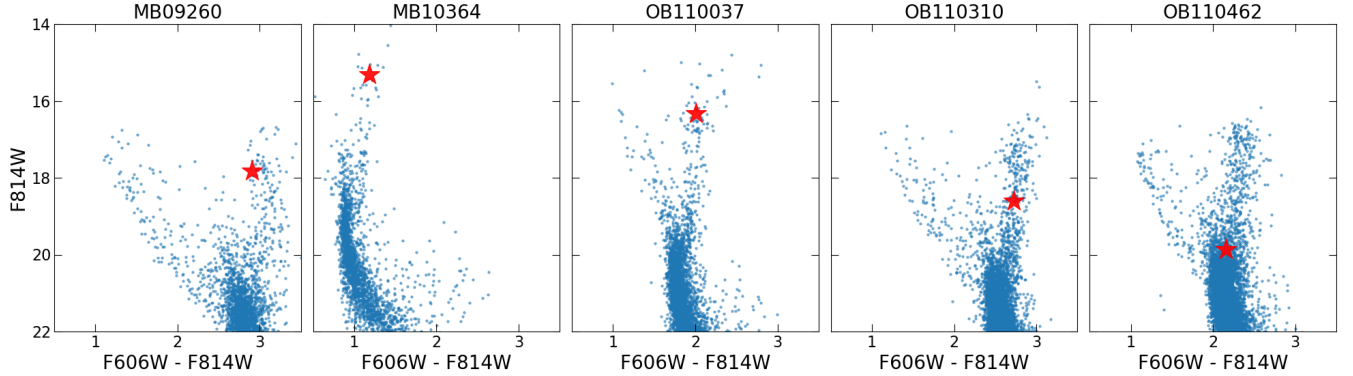


Figure 2. CMDs for each field. The target at baseline magnitude and color is marked as a red star.

well established. See §3.2.5 and Appendix I for further details.

Certain epochs were excluded from the analysis; these are marked with an asterisk in Table 3. The reason for their exclusion is detailed as follows.

- *Epochs with only a single frame.* Observations with only a single frame per filter cannot pro-

duce any useful photometric or astrometric constraints using `hst1pass`. This is the case for the MB09260 2009-10-01 F814W and 2009-10-19, 2010-03-22, and 2010-06-14 F606W epochs. In the MB09260 2010-10-20 F606W epoch, a cosmic ray in one of the exposures interfered with the extraction of the target, effectively leaving only a single usable frame.

Table 2. Gaia EDR3 Values

Parameter	MB09260	MB10364	OB110037	OB110310
Source ID	4064007633015639552	4042290560398692096	4056117808133831936	4056344036933003264
RA (deg)	269.619073405 \pm 7.3e-07	269.272538687 \pm 1.9e-08	268.982636391 \pm 3.0e-08	267.855757518 \pm 2.3e-07
Dec (deg)	-26.839323825 \pm 5.9e-07	-34.451415987 \pm 1.5e-08	-30.561059419 \pm 2.5e-08	-30.409776355 \pm 1.7e-07
$\mu_{\alpha*}$ (mas/yr)	–	-7.43 \pm 0.08	2.40 \pm 0.13	-2.08 \pm 1.12
μ_{δ} (mas/yr)	–	-6.80 \pm 0.05	-3.91 \pm 0.09	-6.75 \pm 0.58
π (mas)	–	0.40 \pm 0.08	0.15 \pm 0.13	0.54 \pm 1.16
ZP-corrected π (mas)	–	0.43	0.19	0.53*
G (mag)	19.216 \pm 0.004	16.086 \pm 0.002	17.477 \pm 0.001	20.051 \pm 0.010
RP (mag)	–	14.929 \pm 0.009	16.323 \pm 0.010	–
BP (mag)	–	16.557 \pm 0.011	19.049 \pm 0.032	–
ipd_gof_harmonic_amplitude	0.089	0.064	0.036	0.042
ipd_frac_multi_peak	0	15	0	0
ipd_frac_odd_win	18	0	0	55
ruwe	–	1.388	0.971	0.981
astrometric_excess_noise (mas)	1.241	0.406	0.000	0.894
astrometric_excess_noise_sig	2.657	12.020	0.000	0.332
astrometric_params_solved	3	95	31	95
phot_bp_rp_excess_factor	–	1.69	1.39	–

NOTE— Magnitude uncertainties are estimated from the Gaia reported flux errors. ZP correction comes from [Lindegren et al. \(2021a\)](#), * denotes values that are extrapolations. For full descriptions we refer the reader to Gaia EDR3 documentation ([van Leeuwen et al. 2021](#)), Section 13.1.1 `gaia_source`. OB110462 is not in Gaia.

- *Multiple exposure times.* Although in principle mixing multiple exposure times in a single epoch is possible, in practice it makes the uncertainties worse. This is likely due to issues with imperfect CTE correction in the `_f1c` files. For epochs where there were multiple exposure times, the combination that resulted in the smallest astrometric uncertainties were selected. Based on this criterion, some frames from the MB09260 2009-10-01 F606W, MB10364 2010-09-13 F814W, OB110037 2011-08-15 F814W, OB110310 2013-10-21 F814W, and OB110462 2011-08-08 F606W and F814W epochs were not used.
- *Saturation of target.* No useful astrometric limits can be placed when the target is saturated. The target is saturated in both filters in the MB10364 2011-04-13 and 2011-07-22 epochs.
- *Telescope pointing issues.* The observations of OB110462 on 2017-08-11 suffered a telescope drifting issue, resulting in streaked images.
- *Astrometric alignment systematics.* Although there are no standalone issues with the observations of OB110462 on 2013-05-13, astrometric systematics are apparent in the reference stars when this epoch is astrometrically aligned along with the other epochs using the methodology described

in §3.2. This is due to the difference in position angle of the observations taken, as the 2013-05-13 epoch was taken at PA = 99.9 deg, while all the other epochs were taken with a PA different by ~ 180 deg, with PA = 255.2 - 276.1 deg. Thus, the 2013-05-13 epoch is left out of the analysis.

The other targets (MB09260, OB110037, OB110310) with ~ 180 deg differences in PA across observations do not suffer this same problem, as there are multiple observations at each PA. This allows the systematics due to the ~ 180 deg PA flip to be calibrated out during the astrometric alignment.

3.2. HST Astrometric Analysis

The positional measurements extracted from the different epochs of HST data (§3.1) must be transformed into a common reference frame in order to derive the motion of the target. This is an iterative process, with multiple “passes” at refining the reference frame, allowing for the best relative astrometry possible to be extracted. We follow a similar procedure as described in §4.2 of [Lu et al. \(2016\)](#). The final positions and magnitudes of the targets resulting from the analysis in this section is presented in Table 7. The photometry is shown in Figures 3 - 8 and the astrometry is shown in Figures 13 - 18.

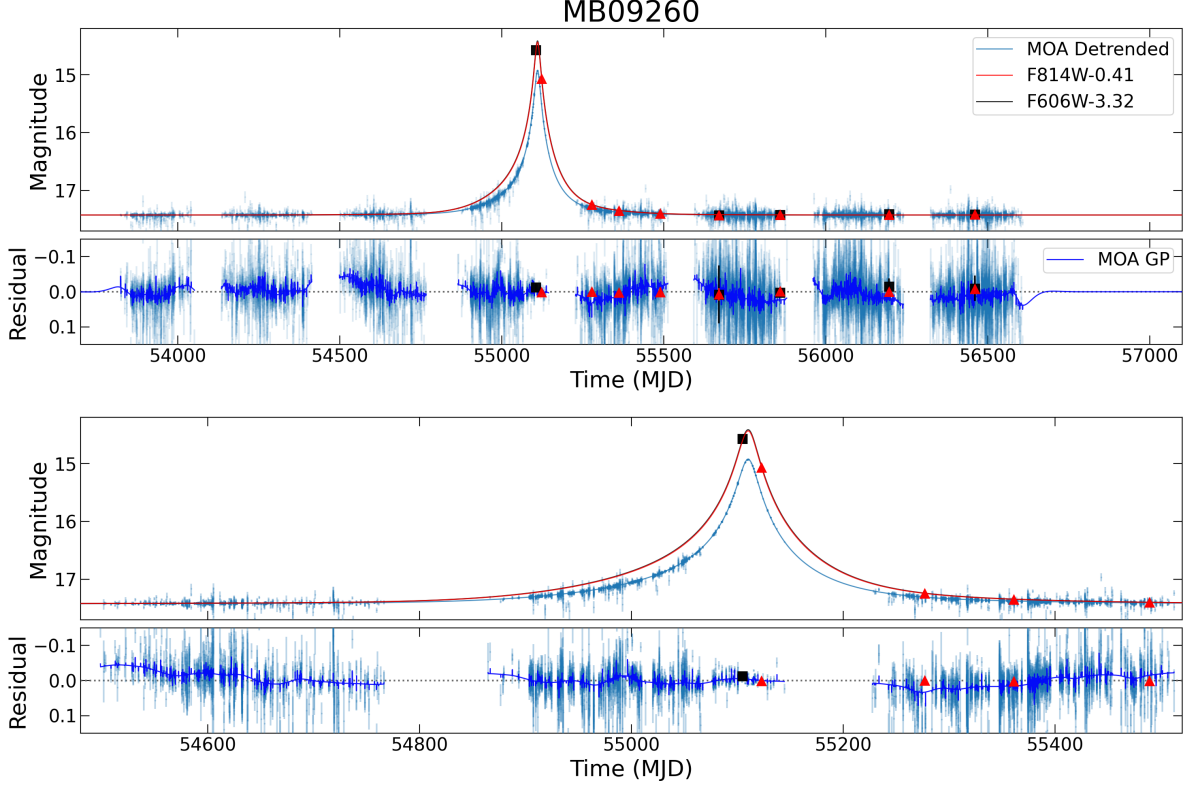


Figure 3. (*Top panel:*) MB09260 lightcurve, as seen by MOA and HST F814W and F606W. The maximum likelihood model (described in Section 5) is plotted over the data. (*Second from top panel:*) The best-fit model residual. In the top panel, the MOA data has been detrended, while in the bottom the Gaussian Process is plotted on top of the residual. We emphasize the residual is not independently fit by the Gaussian Process, but is simultaneously fit with the model parameters; this is purely to visualize the data (also see Golovich et al. (2020)). See §4 for more details about the fitting procedure. (*Second from bottom panel:*) Same as top panel, but zoomed into the three most magnified years. (*Bottom panel:*) Same as second from top panel, but zoomed into the three most magnified years.

3.2.1. Alignment procedure

Following standard image processing techniques, a 2-D polynomial transformation of the form

$$x' = a_0 + a_1x + a_2y + a_3x^2 + a_4xy + a_5y^2 + \dots \quad (1)$$

$$y' = b_0 + b_1x + b_2y + b_3x^2 + b_4xy + b_5y^2 + \dots \quad (2)$$

is applied to the images in order to match them to a reference image. A first order 2-D polynomial transformation ($x' = a_0 + a_1x + a_2y$; $y' = b_0 + b_1x + b_2y$) is an affine transformation⁸, which can be used to model translation, rotation, scaling, and shearing introduced by the camera. A higher-order polynomial can correct for additional distortions, but going beyond second order generally does not improve results as the number of

free parameters quickly increases and results in overfitting.

In the first pass, the HST images are aligned to the absolute reference frame of Gaia with a first order 2-D polynomial transformation to roughly establish the transformation. The Gaia EDR3 catalog is matched to the HST catalog using the pattern matching algorithm of Groth (1986).

In subsequent passes, the HST images are aligned to themselves, using a 2-D polynomial transformation going up to second order. It is empirically determined that 3-4 passes gives optimal results. In each successive pass, the HST images are aligned to the reference frame derived in the previous pass, which continually refines the reference frame and derived proper motions.

To calculate the optimal transformation, a set of reference stars $r_{ref}^R(t_0)$ are selected from the stars in reference frame $R(t_0)$ observed at time t_0 . The reference stars $r_{ref}^R(t_0)$ are matched to corresponding stars $u_{ref}^U(t)$ in the untransformed $U(t)$ frame observed at time t . The transformation $T : U(t) \rightarrow R(t)$ is found

⁸ An affine transformation maps points to points, lines to lines, planes to planes, and so on. Affine transformations preserve collinearity and ratios of distances. Parallel lines also remain parallel after an affine transformation.

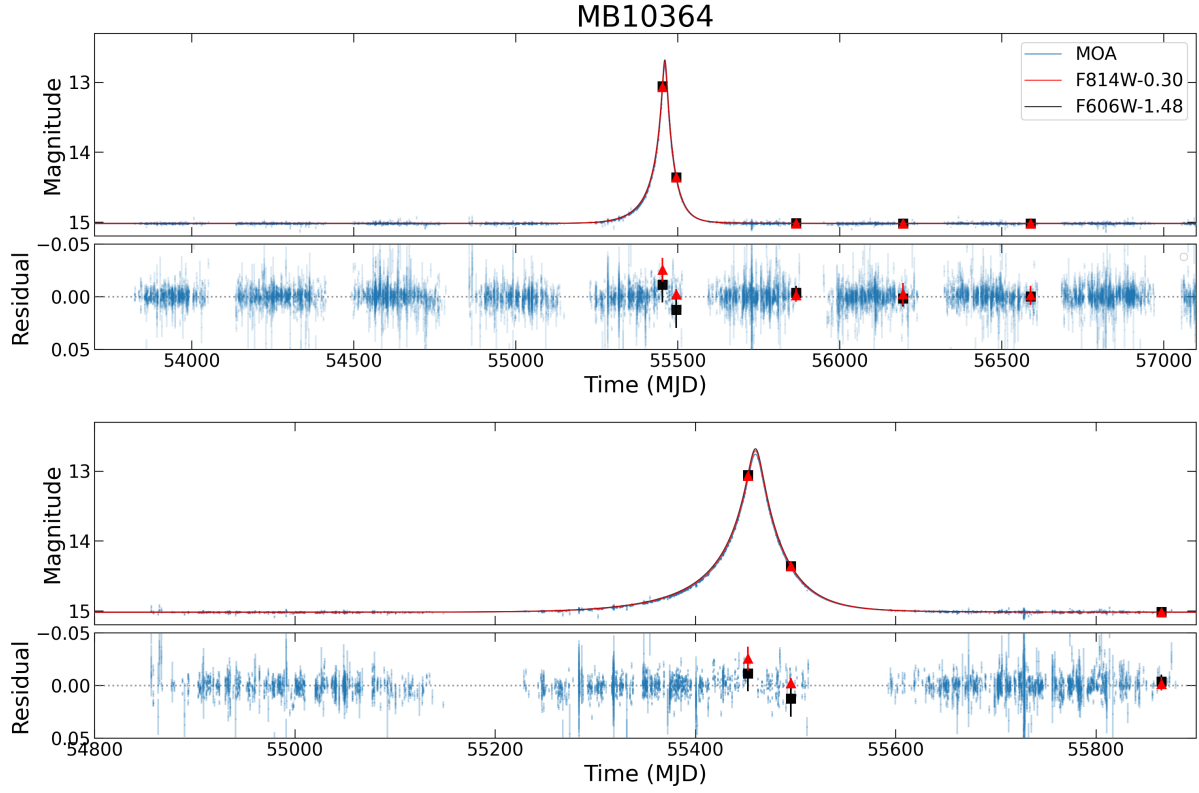


Figure 4. Same as Figure 3, but for MB10364. Note we do not include GP in the MB10364 fit.

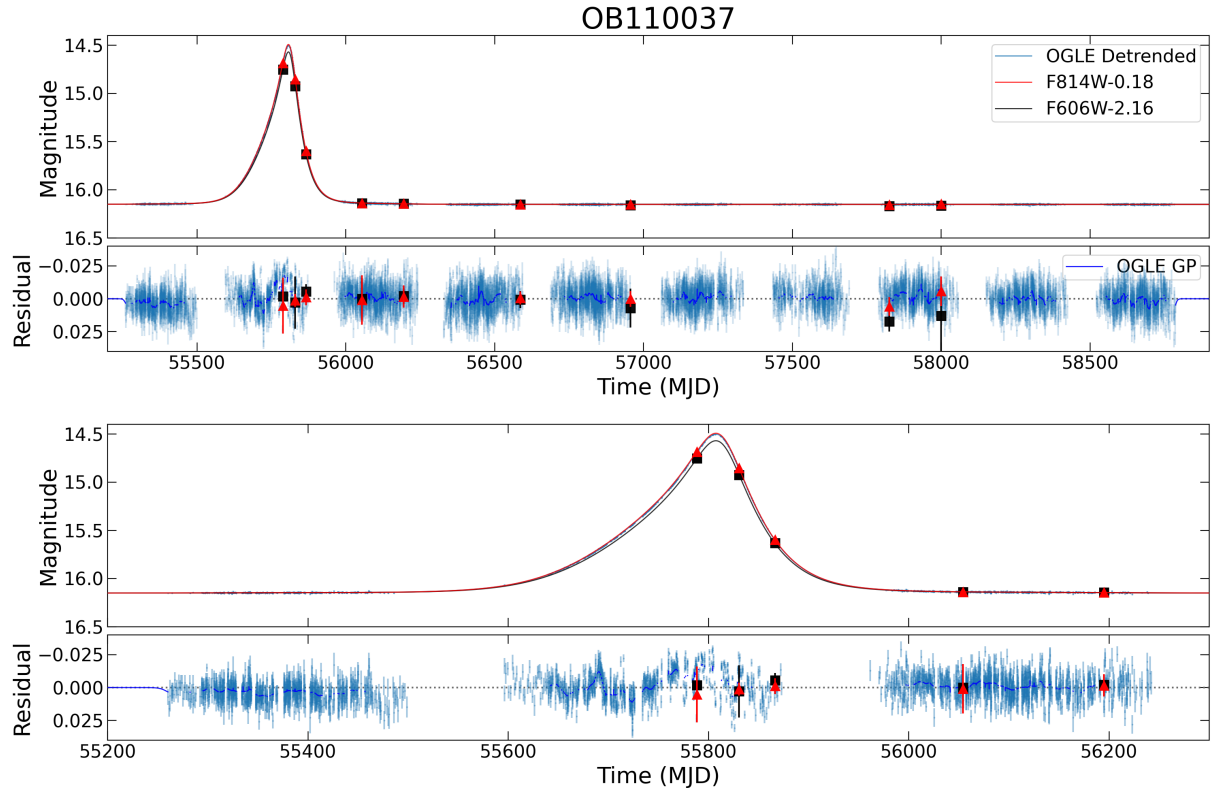


Figure 5. Same as Figure 3, but for OB110037. Instead of MOA data, it is OGLE data.

by least-squares minimization of the x and y position residuals from the alignment

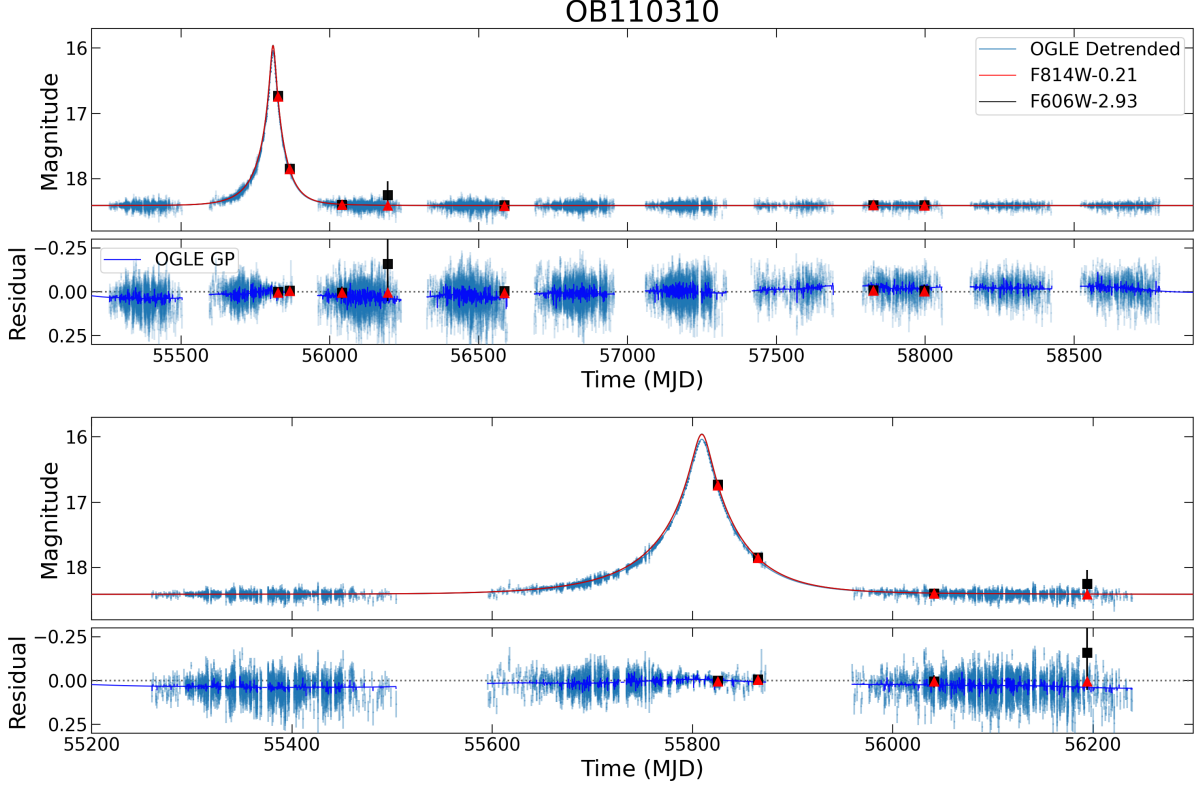


Figure 6. Same as Figure 5, but for OB110310.

$$x_{res} = \sum_i w_{x,i} (x_{r,i}^R(t) - T(x_{u,i}^U(t)))^2 \quad (3)$$

$$y_{res} = \sum_i w_{y,i} (y_{r,i}^R(t) - T(y_{u,i}^U(t)))^2 \quad (4)$$

where $w_{(x,y),i}$ is the weight for the i -th reference star, $(x^R(t)_{r,i}, y^R(t)_{r,i})$ and $(x^U(t)_{u,i}, y^U(t)_{u,i})$ are the positions of the stars in the reference $R(t)$ and untransformed $U(t)$ frames at time t . The positions of the reference stars $r_{ref}^R(t)$ in the reference frame R at time t are propagated from time t_0 using the proper motions

$$x_{r,i}^R(t) = x_{r,i}^R(t_0) + v_{x,r,i}^R(t - t_0) \quad (5)$$

$$y_{r,i}^R(t) = y_{r,i}^R(t_0) + v_{y,r,i}^R(t - t_0) \quad (6)$$

where $v_{(x,y),r,i}^R$ are the proper motions of the i -th reference stars in reference frame R . After the transformation T is derived, it is applied to all the stars u^U in the U frame to obtain a transformed star list $u^R(t) = T(u^U(t))$, where the stars $u^R(t)$ are now in the frame R . This yields starlists for all N epochs $u_1^R(t_1), \dots, u_N^R(t_N)$, where the positions of all the stars are now in the same reference frame R . For each star j , a proper motion is derived by finding the best-fit straight

line via non-linear least squares through the $n \leq N$ observations.⁹

Lu et al. (2016) examined several different weighting schemes and showed that the resulting astrometry is not affected. As we assume our data has Gaussian uncertainties, we choose to use weights $w_{(x,y),i} = 1/\sigma_{(x,y),i}$, where $\sigma_{(x,y),i}$ are the positional uncertainties of the stars in the untransformed frame. Instead of directly using the positional uncertainties returned by `hst1pass`, we used the error on the mean, with an additional additive error empirically determined during the astrometric alignment process. The uncertainties, as well as the procedure used to determine them, are detailed in Appendix A.

As we are interested in the astrometry of the target, the target itself is not used to establish the transformation into a common reference frame (§3.2.2) nor to judge the quality of the final transformation (Figure 9).

3.2.2. Reference star selection

Reference stars are stars assumed to have linear proper motions, which are used to derive the reference frame transformation and the motions of the other stars. The

⁹ Some stars are not detected in all epochs, which is why it is possible to have $n < N$ observations.

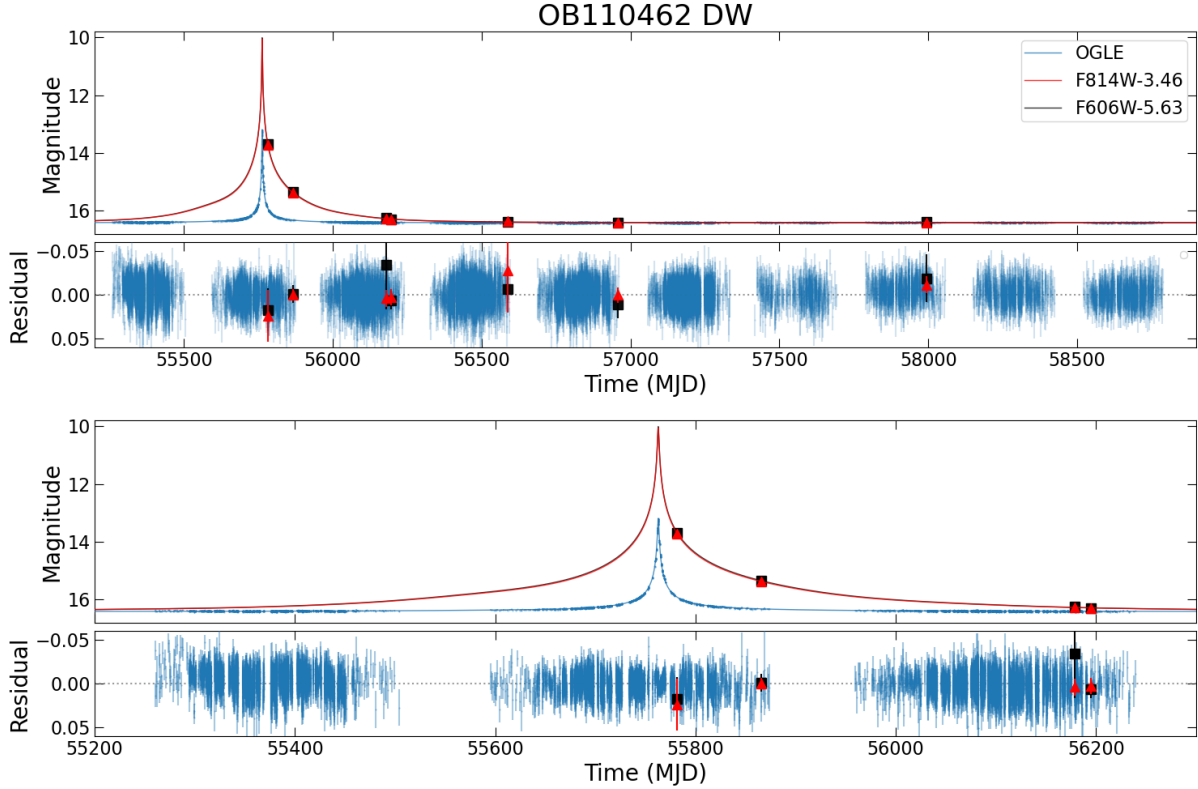


Figure 7. Same as Figure 5, but for OB110462. This maximum likelihood model was calculated using the default weighted likelihood described in §4.3.

selection of reference stars is an art that depends on multiple considerations, such as the stellar density, amount of geometric distortion, instrumental systematics, number and brightness of targets of interest, to name a few. The goal is to balance having enough stars to establish the reference frame, while excluding stars which would produce a non-stable reference frame. The criteria for reference star selection for each target is summarized in Table 5. We choose reference stars with brightness similar to the target, relatively large radial separations from our target of interest, and exclude likely foreground stars. We detail the reasoning for these choices below.

Brightness range: Due to the nature of CTE, there are strong magnitude-dependent astrometric residuals, even when using the latest CTE-corrected `_flc` images. However, this is not unexpected (Kuhn & Anderson 2021). For this reason, stars are chosen to be in a brightness range similar to the one spanned by the target as narrow as possible. For OB110310 and OB110462, which are relatively faint and where there are many stars of similar brightness, all stars falling within ± 0.1 mag of the target’s brightest and faintest in the HST data are used. MB09260, on the other hand, is brighter, with less stars of similar brightness, so the range is larger, with all stars falling within ± 1 mag of the target’s brightest and

faintest in the HST data are used. MB10364 is so bright that many stars of comparable brightness are saturated in the longer exposures. Because of this, only bright ($F814W < 18.0$, $F606W < 19.2$) and unsaturated stars were selected; the bright limit on the magnitude range differs between epochs because of the different exposure times.

Spatial separation: Only reference stars within $30''$, or $20''$ for the denser field around OB110462, are used as reference stars. This minimizes the impact of geometric distortion residuals and spatially dependent PSF variations.

Foreground stars: A key assumption in the astrometric alignment process is that reference stars have linear proper motions, and parallax effects are ignored. For a typical bulge star 8 kpc from Earth, this is a reasonable assumption as the parallax will be $1/8000$ arcsec = 0.125 mas, below our achievable astrometric precision. However, for nearby stars, ignoring parallax is an issue when trying to derive an accurate transformation. As all the target fields are toward the highly extincted Galactic bulge, bright blue stars as identified on a CMD (Figure 2) are likely to be nearby and have a non-negligible parallax, and are excluded from the set of reference stars. The color-magnitude exclusion criteria are listed in the

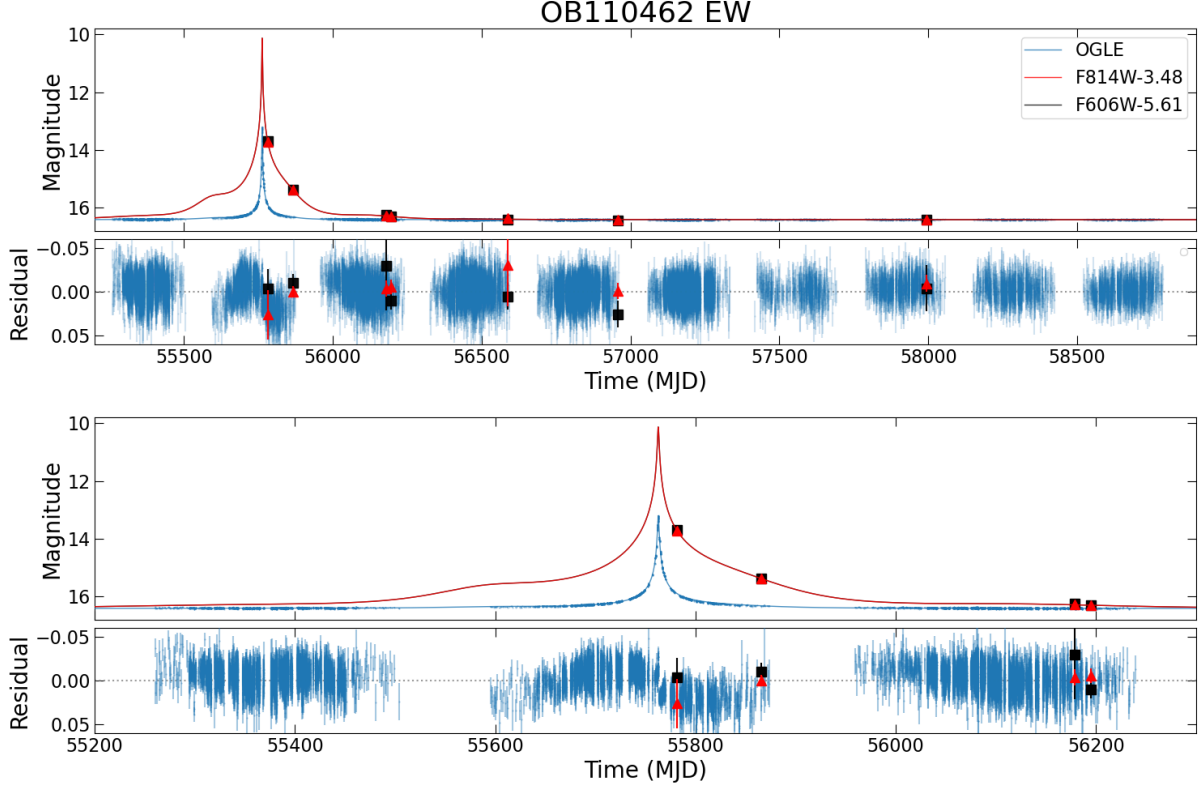


Figure 8. Same as Figure 5, but for OB110462. This maximum likelihood model was calculated using the equal weight likelihood described in §4.3.

last column of Table 5. For MB10364, no bright blue stars were removed as reference stars, as all the observations came from within 6 weeks of the same time of year. Hence, any type of yearly parallax signal would be negligible within this time span.

Number of detections: We require reference stars to be detected in most, if not all, epochs. If there are N_{ep} total epochs, we require reference stars to be detected in $N_{\text{ep,detect}} = N_{\text{ep}} - 2$ epochs.

Lastly, as the motion of the target is the quantity we are interested in, we do not use it as a reference star.

3.2.3. Derived stellar proper motions

To evaluate the goodness of the fits of the derived stellar proper motions, we consider the χ^2 distributions of the position residuals

$$\chi_x^2 = \sum_t \left(\frac{x_t - x_{t,\text{fit}}}{\sigma_{x_t}} \right)^2 \quad (7)$$

$$\chi_y^2 = \sum_t \left(\frac{y_t - y_{t,\text{fit}}}{\sigma_{y_t}} \right)^2 \quad (8)$$

where $x \equiv \text{RA}$, $y \equiv \text{Dec}$, $(x, y)_t$ are the positions in the data, $(x, y)_{t,\text{fit}}$ are the positions as derived from the linear motion fit, and $\sigma_{(x,y),t}$ are the positional uncertainties at time t . The distributions of χ_x^2 and χ_y^2 for the

reference stars detected in all epochs N_{ep} are shown in Figure 9, with the expected χ^2 distribution overplotted on top. The distributions for the positions in F814W and F606W are shown separately. The expected residual distribution has $N_{\text{ep,detect}} - 2$ degrees of freedom, as there are two free parameters in the linear motion fit (initial position and proper motion). Note that unlike Gaia, this linear model fit does not include parallax. Parallax is included only in the full modeling with microlensing.

3.2.4. OB110462 bias correction

There is a bright star (“the neighbor”) ~ 10 pixels (~ 0.4 arcsec) west of OB110462. The neighbor is ~ 3 magnitudes brighter than OB110462 at baseline (F814W = 16.7 mag, F606W = 19.0 mag). Because of its proximity and high contrast, the neighbor’s PSF might “leak” onto OB110462 and alter its astrometry and photometry. We perform injection and recovery tests to ascertain the reliability of faint source extraction near a bright source, in order to determine whether the astrometry and photometry of OB110462 as determined in §3.2 and §3.3 is biased by the bright neighbor.

The methodology and results of the injection and recovery analysis are detailed in Appendix B. In summary,

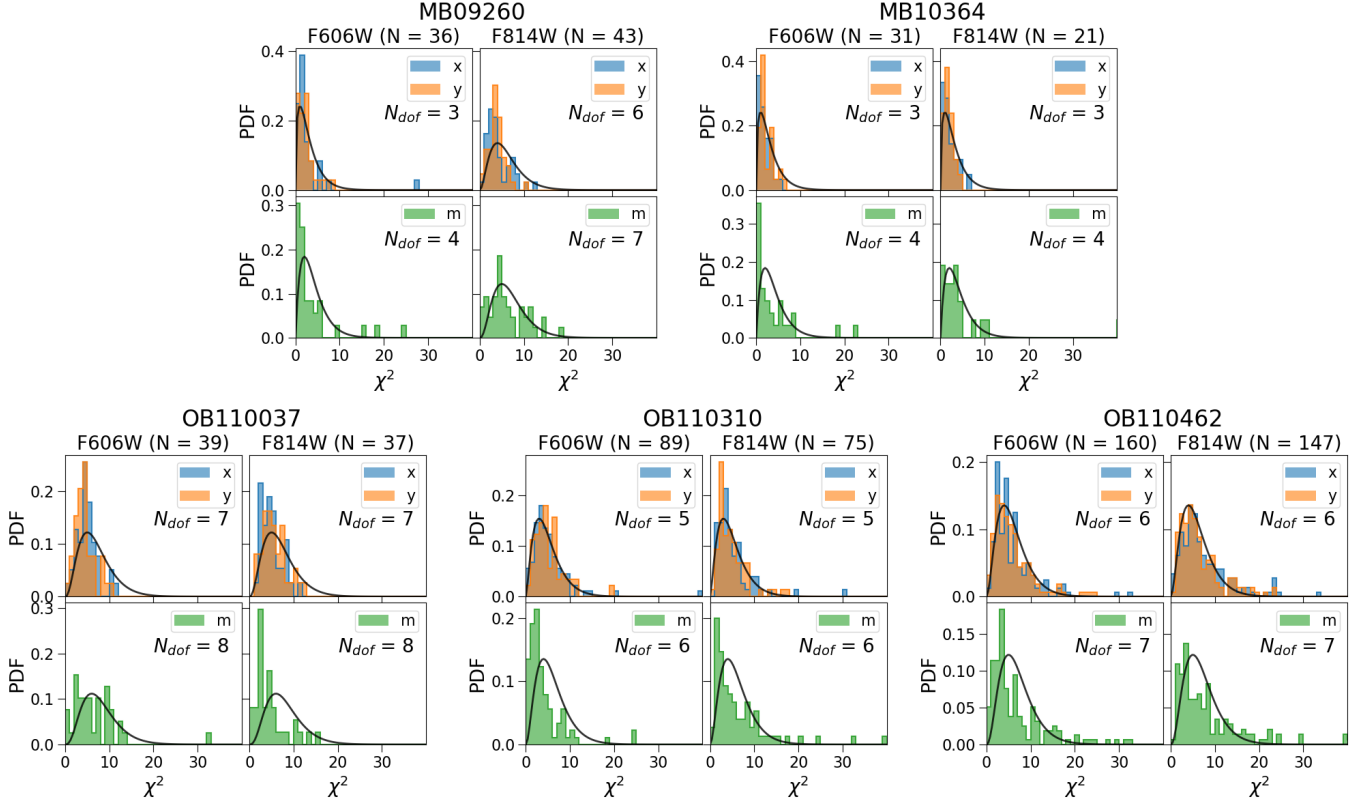


Figure 9. Histogram of χ^2 residual values to the linear fits with no parallax for the reference stars of each target (Table 5). In each panel, the left column shows the distributions for reference stars in F606W, while the right column shows F814W. The number of reference stars is listed as N . In each panel, the top row shows the χ^2 distribution of residuals of a linear fit to positions vs. time in $x \equiv \text{RA}$ and $y \equiv \text{Dec}$. The bottom row shows the χ^2 distribution of residuals of a constant fit to magnitude vs. time. The expected χ^2 distributions are shown in black, with the number of degrees of freedom listed as N_{dof} .

the positional bias is negligible when the target is highly magnified and of similar brightness to the neighbor. However, in epochs where the target is no longer magnified, the bright star biases the position of the target. In F814W, where the resolution is lower, the measured position of the target is biased toward the neighbor by ~ 0.4 mas along the target-neighbor separation vector. In F606W, where the resolution is higher, the bias is less (~ 0.25 mas) with the direction of bias more randomly oriented. Similarly, the photometric bias is larger when the contrast is large, with the bright neighbor causing the extracted photometry of OB110462 to be brighter than the injected values. The effect is again more severe in F814W than F606W because of the lower resolution.

Using the results of the injection and recovery analysis, we calculate a bias correction to apply to OB110462 astrometry and photometry (Table 19). The values in the table are added to astrometry and photometry derived in §3.2 and §3.3; the uncertainties are added in quadrature to the uncertainties in §3.2 and §3.3.

We only perform this analysis for OB110462, as it is the only faint target near a bright companion. All the

other targets are either bright with faint companions, isolated, or both bright and isolated.

3.2.5. Astrometric color offset

As mentioned in §3.1 the data taken in F606W and F814W filters are treated as independent measurements. For OB110037 and OB110462, the astrometric measurements in F606W and F814W do not agree within the uncertainties.

For OB110037, although the 2011 and 2012 epochs show good agreement, the 2013 to 2017 epochs become increasingly discrepant as time goes on. We attribute this difference to binarity (§5.4).

In contrast, for OB110462 the astrometry in the F606W and F814W are discrepant in all datasets, but the difference appears to be a relatively constant offset with time. This is true both before and after applying the bias correction in §3.2.4. Because the nature of the color difference appears to be a constant offset, we apply

Table 3. HST WFC3-UVIS Observations

Target	Epoch (UT)	PA	Filter	T_{exp}	N_{im}
	(yyyy-mm-dd)	(deg)		(sec)	
MB09260	2009-10-01	275.0	F606W	10.0	4*
				100.0	2
			F814W	20.0	1*
	2009-10-19	275.0	F606W	310.0	1*
			F814W	72.0	6
	2010-03-22	95.0	F606W	300.0	1*
			F814W	280.0	5
	2010-06-14	95.0	F606W	200.0	1*
			F814W	275.0	5
	2010-10-20	270.0	F606W	275.0	2*
			F814W	275.0	4
	2011-04-19	90.0	F606W	275.0	2
			F814W	275.0	4
	2011-10-24	270.0	F606W	275.0	2
			F814W	275.0	4
	2012-09-25	270.0	F606W	275.0	2
			F814W	275.0	4
	2013-06-17	105.5	F606W	275.0	2
			F814W	275.0	4
MB10364	2010-09-13	270.0	F606W	1.0	1
				2.0	1
			F814W	3.0	5
				1.0	1*
	2010-10-26	277.4	F606W	12.0	2
			F814W	12.0	6
	2011-04-13	90.0	F606W	260.0	2*
			F814W	120.0	4*
	2011-07-22	260.5	F606W	160.0	4*
			F814W	90.0	4*
	2011-10-31	278.8	F606W	30.0	5
			F814W	30.0	6
	2012-09-25	270.9	F606W	30.0	5
			F814W	30.0	6
	2013-10-24	277.0	F606W	40.0	5
			F814W	40.0	6
OB110037	2011-08-15	245.0	F606W	30.0	4
			F814W	40.0	4
				20.0	3*
	2011-09-26	270.8	F606W	30.0	5
			F814W	20.0	6
	2011-11-01	276.1	F606W	50.0	5
			F814W	30.0	5
	2012-05-07	98.1	F606W	80.0	4
			F814W	60.0	5
	2012-09-25	270.8	F606W	80.0	4
			F814W	60.0	5
	2013-10-21	274.3	F606W	80.0	4
			F814W	60.0	6
	2014-10-26	275.1	F606W	60.0	4
			F814W	55.0	6
	2017-03-13	90.0	F606W	60.0	3
			F814W	55.0	6
	2017-09-04	256.9	F606W	60.0	3
			F814W	55.0	6

NOTE— Asterisk (*) denotes observations excluded from analysis.

Table 4. HST WFC3-UVIS Observations

Target	Epoch (UT)	PA	Filter	T_{exp}	N_{im}
	(yyyy-mm-dd)	(deg)		(sec)	
OB110310	2011-09-21	270.0	F606W	75.0	4
			F814W	75.0	5
	2011-10-31	276.5	F606W	280.0	3
			F814W	200.0	4
	2012-04-24	96.0	F606W	280.0	3
			F814W	230.0	4
	2012-09-24	271.3	F606W	280.0	3
			F814W	230.0	4
	2013-10-21	274.8	F606W	280.0	3
			F814W	68.0	1*
				230.0	4
	2017-03-14	90.4	F606W	270.0	3
			F814W	230.0	4
	2017-09-01	268.4	F606W	270.0	3
			F814W	230.0	4
OB110462	2011-08-08	270.0	F606W	60.0	1*
				75.0	3
			F814W	120.0	1*
				60.0	1*
	2011-10-31	276.1		75.0	3
			F606W	280.0	3
			F814W	200.0	4
	2012-09-09	269.5	F606W	290.0	3
			F814W	190.0	4
	2012-09-25	271.3	F606W	280.0	3
			F814W	200.0	4
	2013-05-13	99.9	F606W	280.0	3*
			F814W	200.0	4*
	2013-10-22	274.6	F606W	285.0	3
			F814W	285.0	4
	2014-10-26	275.2	F606W	265.0	3
			F814W	265.0	4
	2017-08-11	255.2	F606W	250.0	3*
			F814W	250.0	4*
	2017-08-29	268.3	F606W	250.0	3
			F814W	250.0	4
	2021-10-01	272.0	F606W	407.0	5
			F814W	307.0	6

NOTE— Asterisk (*) denotes observations excluded from analysis.

a constant shift to the OB110462 F606W astrometry

$$\Delta_x = \frac{\sum w_{x,t}(x_{F814W,t} - x_{F606W,t})}{w_{x,t}} \quad (9)$$

$$\Delta_y = \frac{\sum w_{y,t}(y_{F814W,t} - y_{F606W,t})}{w_{y,t}} \quad (10)$$

where

$$w_{x,t} = (\sigma_{x,F814W,t}^2 + \sigma_{x,F606W,t}^2)^{-1/2} \quad (11)$$

$$w_{y,t} = (\sigma_{y,F814W,t}^2 + \sigma_{y,F606W,t}^2)^{-1/2}. \quad (12)$$

Table 5. Reference star criteria

Target	Magnitude range	Radius	$N_{\text{ep,detect}}$	EXCLUDED bright blue stars
MB09260	Target range ± 1 mag: 14.5 < F814W < 18.8 16.9 < F606W < 21.7	30"	11	F606W-F814W < 2.6 & F814W < 20.6
MB10364	2010-09-13: 12.5 < F814W < 18.0 11.5 < F606W < 19.2 2010-10-26: 15.1 < F814W < 18.0 13.4 < F606W < 19.2 2011-10-31: 15.8 < F814W < 18.0 14.4 < F606W < 19.2 2012-09-25: 16.0 < F814W < 18.0 14.5 < F606W < 19.2 2013-10-24: 16.1 < F814W < 18.0 14.7 < F606W < 19.2	30"	8	None excluded
OB110037	Target range ± 0.5 mag: 14.4 < F814W < 16.9 16.4 < F814W < 18.8	30"	12	F606W-F814W < 1.75 & F814W < 19.6
OB110310	Target range ± 0.1 mag: 16.9 < F814W < 18.7 19.6 < F606W < 21.4	30"	12	F606W-F814W < 2.4 & F814W < 21.0
OB110462	Target range ± 0.1 mag: 17.1 < F814W < 20.0 19.2 < F606W < 22.1	30"	14	F606W-F814W < 1.9 & F814W < 20.6

NOTE— These are the criteria for the last pass.

and t indexes the observation times. Thus the modified astrometry for F606W is

$$x'_{\text{F606W},t} = x_{\text{F606W},t} + \Delta_x \quad (13)$$

$$y'_{\text{F606W},t} = y_{\text{F606W},t} + \Delta_y. \quad (14)$$

The values of the offset are $\Delta_x = -0.573$ mas and $\Delta_y = 0.412$ mas. Note that these offsets are calculated using the bias-corrected astrometry.¹⁰ See Appendix I for further details and justification.

We also investigate stars nearby to determine whether any of them show similar behavior. For the 70 stars within 3" of OB110462, we calculate the average positional offset between F814W and F606W in RA and Dec using Eqs. 9 and 10. We then search for stars where the average positional uncertainty in F814W and F606W (whichever is larger) is smaller than the average positional offset to determine which differences are significant. There are 4 stars where the average positional

offset is greater than the average positional uncertainty in RA, and an additional 4 stars the average offset is greater than the average positional uncertainty in Dec. Hence, a total of 8 out of the 70 stars near the target also show these significant offsets. Thus, this effect is seen for roughly 10% of the stars, and so is not very unusual. Although we currently have no explanation for its significance, it appears random, and thus include the astrometric offset when analyzing the data. See Appendix I for additional details.

3.2.6. Comparison to Gaia proper motions and parallaxes

For the three targets with astrometric solutions in Gaia EDR3 (MB10364, OB110037, and OB110310), the Gaia proper motions and parallaxes are compared to the fit proper motions and parallaxes (presented in §5 and Tables 13 - 15). Note that we fit a proper motion and parallax to the source and lens along with an astrometric microlensing model. On the other hand, Gaia fits a proper motion and parallax to the source and lens (the "target") as they are unresolved, and assumes the target is a single star with parallax. The effect of astrometric lensing in Gaia on the proper motions is negligible (Appendix D). Additional details about the various Gaia

¹⁰ Note that even before the bias correction of §3.2.4 is applied, this color offset is still present. In fact, it is slightly larger, with $\Delta_x = -0.751$ mas and $\Delta_y = 0.499$ mas. The bias correction is not the source of the color dependent astrometric offset; rather, it helps to slightly decrease the offset.

Table 6. Gaia vs HST fit (transformed) Proper Motions

Target	$\mu_{\text{HST,L}}$ (mas/yr)	$\mu_{\text{HST,S}}$ (mas/yr)	μ_{Gaia} (mas/yr)
MB10364	$(-5.11^{+1.62}_{-1.10}, -7.78^{+0.58}_{-0.89})$	$(-7.56^{+0.12}_{-0.12}, -6.49^{+0.11}_{-0.11})$	$(-7.43 \pm 0.08, -6.80 \pm 0.05)$
OB110037	$(6.27^{+1.27}_{-1.20}, -6.56^{+0.77}_{-0.81})$	$(2.19^{+0.24}_{-0.24}, -3.87^{+0.20}_{-0.20})$	$(2.40 \pm 0.13, -3.91 \pm 0.09)$
OB110310	$(-0.02^{+1.93}_{-1.16}, -4.68^{+2.39}_{-2.13})$	$(-2.41^{+0.12}_{-0.12}, -7.26^{+0.08}_{-0.08})$	$(-2.08 \pm 1.12, -6.75 \pm 0.58)$

NOTE—The source and lens proper motions here have been transformed into the absolute Gaia proper motion frame, which is offset to the HST proper motion frame as described in Appendix C. The uncertainties on μ_L and μ_S also reflect the uncertainty in the Gaia to HST proper motion transformation; the standard error on the mean of that transformation was added in quadrature to the uncertainties from the proper motion fits. For these reason μ_L and μ_S do not match the reported values in Tables 13 - 15.

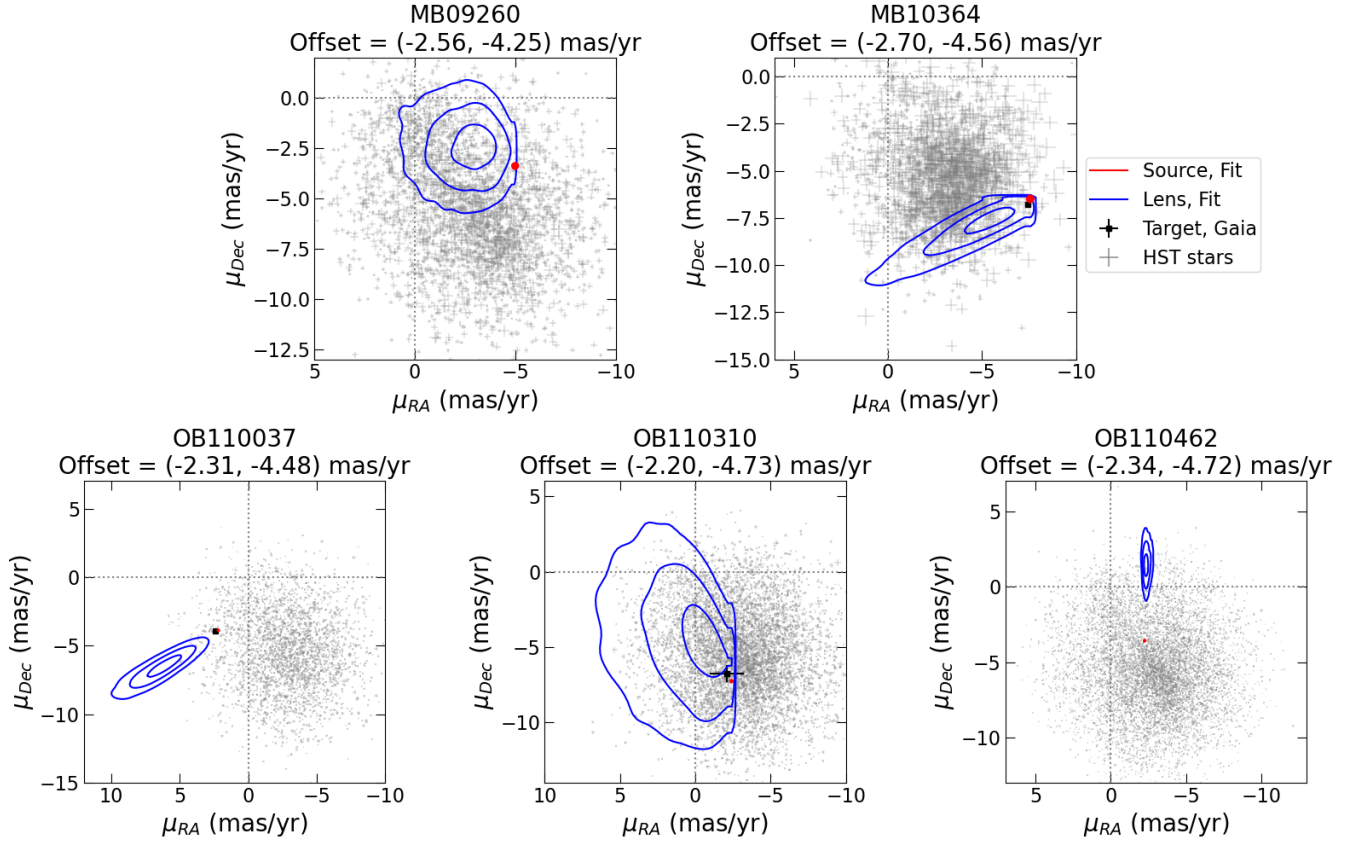


Figure 10. Proper motions for stars in the field of the target. The proper motions derived from F814W HST observations for stars within $30''$ of the target are shown in gray with 1σ uncertainties. Only stars with F814W < 23 for MB09260, OB110310, OB110462 and F814W < 22 for MB10364, OB110037 are shown. As the alignment procedure places the stars in a reference frame where the relative motion is zero, a constant offset must be added to obtain proper motions in the original Gaia absolute reference frame. This offset is calculated by matching the stellar positions in HST to those in Gaia with `astrometric_excess_noise_sig` < 2 , and then calculating the 3σ clipped average weighted by the uncertainty in their difference. The offset value is given in the title for each field. For targets in Gaia with a single-star proper motion is estimated (MB10364, OB11037, OB110310), they are plotted as black squares. The best-fit lens and source proper motion as determined from fitting the HST data with a microlensing model is shown in blue and red $1 - 2 - 3\sigma$ contours, respectively.

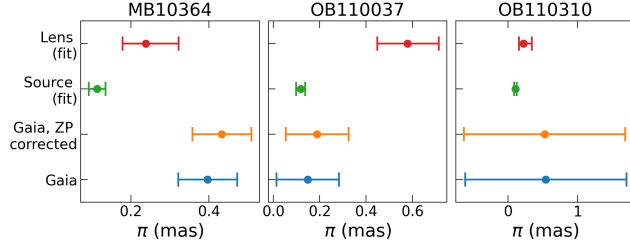


Figure 11. Comparison of Gaia parallaxes with the fit lens and source parallax.

metrics discussed are in Appendix F and Lindegren et al. (2021a).

To make proper motion comparisons between Gaia and HST, the proper motions from the HST frame in which the fitting was performed need to be transformed into the absolute Gaia frame, as the iterative astrometric alignment procedure described in §3.2 produces a reference frame that is at rest with the average proper motion of the aligned stars (Lu et al. 2016). See Appendix C on how the proper motion offset between the HST and Gaia frames is calculated. The source and lens proper motion in the Gaia frame, as well as the Gaia target proper motions, are listed in Table 6 for MB10364, OB110037, and OB110310. The vector point diagram for all stars from the HST observations transformed to the Gaia frame, along with the $1-2-3\sigma$ contours from the source and lens fit, are shown in Figure 10. For MB10364, OB110037, and OB110310 the target proper motion from Gaia is also included.

MB10364—MB10364’s proper motion in Gaia is $(-7.43 \pm 0.08, -6.80 \pm 0.05)$ mas/yr. The fit from HST for the lens is $(-5.11^{+1.62}_{-1.10}, -7.78^{+0.58}_{-0.89})$ mas/yr, inconsistent with Gaia in RA and Dec at $\sim 2\sigma$. The fit from HST for the source is $(-7.56^{+0.12}_{-0.12}, -6.49^{+0.11}_{-0.11})$ mas/yr, inconsistent with Gaia in Dec at $\sim 2\sigma$. MB10364 has parallax $\pi = 0.43 \pm 0.08$ in Gaia. The source and lens parallax from the MB10364 fits are $\pi_S = 0.11^{+0.02}_{-0.02}$, $\pi_L = 0.24^{+0.08}_{-0.06}$, neither of which are consistent with the Gaia value. The Gaia fit for MB10364 has a large renormalized unit weight error (RUWE = 1.388), and a large astrometric excess noise ($\epsilon = 0.406$ mas) with high significance ($D = 12.020$), indicating the single star model is not providing a good fit. This mismatch is not due to astrometric microlensing (Appendix D). The most likely explanation for the discrepancies are crowding—there are several stars close to MB10364 that would cause confusion (Figures 1 and 12). As the source and lens are not resolvable, the fact that 15% of the Image Parameters Determination (IPD) algorithm has identified a double peak is likely due to confusion. This means the Gaia measurement is not reliable.

OB110037—OB110037’s proper motion in Gaia is $(2.40 \pm 0.13, -3.91 \pm 0.09)$ mas/yr. The fit from HST for the lens is $(6.27^{+1.27}_{-1.20}, -6.56^{+0.77}_{-0.81})$ mas/yr, inconsistent with Gaia in both RA and Dec at $\sim 3\sigma$. The fit from HST for the source is $(2.19^{+0.24}_{-0.24}, -3.87^{+0.20}_{-0.20})$ mas/yr, consistent with Gaia. The caveat to this is that the fit to the HST F606W astrometry is poor (Figure 17). However, the astrometric lensing model is mostly independent of the proper motion model, hence the proper motion value can still be believed. OB110037 is very well measured and behaved in Gaia (it is the only target with a 5-parameter solution, see Table 2). Additionally from the image (Figures 1 and 12) OB110037 is relatively bright and isolated. The fact that the fit source and Gaia proper motions are consistent would indicate that the lens is dim in comparison to the star in Gaia *G* band. This makes sense as the astrometric shift for OB110037 is undetectable by the time Gaia begins observing.

OB110037 is well modeled in Gaia by a single source with parallax. Although the microlensing model is a poor fit to the astrometry due to a time-dependent color-offset, the proper motions from our model are in good agreement with Gaia. OB110037 has parallax $\pi = 0.19 \pm 0.13$ in Gaia. The source and lens parallax from the OB110037 fits are $\pi_S = 0.12^{+0.02}_{-0.02}$, $\pi_L = 0.58^{+0.14}_{-0.13}$. The source parallax is consistent with the Gaia value. We note that the source may appear well-behaved in Gaia because the astrometry is in a single filter. The multi-band HST astrometry may be useful in identifying binary companions. See Appendix F for further discussion.

OB110310—OB110310’s proper motion in Gaia is $(-2.08 \pm 1.12, -6.75 \pm 0.58)$ mas/yr. The fit from HST for the lens is $(-0.02^{+1.93}_{-1.16}, -4.68^{+2.39}_{-2.13})$ mas/yr, consistent with Gaia due to large uncertainties in both Gaia and the fit. The fit from HST for the source is $(-2.41^{+0.12}_{-0.12}, -7.26^{+0.08}_{-0.08})$ mas/yr, consistent with Gaia. OB110310 has parallax $\pi = 0.53 \pm 1.16$ in Gaia (note the OB110310 zero point correction is an extrapolation), consistent with non-detection of parallax. The source and lens parallax from the OB110310 fit are $\pi_S = 0.10^{+0.02}_{-0.02}$, $\pi_L = 0.22^{+0.12}_{-0.07}$, which are both consistent within the very wide uncertainties of Gaia. The fact that the source and Gaia proper motions are consistent would indicate that the lens is dim in comparison to the star in Gaia *G* band; blending in F814W and F606W also suggest a dark lens (Table 15). The fact that in the IPD 55% of transits have either truncation or multiple gates flagged in one or more windows indicates likely contamination. OB110310 is not very bright and in a somewhat crowded region (Figures 1 and 12).

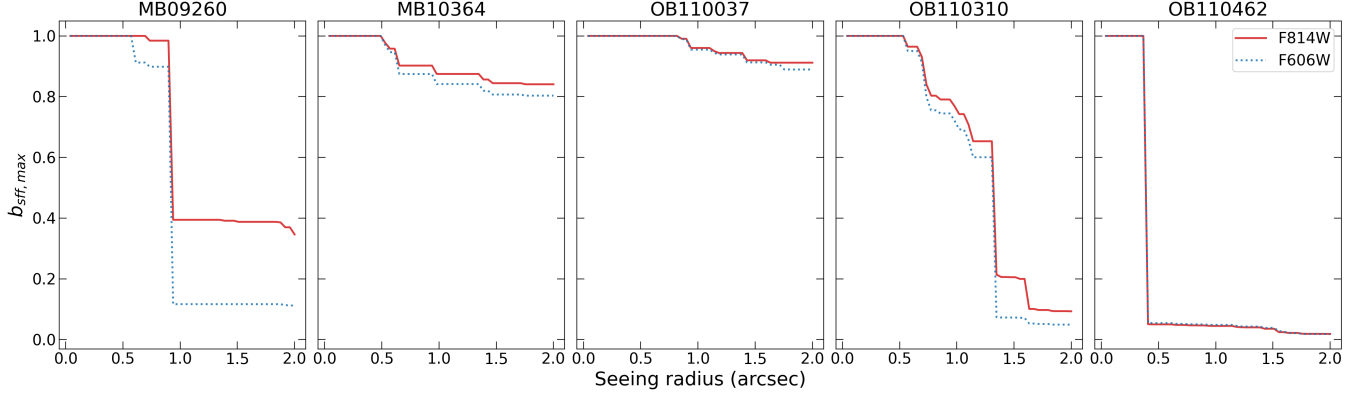


Figure 12. Estimated upper limit on b_{SFF} vs. seeing disk radius in F814W and F606W passbands, as inferred by high resolution imaging from HST. By assuming all the flux from the target is due to the source, an upper limit on $b_{SFF,max}$ can be estimated by taking the flux ratio of the target to all stars within the seeing disk. $b_{SFF,max}$ is also a proxy for quantifying the amount of crowding around the source.

The astrometric noise is large ($\epsilon = 0.894$ mas) but the value is insignificant ($D = 0.332$). Together these explain why the Gaia measurement does not produce very good constraints.

3.3. HST Photometric Analysis

To obtain precise relative photometry, for each epoch a small constant magnitude offset is applied to the stars. The offset is calculated by assuming the reference stars have constant brightness in time, which we define as the 3σ clipped mean. As with the positional uncertainties, for the magnitude uncertainties we used the error on the mean, with an additional additive error empirically determined during the astrometric alignment process; details are in Appendix A.

Analogous to the positional transformation, we evaluate the magnitude transformation by checking how well a constant magnitude describes the stars

$$\chi_m^2 = \sum_i \left(\frac{m_i - m_0}{\sigma_{m_i}} \right)^2 \quad (15)$$

where m_i are the calibrated magnitudes, m_0 is the constant magnitude fit, and σ_{m_i} is the uncertainty on the calibrated magnitude. The χ^2 distributions for the magnitude residuals of the reference stars detected in all N_{ep} epochs are shown in the bottom panels of Figure 9. The expected residual distribution has $N_{ep,detect} - 1$ degrees of freedom, as there is one free parameter in the constant magnitude fit.

4. MICROLENSING MODELING

The mass of the lens M_L in a microlensing event is given by

$$M_L = \frac{\theta_E}{\kappa \pi_E}, \quad (16)$$

where θ_E is the angular Einstein radius (Equation 17), π_E is the microlensing parallax (Equation 21), and $\kappa = 4G/(1AU \cdot c^2)$ is a constant. Densely sampled photometric microlensing observations constrain π_E , while astrometric microlensing observations constrain θ_E .¹¹

To measure these quantities of interest, we simultaneously fit the ground-based photometry and HST photometry and astrometry with a point-source point-lens (PSPL) microlensing model with parallax. We do not consider models involving either binary lenses or sources, nor higher-order effects beyond parallax; these are beyond the scope of this work. Discussion of the need for models more complex than PSPL with parallax are discussed in §5.

4.1. Microlensing Definitions

All microlensing quantities defined in the following section are in the heliocentric reference frame.

The Einstein radius, which sets the angular scale of the microlensing event, is given by

$$\theta_E = \sqrt{\frac{4GM_L}{c^2} \left(\frac{1}{d_L} - \frac{1}{d_S} \right)} \quad (17)$$

where M_L is the mass of the lens, and d_L and d_S are the distance to the lens and the source, respectively.

The Einstein crossing time t_E , the time it takes for the source to traverse the angular radius of the lens and sets the timescale of the events, is given by

$$t_E = \frac{\theta_E}{\mu_{rel}} \quad (18)$$

¹¹ Note that theoretically astrometric microlensing observations should also be able to constrain π_E , but due to the cadence of observations, it is currently unachievable.

Table 7. HST Calibrated Data for Each Target

Target	Filter	Date	RA (mas)	Dec (mas)	Mag (Vega)
MB09260	F814W	2009-10-19	7.80 ± 0.15	5.15 ± 0.14	15.484 ± 0.005
		2010-03-22	5.31 ± 0.14	3.80 ± 0.14	17.656 ± 0.005
		2010-06-14	4.31 ± 0.18	2.97 ± 0.18	17.760 ± 0.007
		2010-10-20	2.54 ± 0.14	1.60 ± 0.14	17.812 ± 0.014
		2011-04-19	0.12 ± 0.15	0.01 ± 0.15	17.838 ± 0.018
		2011-10-24	-2.44 ± 0.21	-1.71 ± 0.21	17.833 ± 0.005
		2012-09-25	-7.07 ± 0.15	-4.80 ± 0.15	17.836 ± 0.007
	F606W	2013-06-17	-10.57 ± 0.26	-7.02 ± 0.22	17.829 ± 0.011
		2009-10-01	8.15 ± 0.22	5.57 ± 0.22	17.899 ± 0.013
		2011-04-19	0.13 ± 0.57	0.17 ± 0.57	20.750 ± 0.083
		2011-10-24	-2.17 ± 0.52	-1.59 ± 0.52	20.748 ± 0.007
		2012-09-25	-6.23 ± 1.31	-4.41 ± 1.32	20.733 ± 0.023
		2013-06-17	-10.10 ± 0.49	-7.21 ± 0.54	20.738 ± 0.036
MB10364	F814W	2010-09-13	9.61 ± 0.16	8.24 ± 0.16	13.366 ± 0.011
		2010-10-26	8.76 ± 0.16	7.72 ± 0.15	14.657 ± 0.005
		2011-10-31	1.23 ± 0.19	0.81 ± 0.18	15.315 ± 0.006
		2012-09-25	-5.70 ± 0.19	-4.89 ± 0.19	15.315 ± 0.010
		2013-10-24	-13.90 ± 0.18	-11.89 ± 0.18	15.316 ± 0.009
	F606W	2010-09-13	8.81 ± 1.70	8.81 ± 1.70	14.538 ± 0.017
		2010-10-26	8.46 ± 0.50	7.59 ± 0.50	15.842 ± 0.017
		2011-10-31	1.47 ± 0.28	1.13 ± 0.28	16.498 ± 0.006
		2012-09-25	-5.66 ± 0.31	-4.99 ± 0.31	16.504 ± 0.008
		2013-10-24	-13.89 ± 0.25	-11.79 ± 0.25	16.502 ± 0.008
OB110037	F814W	2011-08-15	-4.35 ± 0.11	8.24 ± 0.14	14.864 ± 0.021
		2011-09-26	-4.33 ± 0.12	7.82 ± 0.12	15.029 ± 0.005
		2011-11-01	-4.34 ± 0.12	7.52 ± 0.12	15.774 ± 0.006
		2012-05-07	-3.10 ± 0.13	5.40 ± 0.12	16.315 ± 0.019
		2012-09-25	-2.22 ± 0.14	3.86 ± 0.14	16.321 ± 0.009
		2013-10-21	0.10 ± 0.12	-0.36 ± 0.12	16.327 ± 0.005
		2014-10-26	2.45 ± 0.14	-4.36 ± 0.13	16.328 ± 0.006
		2017-03-13	7.74 ± 0.12	-13.21 ± 0.12	16.334 ± 0.007
		2017-09-04	8.05 ± 0.14	-14.90 ± 0.13	16.322 ± 0.011
	F606W	2011-08-15	-4.02 ± 0.25	8.15 ± 0.24	16.916 ± 0.011
		2011-09-26	-4.23 ± 0.20	7.79 ± 0.20	17.086 ± 0.020
		2011-11-01	-4.39 ± 0.24	7.36 ± 0.23	17.794 ± 0.005
		2012-05-07	-2.69 ± 0.31	5.34 ± 0.33	18.301 ± 0.016
		2012-09-25	-2.34 ± 0.26	3.81 ± 0.26	18.306 ± 0.006
		2013-10-21	0.65 ± 0.24	-0.76 ± 0.24	18.314 ± 0.006
		2014-10-26	3.73 ± 0.22	-5.29 ± 0.22	18.320 ± 0.015
		2017-03-13	9.48 ± 0.26	-14.04 ± 0.26	18.331 ± 0.008
		2017-09-04	9.80 ± 0.27	-16.84 ± 0.24	18.326 ± 0.027
OB110310	F814W	2011-09-21	5.20 ± 0.14	15.95 ± 0.14	16.945 ± 0.013
		2011-10-31	4.86 ± 0.17	14.85 ± 0.17	18.058 ± 0.004
		2012-04-24	3.79 ± 0.13	11.35 ± 0.13	18.602 ± 0.013
		2012-09-24	2.82 ± 0.17	8.47 ± 0.17	18.616 ± 0.011
		2013-10-21	0.14 ± 0.13	0.59 ± 0.14	18.621 ± 0.005
		2017-03-14	-7.92 ± 0.18	-23.84 ± 0.18	18.608 ± 0.005
	F606W	2017-09-01	-8.88 ± 0.16	-27.36 ± 0.16	18.613 ± 0.012
		2011-09-21	5.43 ± 0.22	15.98 ± 0.22	19.663 ± 0.018
		2011-10-31	4.73 ± 0.34	15.06 ± 0.34	20.780 ± 0.007
		2012-04-24	3.55 ± 0.38	11.44 ± 0.37	21.329 ± 0.034
		2012-09-24	2.79 ± 0.49	8.02 ± 0.49	21.180 ± 0.212
		2013-10-21	0.56 ± 0.30	0.87 ± 0.30	21.339 ± 0.007
		2017-03-14	-7.81 ± 0.31	-23.78 ± 0.31	21.333 ± 0.022
		2017-09-01	-9.31 ± 0.34	-27.08 ± 0.35	21.335 ± 0.034
OB110462	F814W	2011-08-08	7.52 ± 0.15	11.46 ± 0.15	17.209 ± 0.028
		2011-10-31	6.44 ± 0.23	9.73 ± 0.22	18.849 ± 0.006
		2012-09-09	4.08 ± 0.23	6.58 ± 0.23	19.756 ± 0.009
		2012-09-25	4.28 ± 0.37	6.41 ± 0.37	19.767 ± 0.008
		2013-10-22	1.43 ± 0.33	2.41 ± 0.34	19.838 ± 0.048
		2014-10-26	-0.82 ± 0.29	-0.97 ± 0.30	19.879 ± 0.009
		2017-08-29	-7.19 ± 0.27	-10.58 ± 0.26	19.874 ± 0.009
		2021-10-01	-15.74 ± 0.19	-25.03 ± 0.19	19.859 ± 0.020
	F606W	2011-08-08	6.72 ± 0.43	11.76 ± 0.43	19.313 ± 0.023
		2011-10-31	6.22 ± 0.50	10.54 ± 0.52	20.974 ± 0.010
		2012-09-09	4.56 ± 0.37	5.56 ± 0.37	21.867 ± 0.050
		2012-09-25	4.32 ± 0.59	6.40 ± 0.59	21.919 ± 0.010
		2013-10-22	1.72 ± 0.37	2.44 ± 0.36	22.011 ± 0.015
		2014-10-26	-1.26 ± 0.46	-0.84 ± 0.44	22.042 ± 0.015
		2017-08-29	-7.14 ± 0.41	-10.62 ± 0.41	22.017 ± 0.027
		2021-10-01	-15.21 ± 0.44	-25.02 ± 0.44	22.017 ± 0.017

NOTE— Relative positions and magnitude of the target by epoch and filter.

where μ_{rel} is the lens-source proper motion $|\boldsymbol{\mu}_S - \boldsymbol{\mu}_L|$.

The source-lens separation on sky $\boldsymbol{\theta}_S - \boldsymbol{\theta}_L$ normalized by the Einstein radius is denoted $\mathbf{u}(t)$. The minimum separation is denoted $\mathbf{u}(t_0) = \mathbf{u}_0$. The impact parameter u_0 is the scalar quantity associated with \mathbf{u}_0 . We follow the convention of Gould (2004) where if $u_{0,E} > 0$, the source is to the East of the lens, and $u_0 > 0$; if $u_{0,E} < 0$, the source is to the West of the lens, and $u_0 < 0$. If rectilinear motion is assumed, the lens-source separation is given by

$$\mathbf{u}(t) = \mathbf{u}_0 + \frac{t - t_0}{t_E} \hat{\boldsymbol{\mu}}_{rel}. \quad (19)$$

However, an Earthly observer's perspective of the lensing event is modulated by the Earth's motion around the Sun. For events with long duration ($t_E \gtrsim 3$ months), the Earth's orbital motion violates this rectilinear assumption and must be taken into account. This modifies $\mathbf{u}(t)$ to

$$\mathbf{u}(t) = \mathbf{u}_0 + \frac{t - t_0}{t_E} \hat{\boldsymbol{\mu}}_{rel} - \pi_E \mathbf{P}(t) \quad (20)$$

where

$$\pi_E = \frac{\pi_{rel}}{\theta_E} \quad (21)$$

is the microlensing parallax and $\mathbf{P}(t)$ is the parallax vector. The microlensing parallax is the relative parallax of the source and lens $\pi_{rel} = \pi_L - \pi_S$ normalized by the Einstein radius. The microlensing parallax vector π_E (not to be confused with the parallax vector $\mathbf{P}(t)$) encodes the magnitude of the microlensing parallax and the direction of the relative source-lens proper motion:

$$\pi_E = \pi_E \hat{\boldsymbol{\mu}}_{rel}. \quad (22)$$

The photometric brightening of the source is given by

$$A(u) = \frac{u^2 + 2}{|u| \sqrt{u^2 + 4}}. \quad (23)$$

where the total flux $F(t)$ in the telescope aperture is

$$F(t) = A(t)F_S + F_L + F_N \quad (24)$$

where F_S , F_L , and F_N are the fluxes of the source, lens, and neighboring un-lensed stars in the aperture of the telescope, respectively. The source flux fraction is

$$b_{SFF} = \frac{F_S}{F_S + F_L + F_N} \quad (25)$$

and quantifies the fraction of light lensed in an observed microlensing event. Note that b_{SFF} depends on the observing wavelength and seeing/aperture. The non-source flux $F_L + F_N$ is also called blend flux. Blend flux decreases b_{SFF} and dilutes the magnitude of both the photometric amplification and astrometric shift.

A PSPL photometric microlensing event is characterized by five geometric parameters: t_0 , u_0 , t_E , and π_E . For each telescope that observes this event, two additional parameters, m_{base} and b_{SFF} , are needed to describe each lightcurve; these depend on the seeing and camera filter. As all photometric microlensing observable quantities are normalized by θ_E , the lens mass cannot be determined.

In contrast, astrometric microlensing provides a direct measurement of θ_E . The apparent position of the source, i.e. the centroid of the lensed source images $\boldsymbol{\theta}_{S,c}$, is given by

$$\boldsymbol{\theta}_{S,c}(u, \theta_E) = \frac{(u^2 + 3)\mathbf{u}\theta_E}{u^2 + 2}. \quad (26)$$

Assuming no blended light, the difference between the source's apparent and true positions, i.e. the astrometric shift, is given by

$$\boldsymbol{\delta}_c(u, \theta_E) = \frac{\mathbf{u}\theta_E}{u^2 + 2}. \quad (27)$$

4.2. Modeling framework

We perform parameter estimation using a Bayesian framework. Bayes' theorem

$$\pi(\boldsymbol{\Theta})\mathcal{L}(\mathbf{y}|\boldsymbol{\Theta}) = \mathcal{Z}(\mathbf{y})\mathcal{P}(\boldsymbol{\Theta}|\mathbf{y}) \quad (28)$$

relates the prior π and likelihood \mathcal{L} to the evidence \mathcal{Z} and posterior \mathcal{P} . The goal of parameter estimation is to calculate \mathcal{P} . The likelihood $\mathcal{L}(\mathbf{y}|\boldsymbol{\Theta})$ is presented in Appendix G, and the priors $\pi(\boldsymbol{\Theta})$ are discussed in Appendix H.

The data is fit using MultiNest (Feroz et al. 2009), an implementation of the nested sampling algorithm (Skilling 2004). Nested sampling produces an estimate of the evidence $\mathcal{Z} = \int \pi(\boldsymbol{\Theta})\mathcal{L}(\boldsymbol{\Theta})d\boldsymbol{\Theta}$ and is a by-product the posterior \mathcal{P} . In contrast to methods such as MCMC, nested sampling is designed to better explore multimodal likelihood spaces; however, care must still be taken to ensure that all local minima are explored.

4.3. Likelihood weighting

There is a question of how best to combine the photometry and astrometry data sets, as they represent two different types of measurements. In particular, the question is how much weight each dataset should receive given that there are several orders of magnitude more ground-based data points than HST data points. Thus, the ground-based photometry has an outsize effect on the likelihood. It can be argued that each data point should contribute equally to the likelihood. We consider this to be "default weight" (hereafter abbreviated as DW) likelihood, i.e.

$$\log \mathcal{L}_{tot} = \log \mathcal{L}_{O,phot} + \log \mathcal{L}_{H,phot} + \log \mathcal{L}_{H,ast} \quad (29)$$

Table 8. 99.73% credible intervals/upper limits

Parameter	θ_E (mas)	$\delta_{c,max}$ (mas)	$M_L (M_\odot)$	π_E
MB09260	< 2.42	< 0.85	$1.37^{+2.72}_{-1.16}$	$0.09^{+0.13}_{-0.03}$
MB10364	< 1.76	< 0.62	$0.21^{+0.61}_{-0.18}$	$0.27^{+0.02}_{-0.01}$
OB110037	$1.24^{+1.10}_{-0.90}$	$0.44^{+0.39}_{-0.32}$	$0.41^{+0.37}_{-0.30}$	$0.37^{+0.02}_{-0.02}$
OB110310	< 2.75	< 0.97	$0.78^{+2.98}_{-0.68}$	$0.13^{+0.20}_{-0.08}$
OB110462DW	$4.14^{+2.96}_{-3.14}$	$1.46^{+1.05}_{-1.11}$	$2.12^{+3.51}_{-1.46}$	$0.24^{+0.11}_{-0.16}$
OB110462EW	$4.03^{+1.80}_{-1.73}$	$1.43^{+0.64}_{-0.61}$	$3.69^{+1.80}_{-1.53}$	$0.13^{+0.01}_{-0.02}$

Table 9. Lens type probabilities (%)

Target	Star	BD	WD	NS	BH
MB09260	4	0	38	44	14
MB10364	36	29	36	0	0
OB110037	74	0	26	0	0
OB110310	5	3	65	22	5
OB110462 DW	0	0	0	1	99
OB110462 EW	0	0	10	51	39

NOTE— The Star probabilities are upper limits, while the brown dwarf (BD), white dwarf (WD), neutron star (NS), and BH probabilities are lower limits. This is because the luminous lens probabilities are upper limits, and the dark lens probabilities are lower limits; see Appendix E for details. The probabilities for MB10364 sum to 101 and not 100 because of rounding error when not reporting decimal places. Note that there are two entries for OB110462, one based on a fit with “default weighting” (OB110462 DW) and one based on a fit with “equal weighting” (OB110462 EW). See §4.3 for details.

where $\mathcal{L}_{O,phot}$, $\mathcal{L}_{H,phot}$, and $\mathcal{L}_{H,ast}$ are the likelihoods of the OGLE or MOA photometry, HST photometry, and HST astrometry respectively.

However, it could also be argued that each dataset is independent, and so should each contribute equally to the likelihood. We call this the “equal weight” (hereafter abbreviated as EW) likelihood, i.e.

$$\log \mathcal{L}_{tot} = \frac{\log \mathcal{L}_{O,phot}}{n_{O,phot}} + \frac{\log \mathcal{L}_{H,phot}}{n_{H,phot}} + \frac{\log \mathcal{L}_{H,ast}}{n_{H,ast}} \quad (30)$$

where $n_{O,phot}$, $n_{H,phot}$, and $n_{H,ast}$ are the number of data points in the OGLE photometry, HST photometry, and HST astrometry.

These different likelihoods are essentially giving the different datasets different weights, in the case that they are inconsistent with each other. For all targets, we fit using the default weight likelihood; for OB110462 we additionally fit using the equal weight likelihood.

5. RESULTS

A large (> 1 mas) astrometric microlensing signal is detected in OB110462 (§5.1). A small, but significant, astrometric microlensing signal of 0.4 mas is also detected for OB110037. The other three targets show signals that are consistent with zero. Table 8 reports the

lens masses, Einstein radii, maximum astrometric shifts, and microlensing parallaxes either as measured values or upper limits.

In the sections that follow, the posteriors of the joint photometry and astrometry microlensing fits for the individual targets are presented. Tables 10 - 15 list the median and 1σ (68%) credible intervals for each parameter, in addition to the maximum a posteriori (MAP) and maximum likelihood (\mathcal{L}_{max})¹² solution.

The posteriors are used to constrain the types of lenses allowed (star, brown dwarf (BD), white dwarf (WD), neutron star (NS), or black hole (BH)). From a mass measurement alone, it cannot be determined whether a $5M_\odot$ object is a star or a BH. Additional information about the lens’ brightness is needed, which can be estimated using the source flux fractions in the high-resolution HST filters. By calculating the brightest star allowed by the inferred source flux fractions, we can determine whether a luminous lens (i.e. stellar lens) or dark lens (i.e. compact object lens) scenario is more likely. The method to calculate the probability of a dark lens is outlined in Appendix E. We report the relative probabilities of Star:BD:WD:NS:BH from this calculation in Table 9.

5.1. OB110462

From the microlensing fit, we infer that OB110462 is a NS or a mass gap BH. The data and model for OB110462 with the default weight (DW) likelihood are shown in Figures 7 (photometry) and 14 (astrometry), and the fit posteriors are summarized in Table 10. The inferred Einstein crossing time t_E is $290.12^{+2.67}_{-2.68}$ days, the microlensing parallax π_E is $0.13^{+0.006}_{-0.006}$, the Einstein radius θ_E is $4.03^{+1.14}_{-1.16}$, and the lens mass M_L is $3.69^{+0.55}_{-0.51} M_\odot$. The data and model for OB110462 with the equal weight (EW) likelihood are shown in Figures 8 (photometry) and 13 (astrometry), and the fit posteriors are summarized in Table 11. The inferred Einstein crossing time t_E is $277.25^{+12.58}_{-9.23}$ days, the microlensing parallax π_E is $0.24^{+0.05}_{-0.05}$, the Einstein radius θ_E is $4.14^{+1.00}_{-1.04}$, and the lens mass M_L is $2.12^{+0.74}_{-0.54} M_\odot$. Further, we find that the object is located relatively nearby at 690–1370pc in the direction of the galactic bulge and has a small transverse velocity of < 25 km/s.

The probability that OB110462 is a dark lens is 100%, ruling out the possibility of a stellar lens and making OB110462 the first detection of a compact object with

¹² For most of the targets, the MAP solution is equal to the maximum likelihood (MLE) solution, i.e. values of the parameters for the mode of the posterior distribution are the same as those where the likelihood function is maximized.

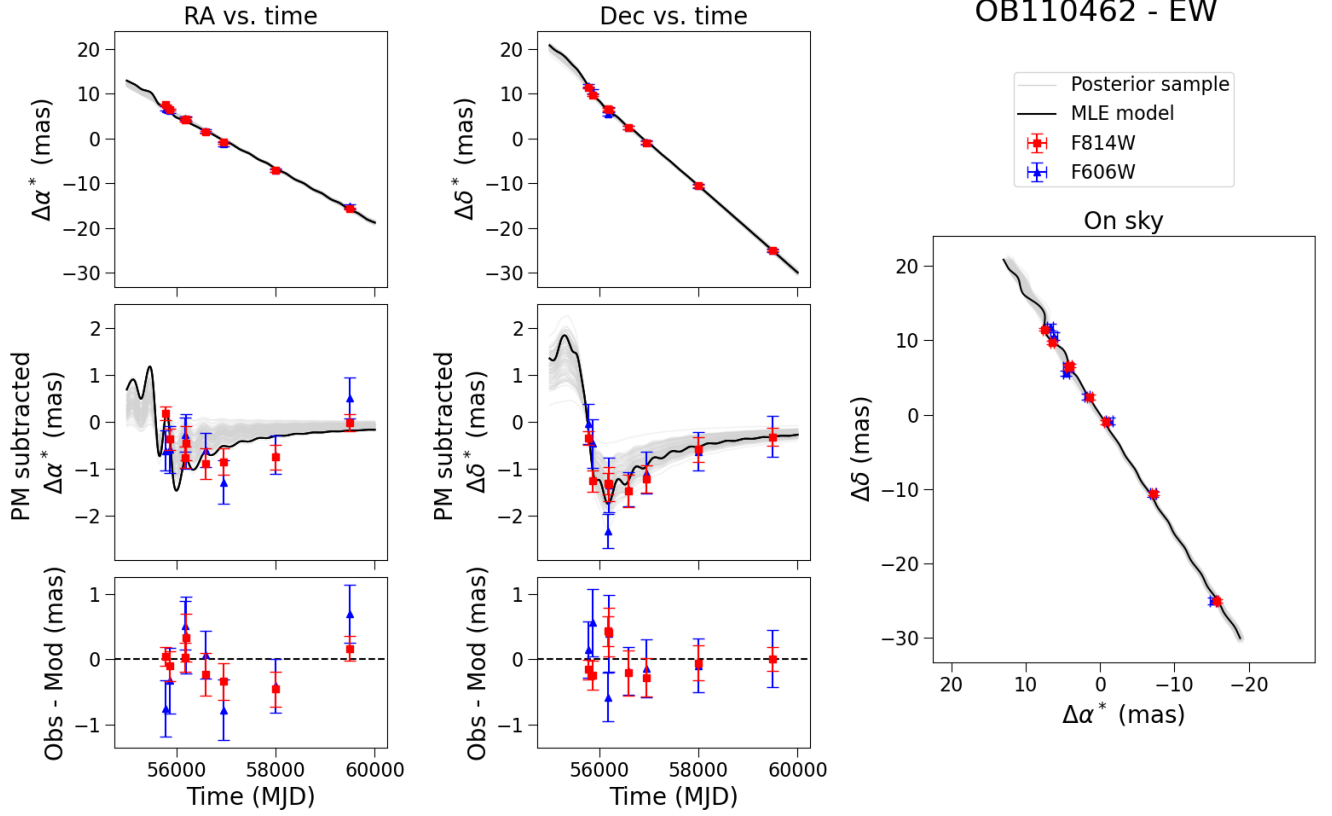


Figure 13. OB110462 astrometry, using the equally weighted likelihood. *Left column, top to bottom:* RA vs. time; RA vs. time with source proper motion subtracted; residuals to the maximum likelihood (MLE) model for RA vs. time fit. HST F814W astrometry data is shown in red; HST F606W astrometry data is shown in blue. The MLE model is shown in black. Fifty random draws from the posterior distribution are shown in light gray. *Middle column, top to bottom:* Same as left column, except Dec instead of RA. *Right panel:* astrometric lensing as seen on-sky. OB110462 shows a strong > 1 mas astrometric microlensing signal in the Dec direction.

astrometric microlensing. Assuming there is a transition from white dwarfs to neutron stars at $1.2M_{\odot}$ and neutron stars to BHs at $2.2M_{\odot}$, the relative probabilities of WD:NS:BH are 0:1:99 for the default weighted (DW) fit and 10:51:39 for the equally weighted (EW) fit.

The microlensing fit also yields information about the distance and transverse velocity of the lens. The lens is relatively nearby at a distance of d_L of [1.54 - 1.75] kpc or [0.69 - 1.32] kpc for the DW and EW solutions, respectively. The inferred lens velocity is $< 25 \text{ km s}^{-1}$ for both solutions with a slower velocity [2 - 13] km s^{-1} from the EW solution and a faster velocity of [17 - 23] km s^{-1} from the DW solution. In both cases, the velocities appear consistent with the compact object receiving little to no kick, although the line-of-sight velocity is not measurable.

A PSPL model is not the end of the story for OB110462. There is no PSPL model which can simultaneously fit both the photometry and the astrometry. Specifically, the ratio of $\pi_{E,E}$ to $\pi_{E,N}$ (i.e. the direction

of μ_{rel}) preferred by the photometry and astrometry are different. The best fit PSPL model for the default weight (DW) likelihood (Equation 29) fits the photometry very well, but leaves a strong ~ 0.5 mas coherent astrometric residual in RA (Figure 14). The best fit PSPL model signal for the equal weight (EW) likelihood (Equation 30) leaves a very small but very coherent ~ 0.03 mag residual in the photometry, but fits the astrometry in RA better than the default weight likelihood model. Although the light curve looks PSPL-like, it is possible the event is a very close binary lens, acting like a single lens and making the event look similar to PSPL. Or otherwise, a very wide binary lens or source acting as a perturbation to PSPL. As mentioned previously, we apply a constant positional offset to the F606W data in order to make it match up with the F814W data. However, this filter dependent positional difference may actually be astrophysical and consistent with a small contribution from a faint source or lens to the companion. Either way, both solutions indicate a NS or BH detection.

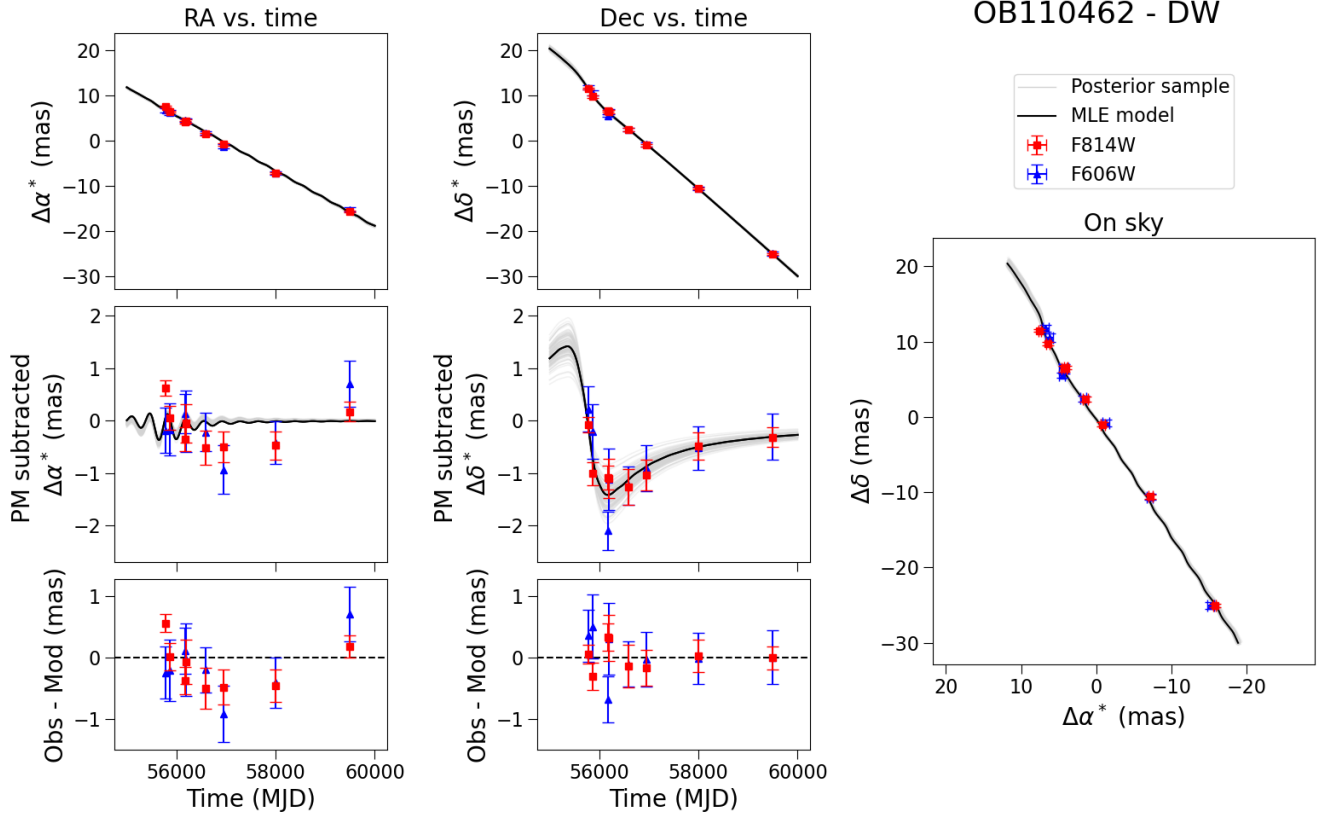


Figure 14. Same as Figure 13, but using the default weighted likelihood for OB110462.

Table 10. OB110462 DW Fit Values

Parameter	Med $^{+1\sigma}_{-1\sigma}$	MAP	MaxL
t_0 (MJD)	55759.28 $^{+0.64}_{-0.60}$	55760.20	55758.05
u_0	-0.07 $^{+0.003}_{-0.002}$	-0.07	-0.07
t_E (days)	290.12 $^{+2.67}_{-2.68}$	289.75	291.68
$\log_{10}(\theta_E/\text{mas})$	0.61 $^{+0.06}_{-0.06}$	0.50	0.60
π_S (mas)	0.11 $^{+0.02}_{-0.02}$	0.16	0.12
$\pi_{E,E}$	0.003 $^{+0.003}_{-0.003}$	0.008	-0.005
$\pi_{E,N}$	-0.13 $^{+0.006}_{-0.005}$	-0.13	-0.14
$x_{S0,E}$ (mas)	229.79 $^{+0.10}_{-0.09}$	229.77	229.81
$x_{S0,N}$ (mas)	-214.24 $^{+0.13}_{-0.14}$	-214.29	-214.26
$\mu_{S,E}$ (mas/yr)	-2.25 $^{+0.02}_{-0.02}$	-2.24	-2.25
$\mu_{S,N}$ (mas/yr)	-3.58 $^{+0.02}_{-0.02}$	-3.59	-3.57
$b_{SFF,O}$	0.05 $^{+0.0004}_{-0.0004}$	0.05	0.05
$m_{base,O}$ (mag)	16.41 $^{+0.001}_{-0.0001}$	16.41	16.41
$b_{SFF,H8}$	0.90 $^{+0.02}_{-0.02}$	0.89	0.91
$m_{base,H8}$ (mag)	19.86 $^{+0.006}_{-0.006}$	19.86	19.87
$b_{SFF,H6}$	0.94 $^{+0.02}_{-0.02}$	0.95	0.94
$m_{base,H6}$ (mag)	22.04 $^{+0.009}_{-0.009}$	22.05	22.04
M_L (M_\odot)	3.69 $^{+0.55}_{-0.51}$	3.01	3.44
π_L (mas)	0.65 $^{+0.08}_{-0.08}$	0.56	0.69
π_{rel} (mas)	0.54 $^{+0.08}_{-0.08}$	0.41	0.57
$\mu_{L,E}$ (mas/yr)	-2.36 $^{+0.12}_{-0.13}$	-2.48	-2.08
$\mu_{L,N}$ (mas/yr)	1.49 $^{+0.73}_{-0.67}$	0.39	1.44
$\mu_{rel,E}$ (mas/yr)	0.11 $^{+0.13}_{-0.12}$	0.24	-0.16
$\mu_{rel,N}$ (mas/yr)	-5.07 $^{+0.68}_{-0.73}$	-3.98	-5.02
θ_E (mas)	4.03 $^{+1.14}_{-1.16}$	3.17	4.01

Table 11. OB110462 EW Fit Values

Parameter	Med $^{+1\sigma}_{-1\sigma}$	MAP	MaxL
t_0 (MJD)	55747.18 $^{+7.48}_{-7.49}$	55734.19	55734.19
u_0	-0.11 $^{+0.02}_{-0.01}$	-0.13	-0.13
t_E (days)	277.25 $^{+12.58}_{-9.23}$	255.39	255.39
$\log_{10}(\theta_E/\text{mas})$	0.62 $^{+0.09}_{-0.12}$	0.74	0.74
π_S (mas)	0.11 $^{+0.02}_{-0.02}$	0.12	0.12
$\pi_{E,E}$	-0.07 $^{+0.05}_{-0.05}$	-0.17	-0.17
$\pi_{E,N}$	-0.23 $^{+0.05}_{-0.03}$	-0.30	-0.30
$x_{S0,E}$ (mas)	229.97 $^{+0.17}_{-0.18}$	230.24	230.24
$x_{S0,N}$ (mas)	-214.27 $^{+0.23}_{-0.22}$	-214.07	-214.07
$\mu_{S,E}$ (mas/yr)	-2.25 $^{+0.03}_{-0.03}$	-2.27	-2.27
$\mu_{S,N}$ (mas/yr)	-3.58 $^{+0.03}_{-0.03}$	-3.60	-3.60
$b_{SFF,O}$	0.05 $^{+0.003}_{-0.004}$	0.06	0.06
$m_{base,O}$ (mag)	16.41 $^{+0.007}_{-0.007}$	16.41	16.41
$b_{SFF,H8}$	0.95 $^{+0.05}_{-0.06}$	1.04	1.04
$m_{base,H8}$ (mag)	19.88 $^{+0.008}_{-0.008}$	19.88	19.88
$b_{SFF,H6}$	0.99 $^{+0.04}_{-0.06}$	1.04	1.04
$m_{base,H6}$ (mag)	22.03 $^{+0.01}_{-0.01}$	22.02	22.02
M_L (M_\odot)	2.12 $^{+0.74}_{-0.54}$	1.93	1.93
π_L (mas)	1.09 $^{+0.36}_{-0.33}$	2.03	2.03
π_{rel} (mas)	0.98 $^{+0.36}_{-0.33}$	1.90	1.90
$\mu_{L,E}$ (mas/yr)	-0.72 $^{+0.96}_{-0.94}$	1.67	1.67
$\mu_{L,N}$ (mas/yr)	1.54 $^{+1.29}_{-1.24}$	3.17	3.17
$\mu_{rel,E}$ (mas/yr)	-1.54 $^{+0.95}_{-0.96}$	-3.93	-3.93
$\mu_{rel,N}$ (mas/yr)	-5.13 $^{+1.24}_{-1.29}$	-6.77	-6.77
θ_E (mas)	4.14 $^{+1.00}_{-1.03}$	5.48	5.48

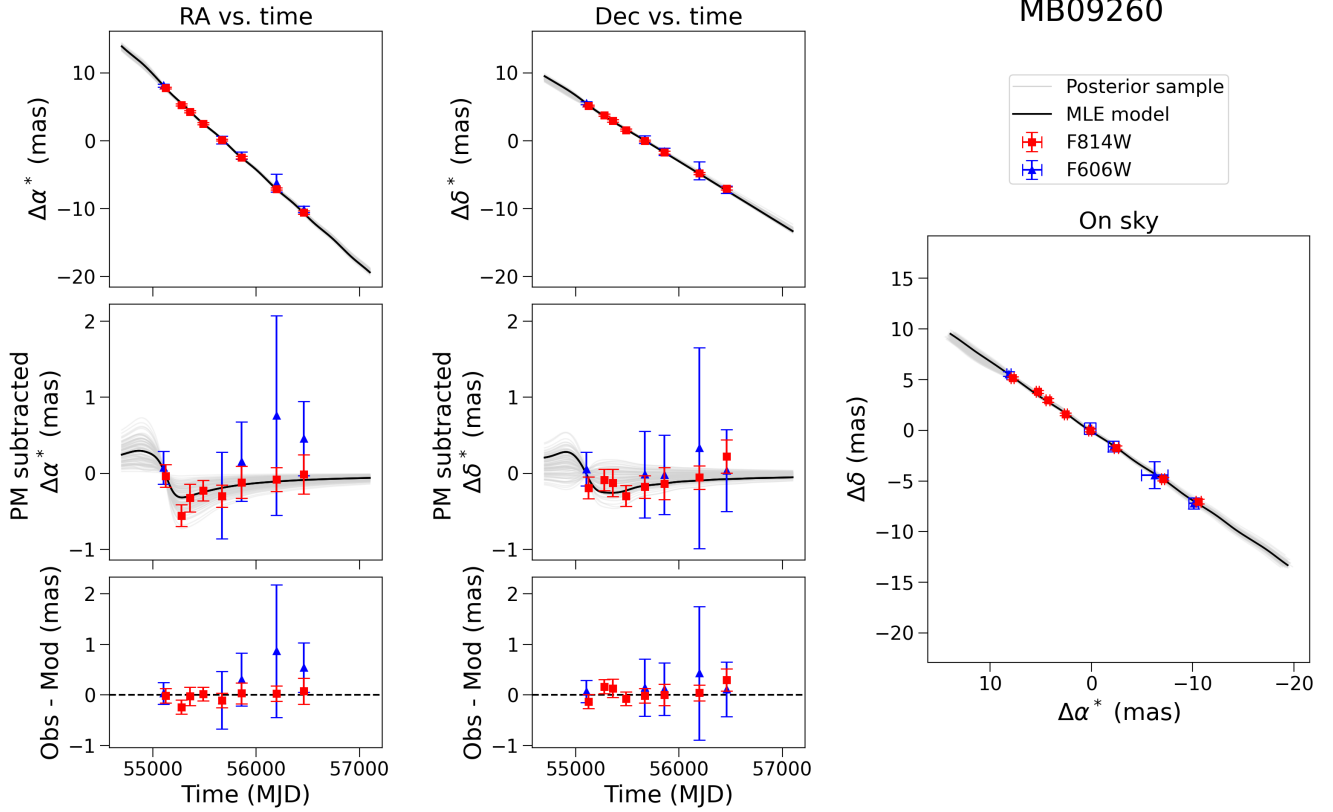


Figure 15. MB09260 astrometry. Same as Figure 13, but for MB09260. The astrometric signal is small, and around the limit of the precision of the F814W measurements.

5.2. MB09260

The data and model for MB09260 are shown in Figures 3 (photometry) and 15 (astrometry), and the fit posteriors are summarized in Table 12. The inferred Einstein crossing time t_E is $142.64^{+3.49}_{-2.87}$ days, the microlensing parallax π_E is $0.09^{+0.03}_{-0.01}$, the Einstein radius θ_E is $1.04^{+0.42}_{-0.39}$, and the lens mass is $1.37^{+0.74}_{-0.60} M_\odot$.¹³

The probability that MB09260 has a dark lens is at least 96%, and the probability of a stellar lens is at most 4%. The relative probabilities of Star:BD:WD:NS:BH are 4:0:38:44:14. Stellar lenses are only allowed below $1 M_\odot$. A white dwarf or neutron star is the most probable type of lens, with black holes possible but less likely.

5.3. MB10364

¹³ These are the values for the posteriors before they are split into modes, which is why the values differ from what is reported in Table 12. However, since these parameters are all globally unimodal, their distributions nearly identical across modes within the uncertainties, and neither mode is strongly favored, the values are not very different and we report the global median and uncertainties.

The data and model for MB10364 are shown in Figures 4 (photometry) and 16 (astrometry), and the fit posteriors are summarized in Table 13. The inferred Einstein crossing time t_E is $61.11^{+0.24}_{-0.24}$ days, the microlensing parallax π_E is $0.27^{+0.01}_{-0.01}$, the Einstein radius θ_E is $0.46^{+0.31}_{-0.21}$, and the lens mass is $0.21^{+0.14}_{-0.10} M_\odot$.

MB10364 is a low mass object, with the possibility of a neutron star or BH lens ruled out. The relative probabilities of Star:BD:WD are 36:29:36.¹⁴

5.4. OB110037

The data and model for OB110037 are shown in Figures 5 (photometry) and 17 (astrometry), the fit posteriors are summarized in Table 14. The inferred Einstein crossing time t_E is $92.78^{+2.63}_{-2.60}$ days, the microlensing parallax π_E is $0.37^{+0.01}_{-0.01}$, the Einstein radius θ_E is $1.24^{+0.36}_{-0.35}$, and the lens mass is $0.41^{+0.12}_{-0.12} M_\odot$.

The probability that OB110037 has a dark lens is at least 26%, and the probability of a stellar lens is at most 74%. The relative probabilities of Star:BD:WD:NS:BH

¹⁴ The probabilities sum to 101 due to rounding error when not reporting decimal places.

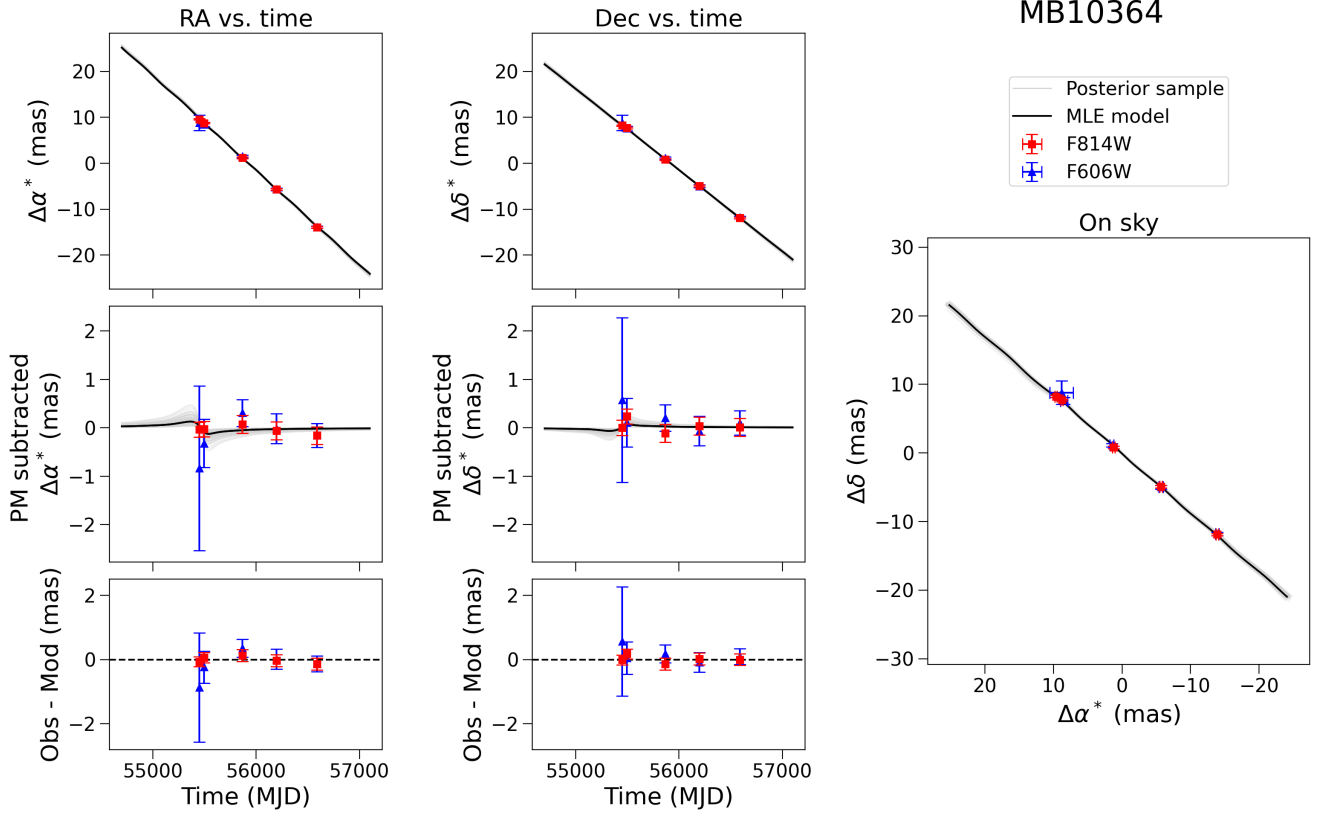


Figure 16. Same as Figure 13, but for MB10364. The astrometric signal is small, at or below the limit of the precision of the F814W measurements.

are 74:0:26:0:0. Stellar lenses are only allowed below $0.6M_{\odot}$, and white dwarfs are the only type of compact objects allowed.

The lightcurve of OB110037 appears to have some type of perturbation at MJD ~ 55690 . This feature is also apparent in the MOA lightcurve, raising our confidence that the lightcurve feature is real. If this is a binary lens signature, it would effectively be only a perturbation on the primary lightcurve, hence the parameters we inferred for the PSPL fit would still apply to the primary (i.e. more massive) lens. Re-analysis of this event with a binary model would be a worthwhile and interesting pursuit, but this is beyond the current scope of this paper. In addition, the astrometry fit, in particular for the F606W filter, is quite poor (Figure 17). Although the first 5 observations from 2011-2012 seem to agree between the two filters, a drastic difference that increases as time goes on begins in 2013-2017. This may also be attributed to a binary lens.

5.5. OB110310

The data and model for OB110310 are shown in Figures 6 (photometry) and 18 (astrometry), and the fit posteriors are summarized in Table 15. The inferred

Einstein crossing time t_E is $82.64^{+2.18}_{-1.50}$ days, the microlensing parallax π_E is $0.13^{+0.08}_{-0.04}$, and Einstein radius θ_E is $0.88^{+0.61}_{-0.42}$, and the lens mass is $0.78^{+0.71}_{-0.39}M_{\odot}$.¹⁵

The probability that OB110310 has a dark lens is at least 95%, and the probability of a stellar lens is at most 5%. The relative probabilities of Star:BD:WD:NS:BH are 5:3:65:22:5. Stellar lenses are only allowed below $1M_{\odot}$. A white dwarf or neutron star is the most probable type of lens, although brown dwarfs and black holes are still allowed at the low and high mass ends, respectively.

5.6. Source properties inferred from CMDs

As there is very little blending for all the targets in the high resolution F814W and F606W filters ($b_{SF} \sim 1$), the difference between the target and source on the CMD does not change much in color nor magnitude

¹⁵ These are the values for the posteriors before they are split into modes, which is why the values differ from what is reported in Table 15. However, since these parameters are all globally unimodal, their distributions nearly identical across modes within the uncertainties, and neither mode is strongly favored, the values are not very different and we report the global median and uncertainties.

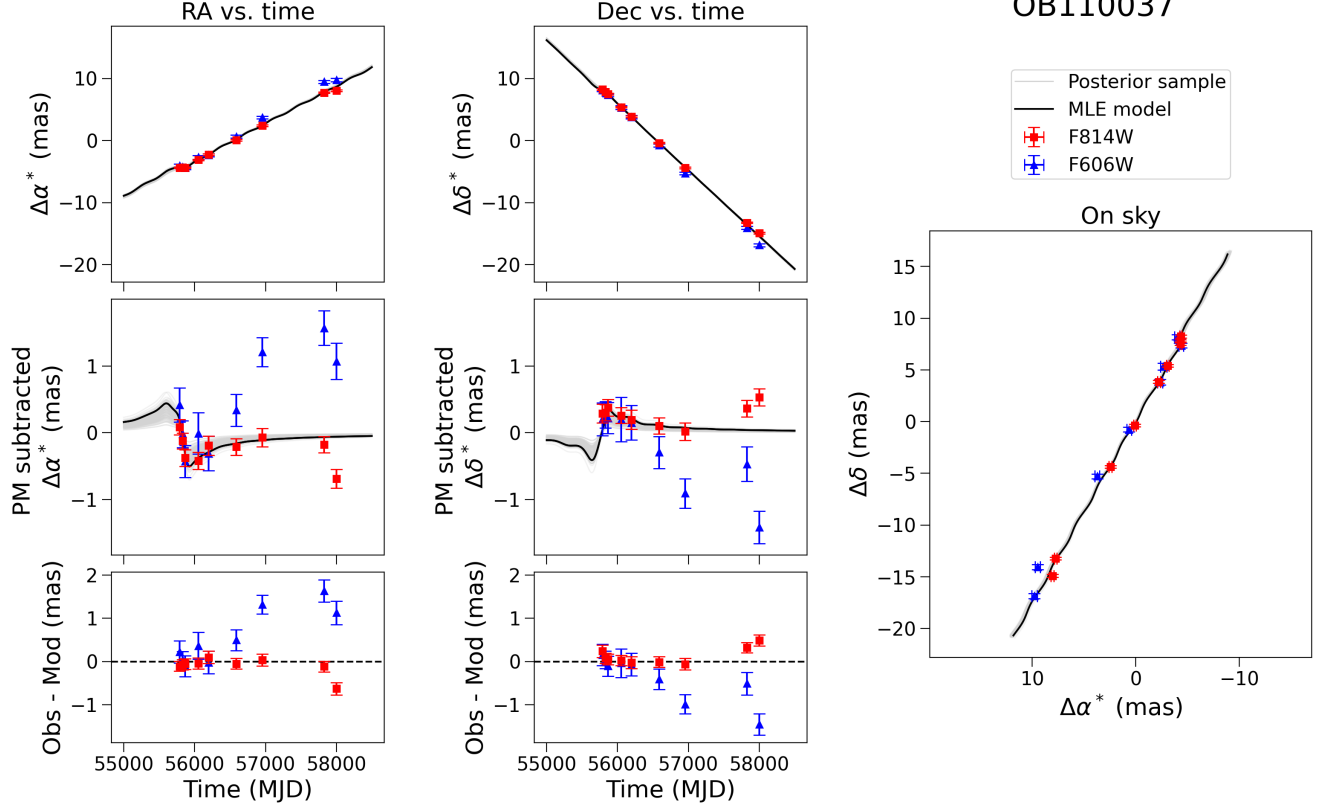


Figure 17. Same as Figure 13, but for OB110037. The photometry and astrometry seem to indicate this object is a binary.

space ($\Delta F_{814W} \lesssim 0.1$ mag and $\Delta(F_{606W} - F_{814W}) \lesssim 0.1$ mag, Figure 2). Based on a CMD analysis, the source stars in MB09260, MB10364, OB110037, and OB110310 are likely red giant stars in the bulge, as is typical for microlensing events in this part of the sky.

The source of OB110462 in the CMD is around the main sequence turnoff (MSTO) on the redder and more luminous side of the main sequence, suggesting it is most likely a giant or sub-giant star. However, a main sequence source could still be consistent.

The region of the CMD around the MSTO contains both foreground stars from the disk as well as bulge stars. We compare the proper motions of OB110462's source to stars in the bright blue foreground as well as in the bulge red giant branch to determine which population it most likely belongs to (Figure 19). The source is consistent with either population, although it falls within the bulk of the bulge population and more on the edge of the disk population, hence we consider it is most likely a bulge star. This is also consistent with the source parallax $\pi_S = 0.11 \pm 0.02$ inferred from the fit which also indicates the source is likely in the bulge.

MB09260 and OB110310 are in the the most highly reddened field, OB110462 and OB110037 are in intermediately reddened fields, and MB10364 is in the least

reddened field. This serves as a reminder that within the bulge the amount of extinction is highly variable, even over relatively small fields.

5.7. Verifying fit results with b_{SFF}

The fitting results are validated by comparing the best-fit OGLE or MOA I-band source flux fraction ($b_{SFF,O}$, $b_{SFF,M}$ in Tables 10 - 15) to the high-resolution F814W HST images (Figure 12). We only compare the F814W images, as it has a similar effective wavelength to OGLE I-band. Assuming a seeing disk radius of $\sim 0.65''$ for OGLE and $\sim 1.25''$ for MOA, we add up the flux from all stars detected by `hst1pass` within this radius. By also assuming all the flux from the target is from the source, we can estimate an upper limit on the source flux fraction by dividing the target flux by the total flux within the seeing disk radius. This gives an approximate estimate of the source flux fraction from HST, $b_{SFF,O,HST-derived}$ or $b_{SFF,M,HST-derived}$, that is compared to the values inferred from the lightcurve fit. This approach is sufficient to cross check our results, considering other differences prevent a perfect comparison (e.g. HST F814W is not a perfect match to the OGLE I filter).

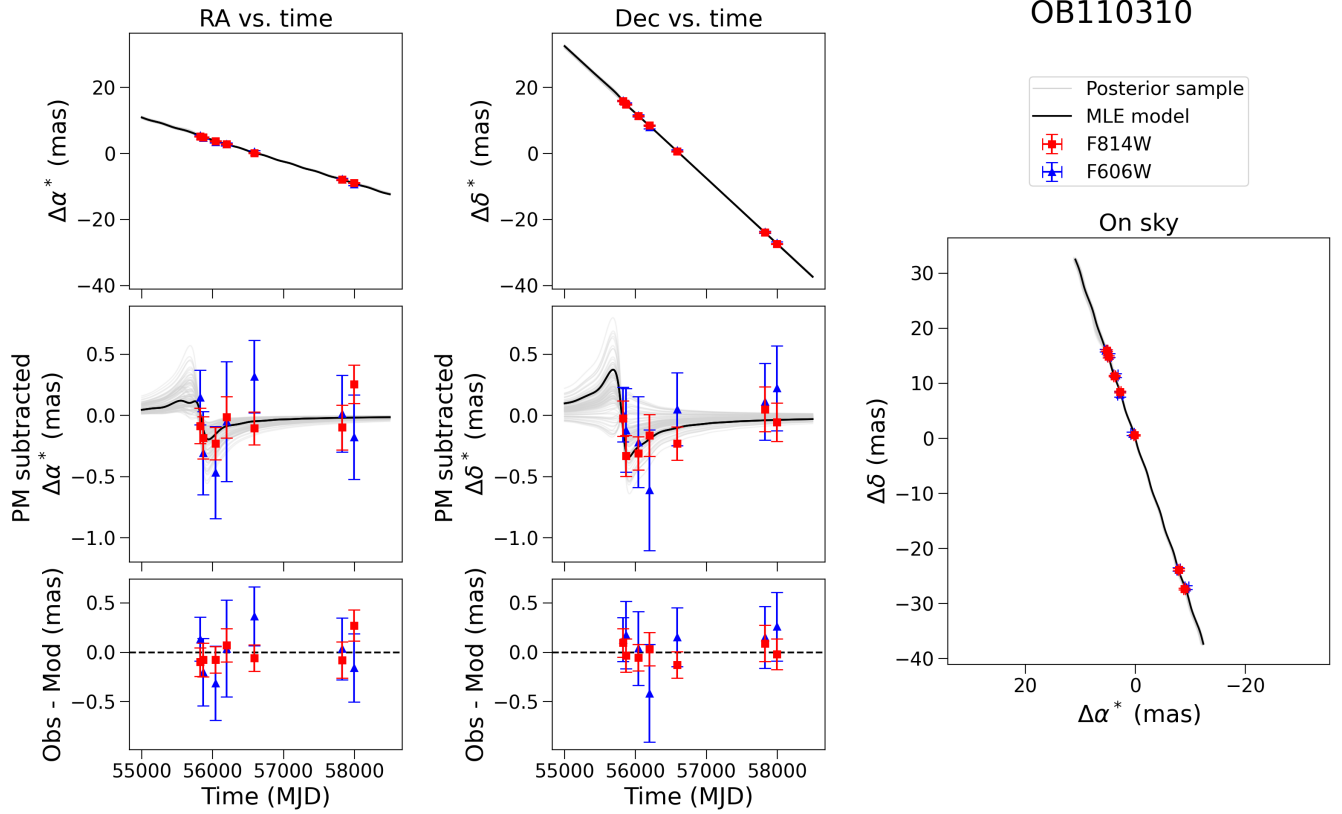


Figure 18. Same as Figure 13, but for OB110310. The astrometric signal is small, and around the limit of the precision of the F814W measurements.

From the photometry fits, MB10364 has $b_{SFF,M} \sim 0.93$, OB110037 has $b_{SFF,O} \sim 0.90$, OB110310 has $b_{SFF,O} \sim 0.97$, and OB110462 has $b_{SFF,O} \sim 0.5$, which are all close to the values inferred from the HST-derived values shown in Figure 12.

MB09260 has $b_{SFF,M} \sim 0.60$, which is higher than the upper limit of $b_{SFF,HST-derived} \sim 0.4$ in F814W at $1.25''$ estimated from the high resolution HST images. However, there is an abrupt transition from $b_{SFF,HST-derived} \sim 1$ to $b_{SFF,HST-derived} \sim 0.4$ (indicating a very bright star) at a radius of $1''$ from the source. The best-fit $b_{SFF,M} \sim 0.60$ falls within these two values, indicating that properly treating this situation by convolving the HST image with a MOA PSF would result in a better match. Hence, MB09260 seems consistent with the high resolution image.

The consistency between the source flux fraction inferred from the fits and the high resolution imaging provides an extra degree of confidence in the inferred fit values.

5.8. Prospects for resolving lens and source

By definition, microlensing means the source and lens are not resolvable. However, after many years, the lens

and source can separate far enough to be resolved (e.g. Batista et al. (2015); Bennett et al. (2015)). In the case of dark lenses, such as black holes, non-detections of the lens many years after the event can be used to place constraints on its properties (e.g. Abdurrahman et al. (2021)). For the five targets in this paper, we provide estimates to determine if and when taking late-time follow-up data would enable such analyses.

From the results of the fit, we can estimate the time necessary to resolve the source and lens t_{res} via

$$t_{\text{res}} = \theta_{\text{res}} / \mu_{\text{rel}} \quad (31)$$

where the relative proper motion μ_{rel} comes from fitting the data, and the minimum angular separation θ_{res} can be estimated using the Rayleigh criterion. For HST with a mirror diameter of 2.4m, θ_{res} corresponds to 63.53 mas in F606W and 85.35 mas in F814W.

Assuming there are no contaminating stars, $b_{SFF} = F_S / (F_S + F_L)$. Then the ratio of lens to source flux, or contrast, is $F_L / F_S = (1 - b_{SFF}) / b_{SFF}$. Note that $b_{SFF} > 1$ are allowed by some of the fits which would lead to an unphysical negative contrast. Thus, if a contrast is negative, it is instead capped at 0. In addition, the fit values for μ_{rel} and b_{SFF} are nearly independent,

Table 12. MB09260 Fit Values, Modes

Parameter	Mode 1			Mode 2		
	Med $^{+1\sigma}_{-1\sigma}$	MAP	\mathcal{L}_{max}	Med $^{+1\sigma}_{-1\sigma}$	MAP	\mathcal{L}_{max}
t_0 (MJD)	55099.19 $^{+1.40}_{-1.37}$	55099.27	55099.27	55099.33 $^{+1.26}_{-1.25}$	55099.99	55099.99
u_0	-0.09 $^{+0.02}_{-0.04}$	-0.07	-0.07	0.02 $^{+0.03}_{-0.06}$	-0.0002	-0.0002
t_E (days)	143.16 $^{+3.35}_{-2.95}$	141.71	141.71	142.37 $^{+3.43}_{-2.89}$	141.64	141.64
$\log_{10}(\theta_E/\text{mas})$	0.03 $^{+0.14}_{-0.20}$	0.24	0.24	0.008 $^{+0.15}_{-0.21}$	0.06	0.06
π_S (mas)	0.10 $^{+0.02}_{-0.02}$	0.12	0.12	0.10 $^{+0.02}_{-0.02}$	0.09	0.09
$\pi_{E,E}$	-0.08 $^{+0.010}_{-0.009}$	-0.08	-0.08	-0.08 $^{+0.009}_{-0.009}$	-0.07	-0.07
$\pi_{E,N}$	-0.02 $^{+0.03}_{-0.04}$	-0.005	-0.005	-0.04 $^{+0.04}_{-0.06}$	-0.06	-0.06
$x_{S0,E}$ (mas)	236.25 $^{+0.13}_{-0.12}$	236.43	236.43	236.20 $^{+0.13}_{-0.11}$	236.30	236.30
$x_{S0,N}$ (mas)	-692.07 $^{+0.11}_{-0.10}$	-692.15	-692.15	-692.01 $^{+0.12}_{-0.13}$	-691.91	-691.91
$\mu_{S,E}$ (mas/yr)	-5.00 $^{+0.05}_{-0.05}$	-5.07	-5.07	-4.99 $^{+0.05}_{-0.05}$	-5.05	-5.05
$\mu_{S,N}$ (mas/yr)	-3.38 $^{+0.04}_{-0.05}$	-3.34	-3.34	-3.39 $^{+0.05}_{-0.05}$	-3.44	-3.44
$b_{SFF,M}$	0.61 $^{+0.02}_{-0.02}$	0.60	0.60	0.60 $^{+0.02}_{-0.02}$	0.61	0.61
$m_{base,M}$ (mag)	17.43 $^{+0.003}_{-0.003}$	17.43	17.43	17.43 $^{+0.003}_{-0.003}$	17.42	17.42
$b_{SFF,H8}$	1.00 $^{+0.02}_{-0.03}$	0.99	0.99	0.99 $^{+0.02}_{-0.03}$	1.00	1.00
$m_{base,H8}$ (mag)	17.84 $^{+0.003}_{-0.004}$	17.83	17.83	17.84 $^{+0.003}_{-0.003}$	17.84	17.84
$b_{SFF,H6}$	1.03 $^{+0.02}_{-0.03}$	1.02	1.02	1.02 $^{+0.02}_{-0.03}$	1.02	1.02
$m_{base,H6}$ (mag)	20.75 $^{+0.007}_{-0.007}$	20.75	20.75	20.75 $^{+0.006}_{-0.007}$	20.75	20.75
M_L (M_\odot)	1.44 $^{+0.74}_{-0.59}$	2.70	2.70	1.30 $^{+0.74}_{-0.58}$	1.44	1.44
π_L (mas)	0.20 $^{+0.05}_{-0.04}$	0.25	0.25	0.20 $^{+0.06}_{-0.04}$	0.20	0.20
π_{rel} (mas)	0.09 $^{+0.04}_{-0.04}$	0.14	0.14	0.10 $^{+0.05}_{-0.04}$	0.11	0.11
$\mu_{L,E}$ (mas/yr)	-2.62 $^{+1.18}_{-0.93}$	-0.61	-0.61	-2.88 $^{+1.15}_{-0.94}$	-2.82	-2.82
$\mu_{L,N}$ (mas/yr)	-2.63 $^{+0.98}_{-0.91}$	-3.04	-3.04	-2.40 $^{+1.09}_{-1.12}$	-1.49	-1.49
$\mu_{rel,E}$ (mas/yr)	-2.40 $^{+0.95}_{-1.17}$	-4.46	-4.46	-2.11 $^{+0.94}_{-1.16}$	-2.23	-2.23
$\mu_{rel,N}$ (mas/yr)	-0.73 $^{+0.89}_{-1.01}$	-0.31	-0.31	-1.01 $^{+1.15}_{-1.09}$	-1.95	-1.95
θ_E (mas)	1.07 $^{+0.41}_{-0.40}$	1.73	1.73	1.02 $^{+0.41}_{-0.39}$	1.15	1.15
$\sum w_i$	0.42			0.58		
$\log \mathcal{Z}$	31613.22			31613.55		

Table 13. MB10364 Fit Values

Parameter	Med $^{+1\sigma}_{-1\sigma}$	MAP	MaxL
t_0 (MJD)	55445.13 $^{+0.12}_{-0.12}$	55445.06	55445.06
u_0	-0.008 $^{+0.01}_{-0.01}$	-0.004	-0.004
t_E (days)	61.11 $^{+0.24}_{-0.24}$	61.06	61.06
$\log_{10}(\theta_E/\text{mas})$	-0.33 $^{+0.22}_{-0.25}$	-0.40	-0.40
π_S (mas)	0.11 $^{+0.02}_{-0.02}$	0.11	0.11
$\pi_{E,E}$	-0.24 $^{+0.003}_{-0.003}$	-0.24	-0.24
$\pi_{E,N}$	0.12 $^{+0.01}_{-0.01}$	0.12	0.12
$x_{S0,E}$ (mas)	130.18 $^{+0.11}_{-0.10}$	130.13	130.13
$x_{S0,N}$ (mas)	-78.98 $^{+0.11}_{-0.10}$	-79.02	-79.02
$\mu_{S,E}$ (mas/yr)	-7.56 $^{+0.06}_{-0.06}$	-7.52	-7.52
$\mu_{S,N}$ (mas/yr)	-6.49 $^{+0.06}_{-0.06}$	-6.47	-6.47
$b_{SFF,M}$	0.93 $^{+0.007}_{-0.007}$	0.93	0.93
$m_{base,M}$ (mag)	15.02 $^{+0.00006}_{-0.00006}$	15.02	15.02
$b_{SFF,H8}$	0.99 $^{+0.02}_{-0.02}$	0.98	0.98
$m_{base,H8}$ (mag)	15.32 $^{+0.006}_{-0.006}$	15.32	15.32
$b_{SFF,H6}$	1.00 $^{+0.02}_{-0.02}$	1.01	1.01
$m_{base,H6}$ (mag)	16.50 $^{+0.006}_{-0.006}$	16.50	16.50
M_L (M_\odot)	0.21 $^{+0.14}_{-0.10}$	0.18	0.18
π_L (mas)	0.24 $^{+0.08}_{-0.06}$	0.22	0.22
π_{rel} (mas)	0.12 $^{+0.05}_{-0.05}$	0.11	0.11
$\mu_{L,E}$ (mas/yr)	-5.11 $^{+1.62}_{-1.09}$	-5.38	-5.38
$\mu_{L,N}$ (mas/yr)	-7.78 $^{+0.57}_{-0.89}$	-7.56	-7.56
$\mu_{rel,E}$ (mas/yr)	-2.46 $^{+1.09}_{-1.61}$	-2.13	-2.13
$\mu_{rel,N}$ (mas/yr)	1.29 $^{+0.88}_{-0.57}$	1.09	1.09
θ_E (mas)	0.46 $^{+0.31}_{-0.21}$	0.40	0.40

Table 14. OB110037 Fit Values

Parameter	Med $^{+1\sigma}_{-1\sigma}$	MAP	MaxL
t_0 (MJD)	55781.53 $^{+0.28}_{-0.30}$	55781.49	55781.49
u_0	-0.002 $^{+0.03}_{-0.02}$	-0.008	-0.008
t_E (days)	92.78 $^{+2.63}_{-2.60}$	93.31	93.31
$\log_{10}(\theta_E/\text{mas})$	0.09 $^{+0.11}_{-0.14}$	0.22	0.22
π_S (mas)	0.12 $^{+0.02}_{-0.02}$	0.11	0.11
$\pi_{E,E}$	-0.31 $^{+0.005}_{-0.005}$	-0.31	-0.31
$\pi_{E,N}$	0.21 $^{+0.01}_{-0.02}$	0.21	0.21
$x_{S0,E}$ (mas)	15.21 $^{+0.06}_{-0.06}$	15.23	15.23
$x_{S0,N}$ (mas)	-115.53 $^{+0.07}_{-0.07}$	-115.61	-115.61
$\mu_{S,E}$ (mas/yr)	2.19 $^{+0.02}_{-0.02}$	2.18	2.18
$\mu_{S,N}$ (mas/yr)	-3.87 $^{+0.02}_{-0.02}$	-3.86	-3.86
$b_{SFF,O}$	0.90 $^{+0.06}_{-0.05}$	0.89	0.89
$m_{base,O}$ (mag)	16.15 $^{+0.0003}_{-0.0003}$	16.15	16.15
$b_{SFF,H8}$	0.91 $^{+0.06}_{-0.05}$	0.90	0.90
$m_{base,H8}$ (mag)	16.33 $^{+0.003}_{-0.003}$	16.33	16.33
$b_{SFF,H6}$	0.84 $^{+0.06}_{-0.05}$	0.82	0.82
$m_{base,H6}$ (mag)	18.32 $^{+0.004}_{-0.003}$	18.31	18.31
M_L (M_\odot)	0.41 $^{+0.12}_{-0.12}$	0.55	0.55
π_L (mas)	0.58 $^{+0.14}_{-0.13}$	0.74	0.74
π_{rel} (mas)	0.46 $^{+0.14}_{-0.13}$	0.62	0.62
$\mu_{L,E}$ (mas/yr)	6.27 $^{+1.25}_{-1.17}$	7.59	7.59
$\mu_{L,N}$ (mas/yr)	-6.56 $^{+0.74}_{-0.78}$	-7.54	-7.54
$\mu_{rel,E}$ (mas/yr)	-4.07 $^{+1.17}_{-1.25}$	-5.42	-5.42
$\mu_{rel,N}$ (mas/yr)	2.69 $^{+0.78}_{-0.75}$	3.68	3.68
θ_E (mas)	1.24 $^{+0.36}_{-0.35}$	1.67	1.67

Table 15. OB110310 Fit Values, Modes

Parameter	Mode 1			Mode 2		
	Med $^{+1\sigma}_{-1\sigma}$	MAP	\mathcal{L}_{max}	Med $^{+1\sigma}_{-1\sigma}$	MAP	\mathcal{L}_{max}
t_0 (MJD)	55802.11 $^{+1.21}_{-1.57}$	55801.39	55801.39	55802.66 $^{+1.15}_{-1.17}$	55801.95	55801.95
u_0	-0.18 $^{+0.05}_{-0.07}$	-0.24	-0.24	-0.005 $^{+0.07}_{-0.08}$	-0.09	-0.09
t_E (days)	83.40 $^{+2.39}_{-1.83}$	83.23	83.23	82.20 $^{+1.66}_{-1.33}$	81.47	81.47
$\log_{10}(\theta_E/\text{mas})$	-0.05 $^{+0.24}_{-0.28}$	0.04	0.04	-0.06 $^{+0.21}_{-0.28}$	0.04	0.04
π_S (mas)	0.10 $^{+0.02}_{-0.02}$	0.10	0.10	0.10 $^{+0.02}_{-0.02}$	0.09	0.09
$\pi_{E,E}$	-0.08 $^{+0.01}_{-0.01}$	-0.09	-0.09	-0.09 $^{+0.01}_{-0.02}$	-0.10	-0.10
$\pi_{E,N}$	-0.08 $^{+0.06}_{-0.08}$	-0.14	-0.14	-0.11 $^{+0.10}_{-0.09}$	-0.21	-0.21
$x_{S0,E}$ (mas)	-104.56 $^{+0.12}_{-0.10}$	-104.62	-104.62	-104.62 $^{+0.09}_{-0.09}$	-104.58	-104.58
$x_{S0,N}$ (mas)	-183.61 $^{+0.13}_{-0.11}$	-183.53	-183.53	-183.57 $^{+0.13}_{-0.14}$	-183.49	-183.49
$\mu_{S,E}$ (mas/yr)	-2.41 $^{+0.02}_{-0.03}$	-2.39	-2.39	-2.40 $^{+0.02}_{-0.02}$	-2.43	-2.43
$\mu_{S,N}$ (mas/yr)	-7.26 $^{+0.03}_{-0.03}$	-7.26	-7.26	-7.26 $^{+0.03}_{-0.03}$	-7.28	-7.28
$b_{SFF,O}$	0.97 $^{+0.02}_{-0.02}$	0.98	0.98	0.96 $^{+0.02}_{-0.03}$	0.96	0.96
$m_{base,O}$ (mag)	18.41 $^{+0.005}_{-0.005}$	18.41	18.41	18.41 $^{+0.005}_{-0.005}$	18.41	18.41
$b_{SFF,H8}$	1.02 $^{+0.02}_{-0.03}$	1.04	1.04	1.02 $^{+0.02}_{-0.03}$	1.04	1.04
$m_{base,H8}$ (mag)	18.62 $^{+0.003}_{-0.003}$	18.61	18.61	18.62 $^{+0.003}_{-0.003}$	18.62	18.62
$b_{SFF,H6}$	1.02 $^{+0.02}_{-0.03}$	1.04	1.04	1.02 $^{+0.02}_{-0.03}$	1.05	1.05
$m_{base,H6}$ (mag)	21.34 $^{+0.006}_{-0.006}$	21.34	21.34	21.34 $^{+0.006}_{-0.006}$	21.34	21.34
M_L (M_\odot)	0.90 $^{+0.77}_{-0.47}$	0.83	0.83	0.71 $^{+0.62}_{-0.34}$	0.58	0.58
π_L (mas)	0.21 $^{+0.11}_{-0.06}$	0.28	0.28	0.23 $^{+0.13}_{-0.07}$	0.35	0.35
π_{rel} (mas)	0.11 $^{+0.10}_{-0.06}$	0.18	0.18	0.12 $^{+0.13}_{-0.07}$	0.25	0.25
$\mu_{L,E}$ (mas/yr)	0.21 $^{+2.20}_{-1.30}$	0.22	0.22	-0.16 $^{+1.67}_{-1.06}$	-0.30	-0.30
$\mu_{L,N}$ (mas/yr)	-4.79 $^{+2.45}_{-1.96}$	-3.22	-3.22	-4.57 $^{+2.32}_{-2.31}$	-2.84	-2.84
$\mu_{rel,E}$ (mas/yr)	-2.61 $^{+1.30}_{-2.22}$	-2.60	-2.60	-2.24 $^{+1.06}_{-1.69}$	-2.13	-2.13
$\mu_{rel,N}$ (mas/yr)	-2.46 $^{+1.97}_{-2.48}$	-4.04	-4.04	-2.69 $^{+2.33}_{-2.34}$	-4.44	-4.44
θ_E (mas)	0.90 $^{+0.66}_{-0.43}$	1.10	1.10	0.87 $^{+0.55}_{-0.41}$	1.10	1.10
$\sum w_i$	0.43			0.57		
$\log \mathcal{Z}$	24631.66			24631.92		

and so these results for t_{res} and F_L/F_S can be thought of as independent.

The resolving time after photometric peak and maximum contrast in the F814W and F606W HST filters for each target are listed in Table 16. Currently, only OB110462 could potentially have its source-lens pair resolved in F606W; it has the shortest resolving time, as well as the highest lens-source contrast. All the other targets have lens-source resolving times at least 15 years post-photometric peak. In addition, since they all have very high source flux fractions b_{SFF} , their lens-source contrasts are very low, which means even after enough time has passed for the lens and source to separate, a luminous lens would be difficult to detect. Thus, high resolution imaging of OB110037 in the near future could confirm the results of the fit if the separating source and lens could be detected. For the other targets, the absence of any lens detection would imply consistency with the results presented here, but could not confirm them; however, any detection of a lens would imply the fit results here are incorrect.

6. DISCUSSION

OB110462 is the first definitive detection of a compact object discovered with astrometric microlensing. Depending on the fit (See §4.3), it is either a neutron

Table 16. Lens/source resolvability

Parameter	Resolving time t_{res} (yr)		Contrast (F_L/F_S)	
	F814W	F606W	F814W	F606W
MB09260	32.08 $^{+19.38}_{-9.20}$	23.88 $^{+14.42}_{-6.85}$	0.01 $^{+0.03}_{-0.00}$	0.00 $^{+0.01}_{-0.00}$
MB10364	30.72 $^{+24.58}_{-12.19}$	22.87 $^{+18.29}_{-9.07}$	0.01 $^{+0.02}_{-0.00}$	0.00 $^{+0.02}_{-0.00}$
OB110037	17.45 $^{+6.92}_{-4.01}$	12.99 $^{+5.15}_{-2.98}$	0.10 $^{+0.07}_{-0.07}$	0.20 $^{+0.08}_{-0.07}$
OB110310	22.03 $^{+19.49}_{-8.95}$	16.40 $^{+14.61}_{-6.66}$	0.00 $^{+0.01}_{-0.00}$	0.00 $^{+0.01}_{-0.00}$
OB110462	16.63 $^{+0.78}_{-0.75}$	12.38 $^{+0.58}_{-0.56}$	0.12 $^{+0.01}_{-0.01}$	0.07 $^{+0.01}_{-0.01}$

star (51% probability for the EW fit, 1% probability for the DW fit), a black hole (39% probability for the EW fit, 99% probability for the DW fit), or a white dwarf (10% probability for the EW fit). MB09260 and OB110310 are mostly likely white dwarfs or neutron stars, although a NS-BH mass gap object cannot be ruled out. MB10364 and OB110037 are definitively low mass objects; OB110037 is most likely a star or white dwarf, while MB10364 is either a star, brown dwarf, or white dwarf.

Here we discuss the lensed source population (§5.6), the observed BH yield as compared to theoretical expectations (§6.1), the resulting constraints and questions it raises about the Galactic BH population (§6.2 and

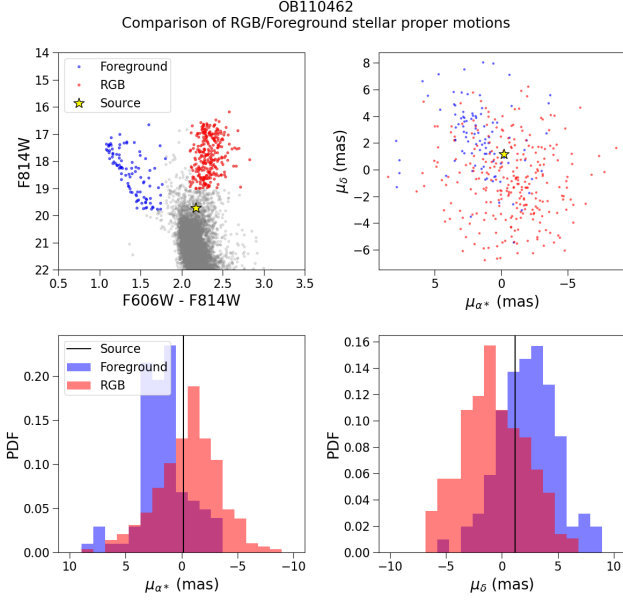


Figure 19. *Top left:* CMD with the blue foreground and red giant branch (RGB) stars marked. The source color and magnitude as gotten from the fitting is shown as the yellow star. *Top right:* VPD of the foreground and RGB stars. The source proper motions as gotten from the fitting is shown as the yellow star. *Bottom left:* Histogram of the foreground and RGB RA proper motions. The proper motion of the source is shown in the black line. *Bottom right:* Same as bottom left, but for Dec.

§6.3), and a look toward the future of BH microlensing searches (§6.4 and §6.5).

6.1. Comparison to simulations

6.1.1. π_E - t_E - $\delta_{c,max}$

As described in Lam et al. (2020), black hole candidates can be identified photometrically due to their long t_E and small π_E and confirmed astrometrically with the addition of a measurement of $\delta_{c,max}$. The 1–2–3 σ contours from the fits in π_E – t_E and π_E – $\delta_{c,max}$ are plotted above simulated microlensing events from PopSyCLE Lam et al. (2020) in Figure 16. Considering π_E – t_E and π_E – $\delta_{c,max}$ space confirms the interpretation of MB10364 and OB110037 in Table 9 as definitive non-BHs, due to their large π_E and small $\delta_{c,max}$. The uncertainty in π_E for OB110310 as well as only having an upper limit on $\delta_{c,max}$ is what makes it hard to definitively rule out high or low mass lenses. MB09260 lands in a regime mostly dominated by white dwarfs and neutron stars, but also with contamination of other objects. OB110462 falls solidly within the mass gap; its position in π_E – t_E is unusual as it has a relatively large π_E for a BH.

Table 17. Fraction of expected BH detections vs. t_E from PopSyCLE simulation

Target	t_E range	% BH
MB09260	$135 < t_E < 155$ days	50
MB10364	$60 < t_E < 62$ days	14
OB110037	$87 < t_E < 100$ days	12
OB110310	$78 < t_E < 90$ days	20
OB110462 DW	$283 < t_E < 297$ days	50
OB110462 EW	$253 < t_E < 322$ days	14

NOTE—For each target, the t_E range is the median $\pm 3\sigma$. For OB110462 there are two entries, one with equal weighting to the astrometry and photometry data (OB110462 EW) and one with the default weighting of astrometry and photometry data (OB110462 DW). See §4.3 for details.

6.1.2. Number of detected BHs

We next compare our observed BH yield to the theoretical expectation from PopSyCLE simulations from Lam et al. (2020) as a function of t_E . For a sample of simulated events that would be observable by OGLE (see Table 4 of Lam et al. (2020)), we calculate the fraction of BHs as a function of the Einstein crossing time t_E . Assuming the OGLE observability criterion for the MOA sample is not strictly correct; however, OGLE and MOA often observe an overlapping set of events, so this approximation should suffice.

We wish to calculate the probability of detecting k BHs in our sample, given n samples where the probability of detecting a BH in the i -th sample is p_i . This is described by a Poisson binomial distribution, which characterizes a “success/no success” experiment with n independent trials, where the i -th trial has probability p_i of success (Wang 1993). The probability of k successes is given by

$$P(K = k) = \sum_{A \in F_k} \prod_{i \in A} p_i \prod_{j \in A^c} (1 - p_j) \quad (32)$$

where F_k is the set of all subsets of k integers that can be selected from the set $\{1, \dots, n\}$, i.e.

$$F_k = \{A : A \subseteq \{1, \dots, n\}, |A| = k\}$$

where $|A|$ is the number of elements in A . A^c is the complement of A . In the limit where all p_i are equal, the Poisson binomial distribution is the definition of the ordinary binomial distribution.

In our case, there are $n = 5$ independent trials (i.e. targets). We calculate the probability of success p_i (i.e. BH detection) using PopSyCLE. We define the success probability for the i -th target as the fraction of BH lensing events in PopSyCLE over the range of t_E inferred from the fit

$$\text{med}(t_E) - 3\sigma < t_E < \text{med}(t_E) + 3\sigma.$$

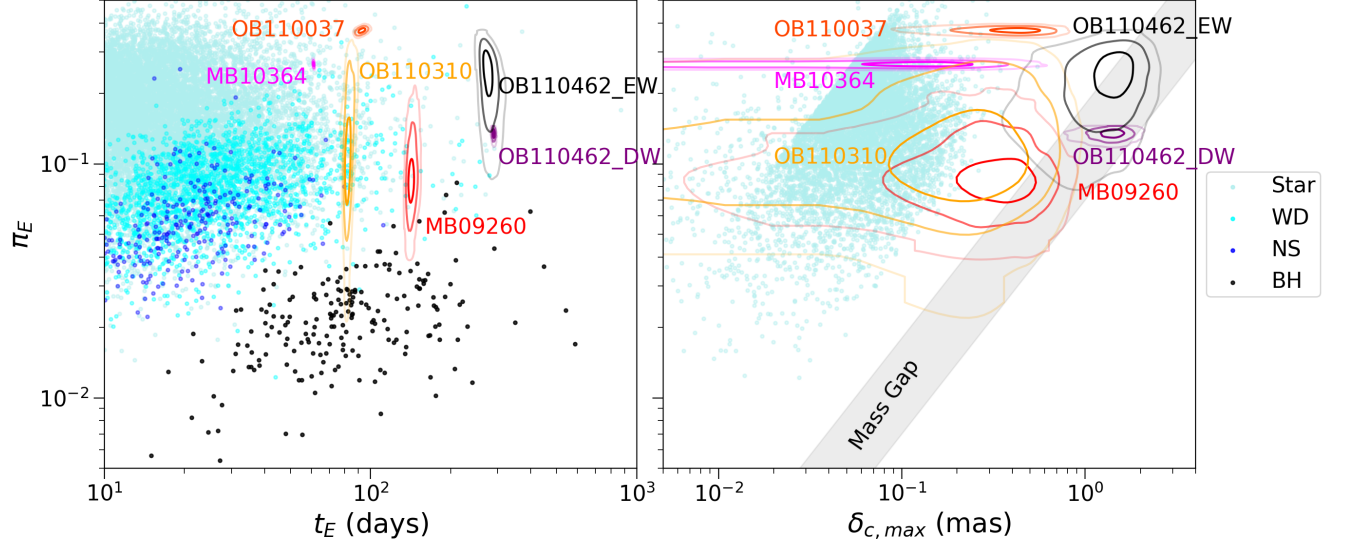


Figure 20. Microlensing parallax π_E vs. Einstein crossing time t_E (left) and maximum astrometric shift $\delta_{c,max}$ (right). Points are from the PopSyCLE simulation. Contours are $1 - 2 - 3\sigma$ (39.3-86.5-98.9%) credible regions from the fits. OB110462 is the best BH-candidate, falling solidly in the NS-BH mass gap. MB09260 and OB110310 are most likely white dwarfs or neutron stars, although due to uncertainty in π_E and $\delta_{c,max}$ higher and lower mass lenses cannot be definitively ruled out. OB110037 and MB10364 are not black holes as they have very large π_E , as well as relatively short t_E and small $\delta_{c,max}$.

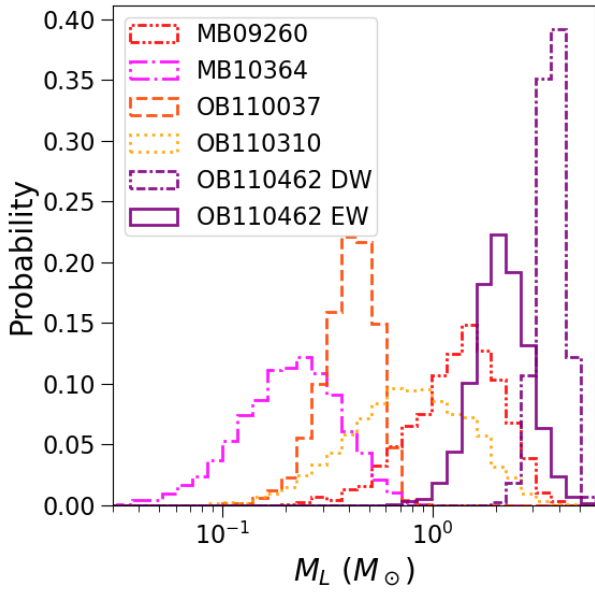


Figure 21. Lens mass posterior probabilities for the targets. There are two fits for OB110462, one with equal weighting to the astrometry and photometry (OB110462 EW) and one with the astrometry fit based on priors from the photometry fit (OB110462 DW). See §4.3 for details.

The probabilities of BH detection for each target are listed in Table 17.

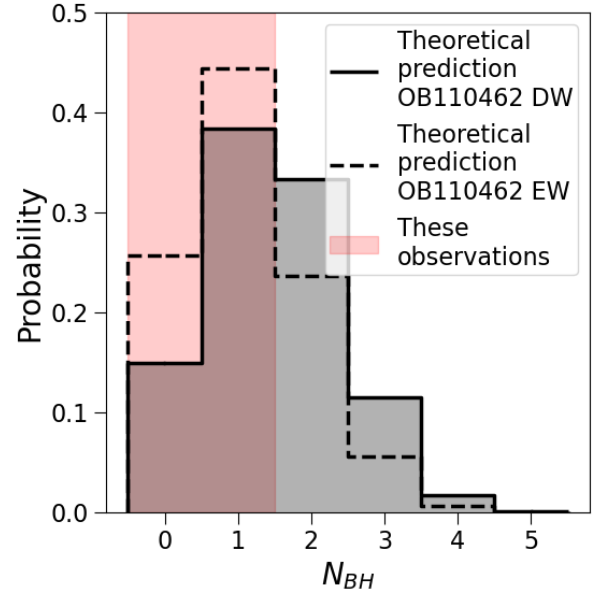


Figure 22. Probability of detecting N BHs as calculated from the PopSyCLE simulation. Our observation of 0 or 1 BH is consistent with the prediction.

The results of evaluating Eq. 32 for $k = 0, \dots, 5$ detections assuming success probabilities p_i is presented in Figure 22. PopSyCLE predicts 2×10^8 BHs in the Milky Way ranging from $\sim 5 - 16 M_\odot$ Lam et al. (2020). There are no mass gap objects in the simulation, and hence no

exact OB110462 analogue. Hence, we consider the probabilities of making one mass gap detection as somewhere between 0 or 1 in PopSyCLE. The probability of detecting 0 or 1 BHs are $\sim 20\%$ and $\sim 40\%$, respectively. This estimate appears consistent with our single detection of a NS-BH mass gap object.

6.2. OB110462: first isolated mass gap object

The posterior on the lens mass of OB110462 falls largely within the NS-BH mass gap of $\sim 2-5M_{\odot}$. LIGO has found mass gap objects both as the merger remnant ($\sim 3M_{\odot}$ in GW170917 (Abbott et al. 2017) and $\sim 3.4M_{\odot}$ in GW190425 (Abbott et al. 2020a)), and in the merger components ($\sim 2.6M_{\odot}$ in GW190814 (Abbott et al. 2020b)). Non-interacting mass gap BHs of $\sim 3M_{\odot}$ with red giant companions have also been detected in the Milky Way (Thompson et al. 2019; Jayasinghe et al. 2021). With a mass of 1.6 - 4.2 M_{\odot} , the lens of OB110462 is the first measured isolated Galactic NS or mass gap BH.

Further observations of OB110462 are well worth pursuing. The addition of the 2021 astrometric observations of OB110462 are crucial to the proper motion fits as they extend the temporal baseline by 50%, from 6 years to 10 years (Lam & Lu 2021b). The remaining data from HST Cycle 29 program GO-16760 to be taken in Fall 2022 (§2.4) will help further extend the temporal baseline by another year and provide further information on the astrometric signal.

Additional follow-up observations in the X-ray can place limits on accretion from the ISM (Agol & Kamionkowski 2002). Maeda et al. (2005) and Nucita et al. (2006) looked for X-rays at the location of BH microlensing candidate MACHO-96-BLG-5 reported in Bennett et al. (2002). Neither detected any X-rays. Using the ACIS instrument on Chandra, Maeda et al. (2005) inferred an upper limit at the 99% confidence level of $\sim 10^{-14}$ ergs/s/cm² and 4.7×10^{-4} counts/s in the 0.3-8 keV band. (Nucita et al. 2006) used the EPIC instrument on XMM-Newton and inferred an upper limit at the 99.8% confidence level of 9.10×10^{-15} to 1.45×10^{-14} ergs/s/cm² in the 0.2-10 keV energy band.

We searched several X-ray catalogs that have observed at OB110462's coordinates to determine whether there are any coincident sources. OB110462 was not detected as an X-ray source in any of the following catalogs:

- Chandra Source Catalog 2.0¹⁶ (Evans et al. 2019a,b). The limiting sensitivity provides an upper limit of 1.91×10^{-14} erg/s/cm² at 0.5-7.0 keV.
- XMM-Newton Science Archive¹⁷ (Sarmiento et al. 2019). This provides an upper limit of 1.52×10^{-14} erg/s/cm² and $< 1.38 \times 10^{-3}$ counts/s at 0.2 - 12.0 keV.
- Swift XRT Point Source Catalogue¹⁸ (Evans et al. 2020). This provides an upper limit of 2.4×10^{-3} counts/s at 0.3 - 10 keV.

OB110462's coordinates are not in the eROSITA-DE Early Data Release catalog¹⁹.

We also searched the Australia Telescope National Facility Pulsar Catalogue²⁰ (Manchester et al. 2005) Version 1.65 for any pulsars coincident with the target. There are no coincident pulsars; the nearest pulsar is 0.55 deg away.

6.3. Understanding the Galactic BH population

The mass distribution of BHs in the Milky Way has been derived from dynamical mass measurements of BHs of low-mass X-ray binaries (LMXBs). Özel et al. (2010) uses a sample of 16 LMXBs to infer a narrow mass distribution centered around $8M_{\odot}$, finding evidence for a mass gap in the $2-5M_{\odot}$ lower mass range, and attribute the lack of higher mass systems due to evolutionary channel effects. However, this result is highly uncertain on both the low and high mass ends. Kreidberg et al. (2012) cautions that systematic errors in the analysis of LMXB systems could push their inferred masses high, artificially creating the mass gap. Jonker et al. (2021) also identifies potential observational biases that prevent measurement of high-mass LXMB systems. Additionally, LXMBs occupy a very small and specific part of BH evolutionary parameter space, and the BHs found in those systems are likely not representative of the Galactic BH population as a whole.

There are active and future searches to uncover BHs outside of closely interacting X-ray binary systems. We first consider searches for isolated BHs with microlensing, as discussed in this paper. From our sample of 5, we have only 1 detection of a mass gap object; all other lenses are lower mass. In addition, we only have 1 detection of a > 1 mas astrometric shift; most of the remain-

¹⁶ <https://cxc.harvard.edu/csc/>

¹⁷ <http://nxsas.esac.esa.int/nxsa-web/#search>

¹⁸ <https://www.swift.ac.uk/2SXPS/>

¹⁹ <https://erosita.mpe.mpg.de/edr/>

²⁰ <https://www.atnf.csiro.au/research/pulsar/psrcat/>

ing detections are at the ~ 0.5 mas level, near the limit of HST’s precision. Lu et al. in prep, from a separate analysis of another set of 4 BH candidates, make similar conclusions from their sample. If the BH mass function truly peaks at $8M_{\odot}$, it should be relatively easy to detect such systems at our level of astrometric precision. In addition, selecting candidates from microlensing as well as ensuring they have long t_E should doubly bias us toward high-mass lenses. The fact that the objects being found are primarily low mass despite these selection effects hint at some tension in our understanding of the BH mass function, kick velocity, massive star evolution and death. Although the sample size is still small, microlensing searches for isolated BHs are pointing toward the absence of a lower mass gap (i.e. OB110462), as well as a dearth of higher BH masses.

Several other BH candidates have been identified using microlensing, most notably MACHO-96-BLG-5, MACHO-98-BLG-6 (Bennett et al. 2002), and MACHO-99-BLG-22/OGLE-1999-BUL-32 (Mao et al. 2002)). Poindexter et al. (2005) finds that MACHO-99-BLG-22 is likely a BH, MACHO-96-BLG-5 is possibly a BH, and MACHO-98-BLG-6 is most likely not a BH, with BH lens probabilities of 78%, 37%, and 2%, respectively. On the other hand, (Abdurrahman et al. 2021) find that MACHO-96-BLG-5 and MACHO-98-BLG-6 are still good BH candidates, ruling out non-BH lenses for source-lens relative proper motions larger than 2.5 mas/yr.

There are many active searches for BHs in detached/non-interacting binary systems. To date, radial velocity searches have detected two objects which fall within the mass gap (Thompson et al. 2019; Jayasinghe et al. 2021), which also suggest a paucity of higher-mass systems. Complementary searches using ellipsoidal variables (Rowan et al. 2021) also suggest that higher-mass systems are rare. This mirrors the situation found by microlensing studies—very large changes in RV should be easily detectable and make detection of an $8M_{\odot}$ object easier than a lower mass $3M_{\odot}$ object.

Astrometric searches for detached binaries are also eagerly anticipated with Gaia (e.g. Yamaguchi et al. (2018); Yalinewich et al. (2018); Wiktorowicz et al. (2020)). It will be very fruitful to compare the results of those searches to the X-ray transient, microlensing, and RV searches.

6.4. Improving experimental strategy and design

6.4.1. Multi-filter astrometry

In contrast to photometric observations, multi-filter astrometry is not routinely obtained, as astrometric observations are expensive and facilities with the requisite

precision are rare. This is one of the first projects to explore the impact of different filters on relative astrometry. The source of the discrepancies between the F606W and F814W filters is unclear, as is whether these discrepancies are astrophysical in nature (e.g. binaries with different color), instrumental systematics (e.g. uncorrected CTE), statistical scatter (in particular underestimated uncertainties), or some combination of all three. The existing microlensing data set is heterogeneous in terms of number of frames per filter and exposure time, making it difficult to be certain these differences are not in part driving the differences between the F606W and F814W filter astrometry. However, it demonstrates that multi-filter astrometry is worth continuing to pursue in future astrometric microlensing studies, especially in a more homogeneous manner. For example, it could help break degeneracies between certain types of binaries lenses or sources. In addition, multi-filter observations may be interesting in astrometric studies of globular clusters or the Galactic Center.

6.4.2. CTE correction

As mentioned in §3.1, the CTE correction in the `_f1c` files is not perfect. Future pursuits will explore other methods of correction. For example, a re-analysis of OB110462 using a tabular correction for CTE instead of the `_f1c` files (Anderson 21B ISR). In addition, trying to fix CTE via a magnitude-dependent astrometric alignment is another avenue that is being explored.

6.4.3. Observational strategy

For these precise astrometric measurements, taking good observations is critical. The lens mass constraints for several of the targets are only upper limits, as the astrometric shifts were so small, and undetectable at the precision of the measurements. A dominant source of astrometric uncertainty with HST WFC3-UVIS observations is the undersampling of the PSF. It has been shown that there is a floor in the astrometric precision that can be achieved, even at high SNR, when only a few exposures are used (Hosek et al. 2015). As the majority of the observations in each filter had 4 or less exposures, this limited the achievable astrometric precision for several of the targets, in particular OB110462. Increasing the number of exposures and implementing small dithers to sample different pixel phases reduces this floor as $\sqrt{N_{\text{dithers}}}$.

In addition, the effects of CTE are worsening with time. Actively mitigating CTE in observations is even more important than before, rather trying to correct afterwards.

6.4.4. Event selection

Although all events presented in this work were selected to have $t_E > 200$ days (Sahu 2009), the inferred t_E values for 4 of the 5 events did not satisfy this criteria. As a result, the true t_E range probed extended down to $t_E = 60$ days, and did not sample the t_E range that maximizes the expected yield of BHs ($t_E \gtrsim 100$ days). Only MB09260 and OB110462 had $t_E > 100$ days, weakening the constraints on the BH fraction. Improving predictions of t_E before the photometric peak of the event is crucial to building better samples of BH candidates for astrometric follow-up. More work in this area (both empirical and theoretical) is needed to enable better target selection.

A secondary concern is the target field itself. A sufficient number of reference stars is needed, hence the field in the immediate vicinity of the target must be sufficiently crowded. However, the magnitude range of those nearby stars must also be similar to the target. Because of the steepness of the luminosity function, bright targets or targets with high magnification are more difficult to analyze as they lack sufficient reference stars to perform relative astrometric alignment. This is in tension with the need to have high photometric precision in order to precisely measure the microlensing parallax. Although bright and highly magnified stars should still be followed up if they are long duration events, special care must be taken when designing observations to ensure good astrometric alignment.

6.5. BH searches with the Roman Space Telescope

Although the initial idea and subsequent design requirements for the Roman Space Telescope (hereafter *Roman*) microlensing survey are driven by exoplanet searches (Penny et al. 2019), it also hails the next generation of astrometric microlensing campaigns searching for BHs. Presently, each event must be followed up individually, with only two facilities (HST and Keck) capable of the precision in the near-infrared required to make such a measurement. Such measurements are expensive (requiring an \sim orbit of Hubble or \sim hour of Keck time per measurement), prohibiting dense astrometric temporal sampling or a large sample of targets.

Roman will change this with its ability to simultaneously obtain precise photometry and astrometry over a wide field of view $100\times$ the area of HST and astrometric precision almost an order of magnitude better than HST (Spergel et al. 2015; WFIRST Astrometry Working Group et al. 2019). This will also allow the masses of NS-BH mass gap objects to be precisely measured, and allow a sample of 100-1000 BH candidates to be built up over the duration of the survey (Lam et al. 2020). In

addition, *Roman* will probe a large sample of shorter t_E events which will place constraints on BH kicks.

To make *Roman* as effective as possible for finding BHs, there are several considerations that need to be addressed. The main issue is the large temporal gaps. These are generally not a concern for exoplanets searches, as the transient portion of the lightcurve is nearly covered within the 72 day window. However, for long duration events where the transient portion of the lightcurve is much longer than the window and where a measurement of small microlensing parallax is crucial, incomplete lightcurve coverage will mean the difference between a confirmed BH mass measurement and only an upper limit. Observations filling in these gap will be crucial. Collaboration with a ground-based telescope to provide imaging during the gaps, or a smaller independent follow-up mission with cubesats would be very important.

7. CONCLUSION

We analyze five microlensing events with candidate BH lenses. Combining HST astrometry and densely sampled ground-based photometry, we derive masses for these five lenses as well as their probability of being a BH. Of the five targets, we make one definitive > 1 mas detection of astrometric microlensing (OB110462). The mass of the lens in OB110462 is in the range $1.6\text{--}4.2 M_\odot$, making it the first detection of a compact object through astrometric microlensing.

We use this sample to observationally constrain the number of BHs in the Milky Way. Our observational BH yield currently agrees with simulations assuming 2×10^8 BHs in the Milky Way, albeit with very large uncertainties due to the small sample size. The ability to place more stringent constraints on the number and mass distribution of Galactic BHs will require larger samples, such as *Roman*'s microlensing survey.

Astrometric microlensing holds the key to uncovering the hidden BH population. Further pursuit and refinement of the event selection, observing, and modeling process will fulfill the full promise of this technique and its ability to reveal the properties of Galactic BHs.

ACKNOWLEDGEMENTS

We thank Dan Foreman-Mackey, Tharindu Jayasinghe, Tom Loredo, and Greg Martinez for helpful and interesting conversations. We also thank Kailash Sahu, Howard Bond, Jay Anderson, Martin Dominik, Philip Yock, and Annalisa Calamida for proposing and taking the archival HST observations used in this work.

C.Y.L. and J.R.L. acknowledge support by the National Science Foundation under Grant No. 1909641

and the National Aeronautics and Space Administration (NASA) under contract No. NNG16PJ26C issued through the WFIRST (now Roman) Science Investigation Teams Program. C.Y.L. also acknowledges support from NASA FINESST grant No. 80NSSC21K2043. D.P.B. was supported by NASA grants NASA-80NSSC18K0274 and 80GSFC17M0002.

Based on observations made with the NASA/ESA Hubble Space Telescope, obtained from the data archive at the Space Telescope Science Institute (STScI) operated by the Association of Universities for Research in Astronomy, Inc. under NASA contract NAS 5-26555, and obtained from the the Hubble Legacy Archive, a collaboration between STScI/NASA, the Space Telescope European Coordinating Facility (ST-ECF/ESA) and the Canadian Astronomy Data Centre (CADC/NRC/CSA).

This paper makes use of data obtained by the MOA collaboration with the 1.8 metre MOA-II telescope at the University of Canterbury Mount John Observatory, Lake Tekapo, New Zealand. The MOA collaboration is supported by JSPS KAKENHI (Grant

Number JSPS24253004, JSPS26247023, JSPS23340064, JSPS15H00781, JP16H06287, and JP17H02871) and the Royal Society of New Zealand Marsden Fund.

This work presents results from the European Space Agency (ESA) space mission Gaia. Gaia data are being processed by the Gaia Data Processing and Analysis Consortium (DPAC). Funding for the DPAC is provided by national institutions, in particular the institutions participating in the Gaia MultiLateral Agreement (MLA).

This research has made use of data obtained from the Chandra Source Catalog, provided by the Chandra X-ray Center (CXC) as part of the Chandra Data Archive.

Software: Galaxia (Sharma et al. 2011), astropy (Astropy Collaboration et al. 2013, 2018), Matplotlib (Hunter 2007), NumPy (van der Walt et al. 2011), SciPy (Virtanen et al. 2019), SPISEA (Hosek et al. 2020), PopSyCLE (Lam et al. 2020), dynesty (Speagle 2020), PyMultiNest (Buchner et al. 2014; Feroz et al. 2009), dustmaps (Green 2018), hst1pass (Anderson & King 2006)

APPENDIX

A. RESCALING OF UNCERTAINTIES

For each epoch, `hst1pass` returns the standard deviation of positions and magnitudes over multiple frames σ_x , σ_y and σ_m , respectively. For our uncertainties, we use the error on the mean σ/\sqrt{N} , where N is the number of frames the star is detected in. An empirical constant additive error on the positions Δ_{xy} and magnitudes Δ_m is calculated for each epoch and added in quadrature to the error on the means. This produces the final inflated uncertainties used in the analysis

$$\sigma'_x = \sqrt{\sigma_x^2/N + \Delta_{xy}^2} \quad (\text{A1})$$

$$\sigma'_y = \sqrt{\sigma_y^2/N + \Delta_{xy}^2} \quad (\text{A2})$$

$$\sigma'_m = \sqrt{\sigma_m^2/N + \Delta_m^2}. \quad (\text{A3})$$

To determine Δ_{xy} and Δ_m , a sample of bright, unsaturated stars are selected. The exact magnitude range constituting “bright” is roughly saturation to 3-5 magnitudes fainter, with the exact range determined empirically through the astrometric alignment process. In this sample, the additive error is selected such that the χ^2 distribution of the reference stars position and magnitude fits is roughly consistent with the expected distribution (Figure 9). The resulting values are listed in Table 18. Note that for MB09260 F606W, a constant value across all epochs was simply used.

B. INJECTION AND RECOVERY TESTS

We use the `ks2` software (Anderson et al. (2008); Bellini et al. (2018), see also §3 of Sabbi et al. (2016) for a detailed description) to inject artificial stars into the OB110462 HST images to determine how well we can recover the magnitudes and positions of faint sources near bright sources. Injection and recovery tests are performed for all OB110462 epochs in two different manners:

1. Sources are injected radially around the bright neighbor star at the radius as OB110462, at a variety of azimuths, excluding the azimuth of OB110462 itself (since we cannot recover a source planted on top of a real star).
2. Sources are injected near a comparison star of similar brightness to the neighbor, in the same configuration relative to the comparison star as OB110462 to its bright neighbor (distance and azimuth).

The first test directly probes the region around the neighbor itself but excludes the actual position of the OB110462, while the second test probes a comparison star similar to the neighbor, at the same separation and angle of OB110462 relative to the neighbor.

Table 18. Additive errors for HST data

Epoch	Pos. error (mas)		Mag. error (mmag)	
(yyyy-mm-dd)	F814W	F606W	F814W	F606W
MB09260				
2009-10-19	0.12	—	3.2	—
2010-03-22	0.14	—	4.9	—
2010-06-14	0.14	—	6.1	—
2010-10-20	0.13	—	9.2	—
2011-04-19	0.14	0.36	12.8	4.0
2011-10-24	0.15	0.23	4.0	4.0
2012-09-25	0.15	0.27	4.3	4.0
2013-06-17	0.16	0.28	9.8	4.0
MB10364				
2010-09-13	0.14	1.61	8.6	11.6
2010-10-26	0.14	0.49	4.5	8.6
2011-10-31	0.17	0.26	5.9	5.0
2012-09-25	0.18	0.26	8.5	6.1
2013-10-24	0.17	0.25	6.8	5.8
OB110037				
2011-09-26	0.11	0.18	4.1	14.0
2011-11-01	0.10	0.21	4.0	3.8
2012-05-07	0.10	0.26	12.9	12.2
2012-09-25	0.10	0.22	6.7	4.3
2013-10-21	0.10	0.23	3.9	4.9
2014-10-26	0.10	0.21	4.2	9.7
2017-03-13	0.10	0.21	4.9	5.1
2017-09-04	0.11	0.21	8.5	19.6
OB110310				
2011-10-31	0.12	0.30	4.2	4.9
2012-04-24	0.13	0.30	10.0	24.3
2012-09-24	0.14	0.29	10.2	10.9
2013-10-21	0.13	0.29	4.3	6.3
2017-03-14	0.13	0.31	4.1	18.8
2017-09-01	0.14	0.32	10.0	24.9
OB110462				
2011-08-08	0.13	0.41	18.1	17.0
2011-10-31	0.19	0.37	3.9	5.4
2012-09-09	0.19	0.36	4.7	7.2
2012-09-25	0.19	0.36	6.8	7.2
2013-10-22	0.19	0.36	3.6	4.8
2014-10-26	0.19	0.39	3.8	10.7
2017-08-29	0.20	0.40	5.4	14.7
2021-10-01	0.17	0.36	7.5	12.9

The star we dub “the neighbor” is ~ 10 pixels (~ 0.4 arcsec) west of OB110462. The star we dub “the comparison star” in F814W is ~ 75 pixels (~ 3 arcsec) northeast of OB110462; for F606W the comparison star is ~ 40 pixels (~ 1.6 arcsec) north of OB110462 (Figure 23).

In summary, both methods produce similar results (Figures 24 and 25). We use the results from injection around the comparison star (single-azimuth results) in order to capture any azimuthal dependence which would be lost by averaging over multiple azimuths. This is presented in Table 19.

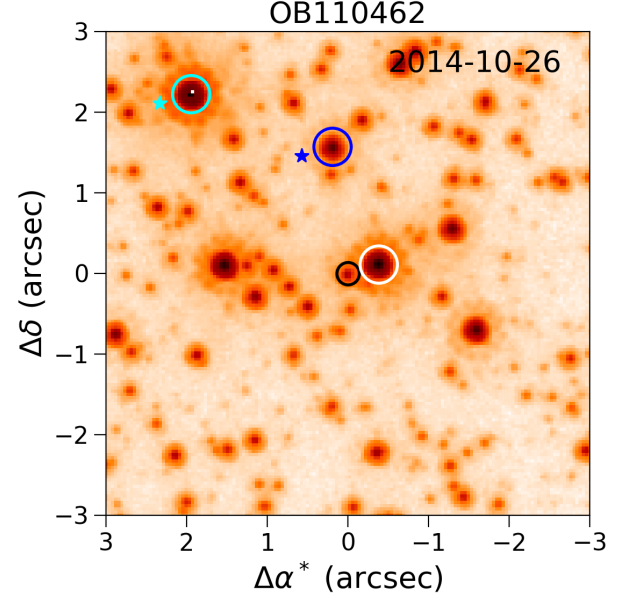


Figure 23. Injection and recovery for OB110462. *Black circle, center:* OB110462. *White circle:* the bright neighbor. *Blue circle:* comparison star for F606W. *Cyan circle:* comparison star for F814W. Positions where stars are injected in reference to the comparison star are shown as blue and cyan stars (F606W and F814W, respectively).

In F814W, the bias is negligible in the first epoch, when the target is magnified and is of similar brightness to the neighbor. However, in later epochs once the target is no longer magnified, the bright star biases the position of the target, by causing the target to be too close to the target by ~ 0.4 mas along the target-neighbor separation vector. The magnitude and direction of the positional offset are comparable across the two approaches, except in 2014, where the injection around the bright star leads to a larger difference than when injecting around the neighbor. The uncertainties are larger in the approach of planting around the neighbor, as it averages over more azimuths and results in a larger uncertainty.

In F606W, the bias is smaller than F814W because the shorter wavelength results in higher resolution. Like F814W, the bias is also negligible in the first epoch, and around ~ 0.25 mas in later epochs. The uncertainties are also larger when averaging across many azimuths. Unlike F814W, the bias is mixed between radial and azimuthal when considering a single azimuth.

B.1. Injection around the neighbor

For each epoch, we determine the separation r of OB110462 and the bright neighbor. We inject three rings of stars surrounding the bright neighbor, of radii

Table 19. Bias correction derived from injection and recovery

Epoch	ΔRA (mas)	ΔDec (mas)	ΔMag (mag)
F606W			
2011-08-08	-0.025 ± 0.001	0.012 ± 0.001	-0.001 ± 0.000
2011-10-31	-0.068 ± 0.002	0.168 ± 0.002	-0.001 ± 0.000
2012-09-09	-0.216 ± 0.001	-0.185 ± 0.001	-0.005 ± 0.000
2012-09-25	0.108 ± 0.002	0.136 ± 0.001	-0.003 ± 0.000
2013-10-22	-0.431 ± 0.001	0.070 ± 0.001	-0.007 ± 0.000
2014-10-26	-0.033 ± 0.001	0.298 ± 0.001	-0.004 ± 0.000
2017-08-29	-0.144 ± 0.001	0.032 ± 0.001	-0.011 ± 0.000
2021-10-01	0.124 ± 0.002	-0.014 ± 0.001	-0.007 ± 0.000
F814W			
2011-08-08	-0.049 ± 0.000	-0.014 ± 0.000	-0.001 ± 0.000
2011-10-31	-0.203 ± 0.001	-0.070 ± 0.001	-0.004 ± 0.000
2012-09-09	-0.278 ± 0.001	-0.150 ± 0.001	-0.016 ± 0.000
2012-09-25	-0.292 ± 0.001	0.025 ± 0.002	-0.007 ± 0.000
2013-10-22	-0.490 ± 0.001	-0.081 ± 0.001	-0.011 ± 0.000
2014-10-26	-0.665 ± 0.001	-0.138 ± 0.001	-0.013 ± 0.000
2017-08-29	-0.258 ± 0.001	-0.129 ± 0.001	-0.013 ± 0.000
2021-10-01	-0.315 ± 0.000	-0.001 ± 0.001	-0.007 ± 0.000

NOTE— Bias correction derived from injection/recovery around a star of comparable brightness at the same separation, azimuth, and magnitude difference as the target to its bright neighbor.

$r - 0.2$ pixels, r , and $r + 0.2$ pixels. Each ring consists of 24 evenly spaced stars, resulting in one star every 15 degrees. Because we cannot recover stars injected on top of the target itself, we do not attempt to recover injected stars that fall within 4 pixels of the target itself; this excludes three of the positions. We thus inject a total of $(24 - 3) \times 3 = 63$ stars per epoch.

B.2. Injection around neighbor-like star

The neighbor-like star we inject around is different for F814W and F606W, because the surrounding stars do not have the same colors as the neighbor and target. The neighbor-like stars were chosen to have similar magnitude and saturation level to the neighbor. In F814W, the neighbor tended to be saturated; the F814W neighbor-like star is also saturated. On the other hand, in F606W the neighbor was not saturated, and the F606W neighbor-like star is also not saturated. The F814W neighbor-like star is brighter than the neighbor in F814W by ~ 0.6 mag, and the F606W neighbor-like star is fainter than the neighbor in F606W by ~ 0.5 mag.

In each epoch, we inject three arcs of radii $r - 0.2$ pixels, r , and $r + 0.2$ pixels centered on the neighbor-like star, where r is the target-neighbor separation (~ 10 pixels). Each arc consists of 15 stars at the azimuth of the target relative to the neighbor ± 0.2 pixels/(target - neighbor separation in pixels), which corresponds to ap-

proximately ± 1.1 degrees. This corresponds to a region of $\sim 0.04 \text{ pix}^2$ where $3 \times 3 \times 15 = 135$ stars are injected.

At each position we inject stars of magnitude $m_I - 0.1$, m_I , and $m_I + 0.1$, where m_I is the magnitude that results in the same contrast with the neighbor-like star as OB110462 to the neighbor. That is, if OB110462 has magnitude m_T and the neighbor m_N , and the injected star is m_I around the neighbor-like star m_C , then $m_T - m_N = m_I - m_C$.

B.3. Recovery of injected sources

After planting fake stars into the image, we determine how well we can recover the positions and magnitudes. To match the properties of our original dataset, we consider stars to be recovered if they are detected in at least N frames, where N is the number of frames were used to calculate the position of the source. Iterative 3-sigma clipping is performed to exclude outliers due to confusion, e.g. from the diffraction spike mask. We then use the transformation parameters derived for this epoch (as described in Section 3.2.1) to convert from (x,y) pixel positions to (RA, Dec) coordinates.

We define a polar coordinate system with the origin located at the neighbor/neighbor-like star. The azimuthal direction is measured counterclockwise from the origin-OB110462 separation vector. The average offset in the radial and azimuthal directions are $\bar{\Delta}r$ and $\bar{\Delta}\theta$ (Figures 24 and 25).

The color of the neighbor and OB110462 are very similar. At baseline, the neighbor is about 3.1 magnitudes brighter than OB110462. During magnification in the first epoch (2011-08-08), the neighbor is only about 0.4 magnitudes brighter. Since the resolution is higher at shorter wavelengths, it is not unexpected that the positional bias is less in F606W than F814W, since the separation is the same in both filters. It is also not surprising that the bias is smallest in the first epoch when the magnitude difference between OB110462 and the neighbor is small, and larger in the remaining epochs when the magnitude difference is large.

C. ABSOLUTE PROPER MOTION REFERENCE FRAME

For each $r = 60''$ field around the target, we match stars from the Gaia EDR3 catalog that report proper motions (i.e. 5-parameter and 6-parameter solutions) and `astrometric_excess_noise_sig` < 2 to the stars in our HST proper motion catalog. For the matched stars, the 1-iteration 3σ -clipped uncertainty-weighted average difference in the proper motion between the two catalogs is calculated. This proper motion offset is added back onto the HST catalog in order to obtain absolute proper

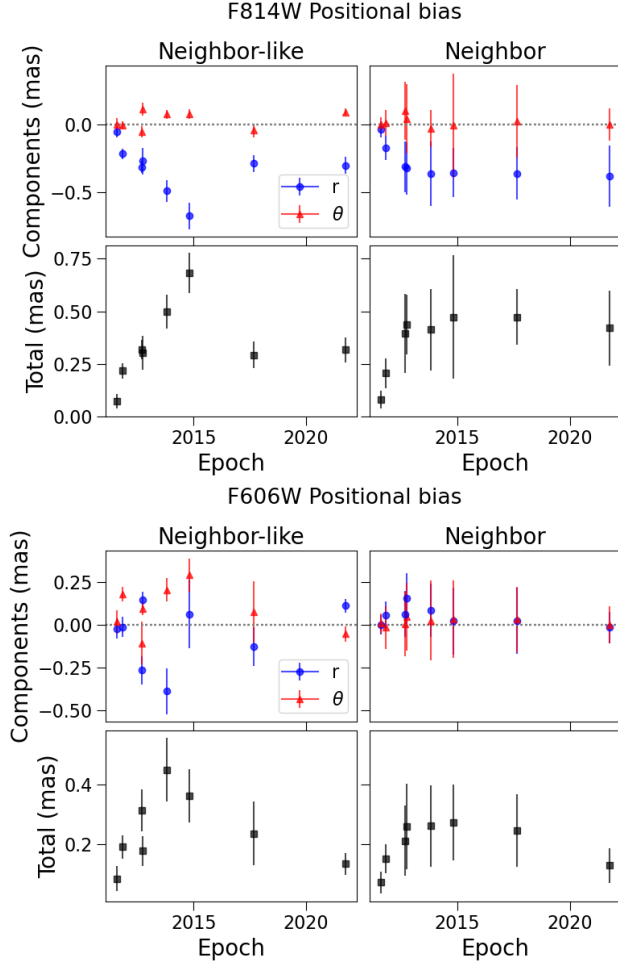


Figure 24. Positional bias in F814W (*top panel*) and F606W (*bottom panel*) as calculated from injection and recovery tests, injecting around a neighbor-like star (*left column*) or around the neighbor (*right column*). The positional bias (position recovered minus the true position input) is shown as a function of radial r and azimuthal θ components (*top row*), as well as total positional bias (*bottom row*).

motions in the Gaia proper motion frame. The values are listed in Table 20.

The vector point diagram of proper motion differences between cross-matched sources in the Gaia and HST F814W catalogs is shown in Figure 26. The discrepancy is worse for fainter stars. This could indicate that the Gaia or HST proper motion uncertainties are underestimated or that there are higher-order distortions between the two reference frames. However, the most likely explanation is just that the Gaia proper motions are not accurate or have underestimated uncertainties (see Appendix F).

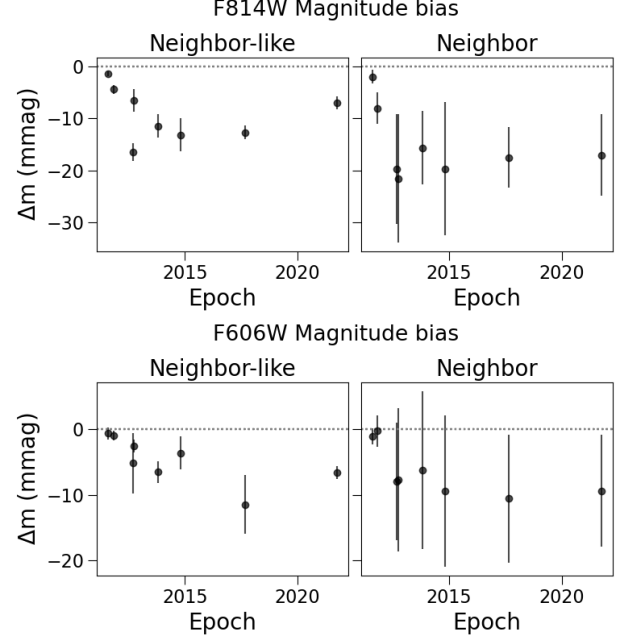


Figure 25. Magnitude bias in F814W (*top panel*) and F606W (*bottom panel*) as calculated from injection and recovery tests, injecting around a neighbor-like star (*left column*) or around the neighbor (*right column*). The magnitude bias is defined as the magnitude recovered minus the true magnitude input.

Table 20. HST to Gaia Proper Motion Reference Frame Offset

Target	$\langle \Delta \mu_{\alpha*} \rangle$ (mas/yr)	$\langle \Delta \mu_{\delta} \rangle$ (mas/yr)
MB09260	-2.56 ± 0.13	-4.25 ± 0.10
MB10364	-2.70 ± 0.10	-4.56 ± 0.10
OB110037	-2.31 ± 0.23	-4.48 ± 0.20
OB110310	-2.20 ± 0.12	-4.73 ± 0.08
OB110462	-2.34 ± 0.15	-4.72 ± 0.11

NOTE— $\Delta \mu_{\alpha*} = \mu_{\text{Gaia}, \alpha*} - \mu_{\text{HST F814W}, \alpha*}$ and $\Delta \mu_{\delta} = \mu_{\text{Gaia}, \delta} - \mu_{\text{HST F814W}, \delta}$.

D. ASTROMETRIC LENSING IN GAIA

There appear to be some discrepancies comparing the inferred proper motions of the targets in Gaia and HST (Table 6). As discussed in §3.2.6, there are several differences between the way we model proper motions as compared to Gaia. First, we are simultaneously modeling the proper motions of the lens and source with parallax, within a microlensing model. In contrast, Gaia is modeling a single star with parallax. Second, the time baselines over which the proper motions are calculated are different. The HST time baseline for MB10364 is 2010-2013, and OB110037 and OB110310 is 2011-2017,

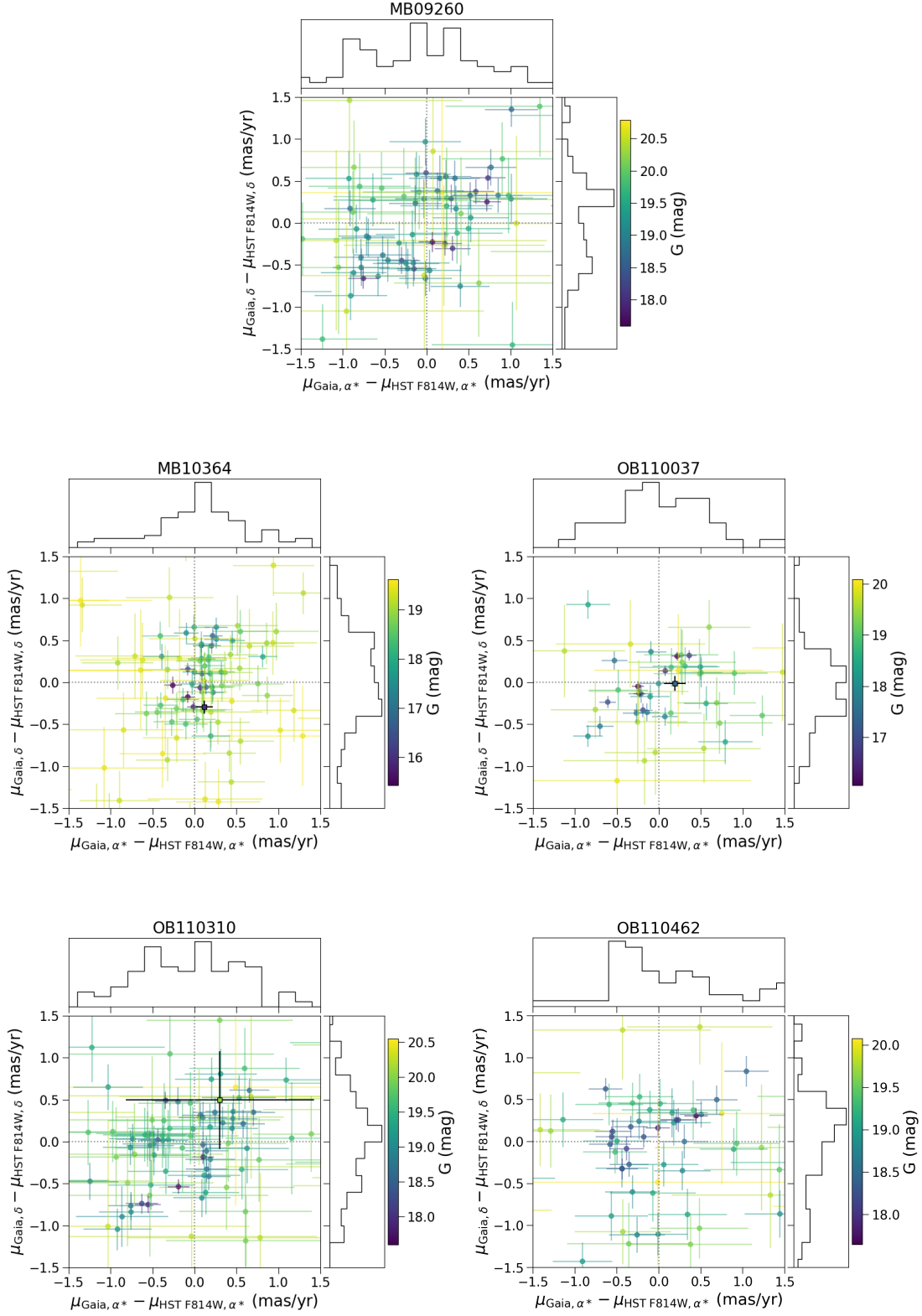


Figure 26. Vector point diagram of proper motion differences between cross-matched sources in the Gaia and HST F814W catalogs within 60'' of the targets. The color of the point indicates the star's magnitude in Gaia G-band. For MB10364, OB110037, and OB110310 the target is shown in the black-outlined square.

while Gaia is 2014-2017. As the lensing signal is time dependent, these two differences might lead us to measure different proper motions than Gaia. Third, the source and lens are not resolvable from each other in Gaia nor HST during the observations, so Gaia is measuring the proper motion of both the source and the lens, while in our fit these proper motions are treated separately. Depending on the relative source-lens motion and color, this could also produce different results.

With regard to the second point, we can estimate the amount by which astrometric microlensing could change the proper motion measurement. Long after source-lens closest approach, i.e. $(t - t_0)/t_E \gg 1$, the impact parameter can be approximated

$$u(t) \approx \frac{t - t_0}{t_E} \gg 1. \quad (\text{D4})$$

The astrometric shift for $u(t) \gg 1$ due to lensing can be approximated as

$$\delta_c(u, \theta_E) \approx \frac{\theta_E}{u}. \quad (\text{D5})$$

We can thus approximate the change in proper motion over time Δt due to astrometric lensing long after the microlensing event as

$$\Delta_{PM} \approx \frac{\theta_E}{\Delta t} \left[\frac{1}{u(t)} - \frac{1}{u(t + \Delta t)} \right]. \quad (\text{D6})$$

For MB10364, OB110037, and OB110310, for Δt corresponding to the start and end of Gaia EDR3 observations, $\Delta_{PM} \approx 0.003, 0.02$, and 0.01 mas/yr, respectively. Hence the effect of lensing on proper motions should be negligible in Gaia. Thus, if the lens is dark, and ignoring crowding/resolution differences between HST and Gaia, the proper motions of the source and the proper motion reported of the target by Gaia should be directly comparable.

E. CONSTRAINTS ON LUMINOUS STELLAR LENSES

We follow a procedure similar to Wyrzykowski et al. (2016) in order to calculate the probability of a dark lens. The two main differences between the analysis of Wyrzykowski et al. (2016) and ours is that they work with photometric data only and must invoke a Galactic model to obtain lens masses and distances, while in our case astrometric data allows us to fit lens mass and distances. This greatly simplifies the analysis as we do not need to calculate the Jacobian to transform the PDFs between different variables. In addition, we use realistic stellar and Galactic models to determine the lens luminosities, instead of relying on simple mass-luminosity scaling relations.

From the fits, we have posterior distributions for the lens mass M_L , distance d_L , baseline magnitude m_{base} , and source flux fraction b_{SFF} . In the following analysis we reassign any fit values with $b_{SFF} \geq 1$ to instead be equal to 0.999999. This is because values of $b_{SFF} \geq 1$ would result in an infinite lens magnitude (Equation E7).²¹

We draw a random sample of 1000 stars from our posterior. For each star we calculate 1) the brightest lens allowed by b_{SFF} and m_{base} , and 2) the brightest star allowed by M_L and D_L .

To calculate 1), by assuming there are no contaminating neighbor stars, $b_{SFF} = F_S/(F_S + F_L)$, an upper limit can be placed on the brightness of the lens:

$$m_L = m_{\text{base}} - 2.5 \log_{10}(1 - b_{SFF}). \quad (\text{E7})$$

We denote this $m_L(b_{SFF}, m_{\text{base}})$.

To calculate 2), we use the simple stellar population synthesis code SPISEA (Hosek et al. 2020) to generate a suite of star clusters to simulate the possible lens population. We use the MISTv1.2 solar metallicity isochrones (Choi et al. 2016), `get_merged_atmosphere` atmosphere model²², Damini et al. (2016) reddening law, and Kroupa (2001) initial mass function (IMF) over the mass range $0.1 M_\odot < M < 120 M_\odot$. Each cluster is $10^4 M_\odot$, in order to reduce stochastic effects in the sampling of the IMF.

Star clusters are generated at the distances spanned by each target's lens distance posteriors, sampled every 0.25 kpc. Clusters of ages 7.0 to 10.0 \log_{10} years in increments of 0.5 \log_{10} years are simulated at each sampled distance in order to cover the age range of disk and bulge stars. The stellar age distribution as a function of distance is drawn from the Galaxia Milky Way stellar simulation (Sharma et al. 2011), which implements a version of the Besançon Galactic model of Robin et al. (2003). As our target sight lines are toward the bulge, most of the stars are old, with $\gtrsim 85\%$ of stars being at least 9.0 \log_{10} years old, although younger stars tend to be at closer distances as disk stars dominate. To calculate the simulated stars' apparent magnitudes, we use

²¹ One might worry this could bias the results. However, a visual check comparing the posteriors (both individual and joint) for lens mass and distance don't show a change when excluding fits with $b_{SFF} > 1$. In particular, the lens mass and distances are nearly independent of the lens magnitude. In addition, if the true value of b_{SFF} is 1, we would expect some scatter around that value, including unphysical > 1 values.

²² This is a combination of the ATLAS9 (Castelli & Kurucz 2004), PHOENIX v16 (Husser et al. 2013), BTSettl (Baraffe et al. 2015), and Koester10 (Koester 2010) models. For further details see Appendix B of (Hosek et al. 2020).

the 3-D extinction map of [Marshall et al. \(2006\)](#), accessed via the `dustmaps` software package ([Green 2018](#)), to obtain an A_{K_s} value for each distance.

For each sample from the posterior, we sample one of the star clusters at the corresponding distance at a particular stellar age from the Galactic distribution. All stars in the simulated cluster with masses within 10% of the sampled posterior mass are identified, and the brightest apparent magnitude of the star in this group is denoted $m_L(M_L, D_L, \star)$. If no stars are found within 10% of the sampled posterior mass, this indicates that stars of that mass have all died and formed compact objects.

If $m_L(M_L, D_L, \star) < m_L(b_{SFF}, m_{base})$, a star with the inferred stellar mass from stellar evolution models would be too bright to be hidden in the blended light allowed by the fit. This means that the lens is not a star. We take this to mean the lens is a compact object, and hence a dark lens. Thus the lower limit on the probability of a dark lens in the observed filter is the fraction of samples where $m_L(M_L, D_L, \star) < m_L(b_{SFF}, m_{base})$ or no mass match is found.

Objects with $m_L(M_L, D_L, \star) > m_L(b_{SFF}, m_{base})$ are samples where a luminous stellar lens is consistent with the inferred amount of blending. Note that $m_L(b_{SFF}, m_{base})$ is an upper limit on the brightness of the lens, as we assumed all the blended flux in Equation E7 is due to the lens; it could be due to unresolved unrelated neighbor stars. Thus the upper limit on the probability of a stellar lens in the observed filter is thus the fraction of samples where $m_L(M_L, D_L, \star) > m_L(b_{SFF}, m_{base})$.

For dark lenses (i.e. any objects where $m_L(M_L, D_L, \star) < m_L(b_{SFF}, m_{base})$ or no star of the same mass was found in the simulated cluster), we categorize them as brown dwarfs, white dwarfs, neutron stars, or BHs by simplistically sorting them by their masses:

- Brown dwarfs: $M < 0.2M_\odot$
- White dwarfs: $0.2M_\odot < M < 1.2M_\odot$
- Neutron stars: $1.2M_\odot < M < 2.2M_\odot$
- BHs: $M > 2.2M_\odot$.

In reality there is overlap between white dwarf and neutron star masses, and the overlap between neutron star and BH masses (if they overlap at all) is unknown. In addition, the maximum brown dwarf mass set by stellar physics is $0.08M_\odot$, but we extend this up to $0.2M_\odot$ to have continuity between the lowest mass WDs of around $0.2M_\odot$. Hence these values are only approximate.

Table 21. Distribution of Gaia parameters towards fields of interest

Parameter	MB09260	MB10364	OB110037	OB110310
N_{stars}	611	1157	1056	884
$f_{D>2}$	0.44	0.51	0.59	0.55
$f_{\epsilon=0}$	0.81	0.77	0.85	0.86
$f_{\text{multi}=0}$	0.79	0.41	0.53	0.70
$\text{med}(\text{multi}_{>0})$	4.50	14.00	9.00	5.00
$\text{multi}_{>0[95\%]}$	37.55	54.00	42.30	43.00
$f_{\text{odd}=0}$	0.76	0.61	0.64	0.64
$\text{med}(\text{odd}_{>0})$	25.50	30.00	26.00	27.50
$\text{odd}_{>0[95\%]}$	83.55	78.20	80.00	78.70
$\langle \log_{10}(\text{amp}) \rangle$	-1.24	-0.89	-1.03	-1.13
$\sigma_{\log_{10}(\text{amp})}$	0.45	0.39	0.58	0.44
$\langle \log_{10}(\text{ruwe}) \rangle$	0.04	0.12	0.08	0.06
$\sigma_{\log_{10}(\text{ruwe})}$	0.10	0.16	0.11	0.11
$\langle \log_{10}(C) \rangle$	0.23	0.22	0.25	0.26
$\sigma_{\log_{10}(C)}$	0.12	0.16	0.15	0.15

NOTE— N_{stars} : Number of Gaia sources within 1 deg^2 of the target.
 $f_{D>2}$: Fraction of sources with `astrometric_excess_noise_significance` > 2.
 $f_{\epsilon=0}$: Fraction of sources with `astrometric_excess_noise` > 2.
 $f_{\text{multi}=0}$: Fraction of stars with `ipd_frac_multi_peak` = 0.
 $\text{med}(\text{multi}_{>0})$: Median of nonzero `ipd_frac_multi_peak` values.
 $\text{multi}_{>0[95\%]}$: 95th quantile of nonzero `ipd_frac_multi_peak` values.
 $f_{\text{odd}=0}$: Fraction of stars with `ipd_frac_odd_win` = 0.
 $\text{med}(\text{odd}_{>0})$: Median of nonzero `ipd_frac_odd_win` values.
 $\text{odd}_{>0[95\%]}$: 95th quantile of nonzero `ipd_frac_odd_win` values.
 $\langle \log_{10}(\text{amp}) \rangle$: Mean of $\log_{10}(\text{ipd_gof_harmonic_amplitude})$.
 $\sigma_{\log_{10}(\text{amp})}$: Standard deviation of $\log_{10}(\text{ipd_gof_harmonic_amplitude})$.
 $\langle \log_{10}(\text{ruwe}) \rangle$: Mean of $\log_{10}(\text{ruwe})$.
 $\sigma_{\log_{10}(\text{ruwe})}$: Standard deviation of $\log_{10}(\text{ruwe})$.
 $\langle \log_{10}(C) \rangle$: Mean of $\log_{10}(\text{phot_bp_rp_excess_factor})$.
 $\sigma_{\log_{10}(C)}$: Standard deviation of $\log_{10}(\text{phot_bp_rp_excess_factor})$.

The above analysis is performed for both the HST F606W and F814W filters. The reported probabilities are the joint constraint. A lens is dark if no masses consistent with a stellar lens are found in either filter. A lens is also dark if the maximum inferred lens flux is insufficient to hide a star (i.e. $m_L(M_L, D_L, \star) < m_L(b_{SFF}, m_{base})$) in either filter. A lens is luminous if the maximum inferred lens flux is sufficient to hide a star (i.e. $m_L(M_L, D_L, \star) > m_L(b_{SFF}, m_{base})$) in both filters. We do not perform this analysis for the OGLE or MOA photometry parameters as the high resolution HST images show the seeing-limited apertures have unrelated neighbor stars in the blend, and hence the limits will all be weaker than using HST. Figure 27 shows the distribution of dark vs. luminous lens probability as a function of mass for each target. Table 9 lists the upper limit on the probability of a stellar lens and lower limits on the probabilities of different dark lenses for each target.

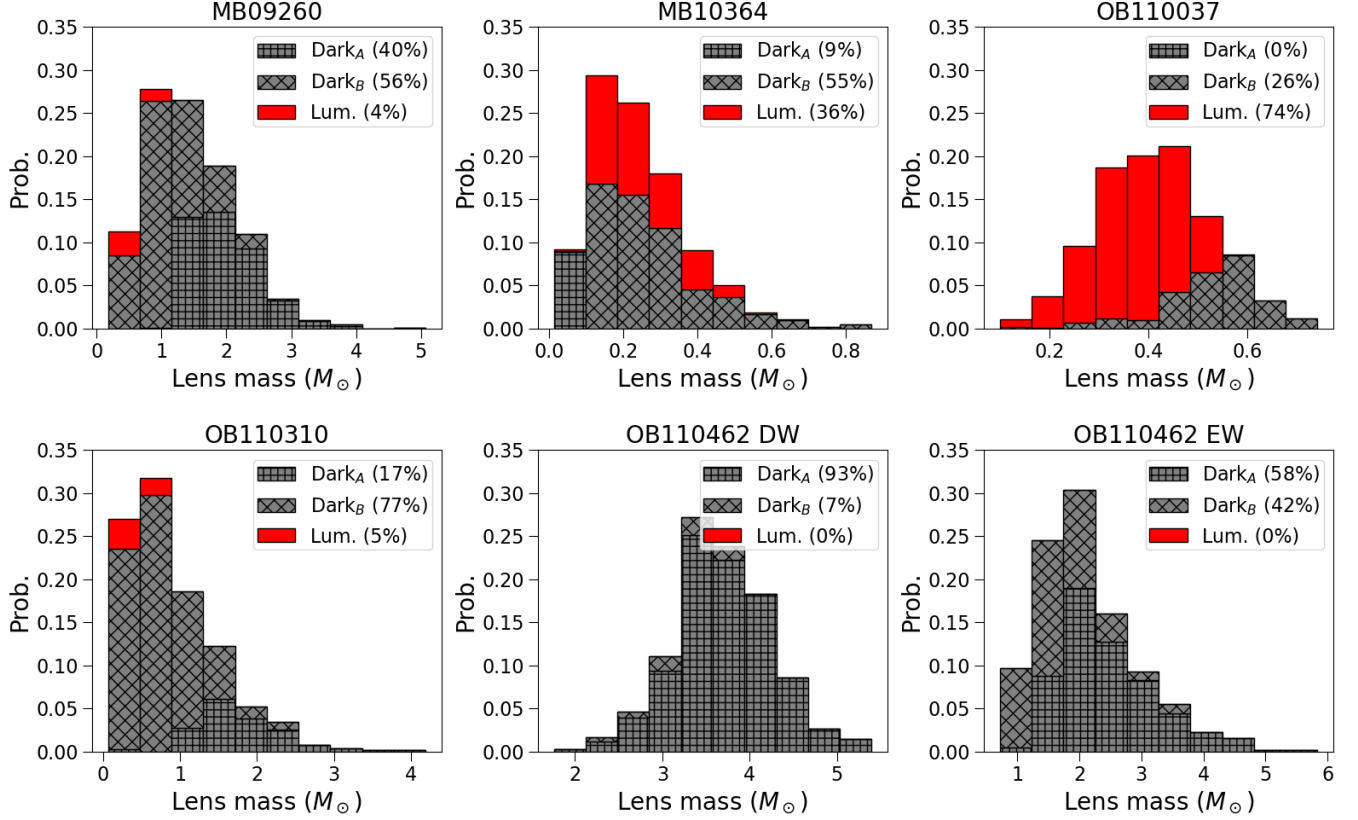


Figure 27. Probabilities for dark (gray) and luminous lenses (red), as a function of lens mass for each target. Lenses that are dark because all stars of that mass have already evolved and died (implying they are compact objects) are subscripted with *A* (square hatch), while lenses that are dark because a star would be too bright to be hidden in the allowed lens flux are subscripted with *B* (diamond hatch). The probabilities for the luminous lenses are upper limits, while the probabilities for the dark lenses are lower limits, since the method described in Appendix E only places an upper limit on the brightness of the lens. Note that there are two fits for OB110462, one with equal weighting to the astrometry and photometry data (OB110462 EW) and one with the default weighting of the astrometry and photometry data (OB110462 DW). See §4.3 for details.

F. GAIA DIAGNOSTICS

We would ideally like to incorporate information from Gaia EDR3 into our target analysis (e.g. using the reported parallaxes and proper motions to inform the prior on the source parallax in the fit, or to compare to the posteriors as a cross-check to validate the results). However, it is known that there are many as-of-yet-unresolved systematics in the Gaia EDR3 astrometry, especially toward the Bulge, and extra care must be taken to verify if a proper motion or parallax for a particular Gaia source is reliable. Gaia EDR3 is much better than Gaia DR2 in terms of photometry, but the astrometry still has issues that need to be worked out (Fabricius et al. 2021). We investigate several different metrics for the Gaia solutions for our targets to determine the reliability of the reported parallax and proper motions. A brief summary of the meaning of relevant Gaia statistics is presented in Table 2; we refer the reader to the Gaia

Early Data Release 3 documentation (van Leeuwen et al. 2021) for details.

F.1. Solution type

Sources in Gaia have varying amounts of information available, described by `astrometric_params_solved`: 3 (2-parameter solution: position), 31 (5-parameter solution: position, parallax, proper motion) or 95 (6-parameter solution: position, parallax, proper motion, astrometrically estimated effective wavenumber). 5-parameter is generally the most accurate, followed by 6-parameter, then 2-parameter. 6-parameter is worse than 5-parameter because it means an assumption had to be made about the source color, which also usually means there is some problem with the source, e.g. very crowded regions, which further reduces accuracy. MB09260 has a 2-parameter solution, MB10364 and OB110310 have 6-parameter solutions, and only OB110037 has a 5-parameter solution. Based on the high-resolution HST images (Figure 1) this is not too surprising, as OB110037

is the brightest object in its area, while the other targets have comparably bright stars nearby.

F.2. Image parameter determination parameters

The Gaia EDR3 solution assumes the motions of objects are due to single stars. Hence, different types of binaries can be identified through large image parameter determination (IPD) parameters: `ipd_gof_harmonic_amplitude` (partially resolved binaries, asymmetric images), `ipd_frac_multi_peak` (resolved, close binaries), `ipd_frac_odd_win` (another bright source, observation window conflicts for wide pairs) (Lindegren et al. 2021b). Given that the targets all have lightcurves well described by point lenses, we do not expect any of these parameters to be unusual for our targets; unusual values likely indicates problems with the astrometric solution itself due to crowding or contamination.

The values for `ipd_gof_harmonic_amplitude` for MB09260, MB10364, OB110037, and OB11030 (0.089, 0.064, 0.036, 0.042, respectively) are somewhat large compared to the median values reported in Tables 4-6 of Lindegren et al. (2021b). However, this is to be expected toward the bulge. Compared to other stars within 1 deg² (Table 21), the values are not unusual.²³

MB10364 has `ipd_frac_multi_peak` = 15. From the HST image MB10364 does not appear to be a resolved binary. The last HST image is from 2014, and Gaia EDR3 observations span 2014-2017, so one could check if the lens and source separation is large enough to resolve with Gaia EDR3; however, this is ruled out by considering the lens-source separation criteria (Table 16) and the fact that Gaia’s resolution is worse than HST’s. The likeliest explanation is that Gaia got confused by the neighboring stars near MB10364 since the crowding within 1 arcsec of MB10364 is high. The other targets have `ipd_frac_multi_peak` = 0.

MB09260 has `ipd_frac_odd_win` = 18 and OB110310 has `ipd_frac_odd_win` = 55. As those targets have neighbors within 1 arcsecond brighter than themselves, those bright neighbors likely confused Gaia. The other targets have `ipd_frac_odd_win` = 0.

F.3. Astrometric goodness-of-fit statistics

Gaia also presents several relevant goodness-of-fit (GOF) statistics from the astrometric fit: the renormalized unit weight error (RUWE; ideally 1), the extra noise required per observa-

tion to explain the residual in the astrometric fit of the source (`astrometric_excess_noise`; ideally 0), and the significance of this source noise (`astrometric_excess_noise_sig`; insignificant if < 2).

MB09260 does not have a RUWE because it is not calculated for 2-parameter solutions. OB110037 and OB110310 both have RUWE ~ 1 (0.971 and 0.981, respectively). MB10364 has a large RUWE (1.388), although not unusual compared to the sources nearby (Table 21)²⁴.

MB09260 and MB10364 both have significant astrometric excess noise (1.241 mas and 0.406 mas, respectively). OB110037 does not have astrometric excess noise and the noise for OB110310 is not significant.

Gaia documentation (van Leeuwen et al. 2021) notes that “For good fits in the limit of a large number of observations, astrometric excess noise significance D should be zero in half of the cases and approximately follow the positive half of a normal distribution with zero mean and unit standard deviation for the other half. Consequently, D is expected to be greater than 2 for only a few percent of the sources with well-behaved astrometric solutions.” It also warns that “Given the many other possible contributions to the excess noise, the user must study the empirical distributions of astrometric excess noise ϵ_i and D to make sensible cutoffs before filtering out sources for their particular application.” Table 21 lists the distributions of D for the stars in Gaia within 1 deg² of our targets. Near MB09260, 84% sources have $D > 0$ and 44% have $D > 2$. Near MB10364, 79% sources have $D > 0$ and 51% with have $D > 2$. Near OB110037, 86% sources have $D > 0$ and 59% have $D > 2$. Near OB110310, 87% sources have $D > 0$ and 54% have $D > 2$. Clearly $D > 2$ for more than a few percent of stars. This is not surprising, as there also still exist many systematics in the astrometry, especially toward the Bulge.

F.4. Color excess

Fabrizius et al. (2021) use $C = \text{phot_bp_rp_excess_factor}$ as a proxy for contamination due to crowding. Stars with large excess ($C > 5$) tend to have underestimated proper motion uncertainties by a factor of ~ 1.7 . All of our targets have $C < 5$; less than 1% of stars within 1 deg² of the targets have $C > 5$. This metric does not seem to capture crowding toward the Bulge.

²³ Note the values reported in Table 21 are the logarithms of `ipd_gof_harmonic_amplitude`, as those are approximately normally distributed.

²⁴ Note the values reported in Table 21 are the logarithms of RUWE, as that are approximately normally distributed.

F.5. Summary

Comparing to the high resolution images we have from HST, the various values reported by Gaia make sense.

- OB110037 is the brightest source in its vicinity, and hence has a good astrometric solution. Its astrometric solution (parallax and proper motion) are likely to be reliable. The HST source proper motion agrees with the Gaia proper motion measurement.
- MB10364 is bright but it also is crowded. OB110310 is somewhat isolated but is faint. Their astrometric solutions are likely to be unreliable.
- MB09260 does not have enough visibility periods to generate an astrometric solution (requires at least 9 visibility periods, while MB09260 only has 8), so it is only a 2-parameter solution.

In conclusion, although Gaia is a dedicated astrometric mission, it is not optimized for the crowded and extincted Bulge, and the astrometric parameters are likely to be untrustworthy there (Fabricius et al. 2021; Rybizki et al. 2021). Although Gaia EDR3 is also an improvement over DR2, those improvements are in the photometry and not the astrometry. Placing too much weight on the Bulge astrometry in analyses (especially the uncertainties) should be done with caution. For these targets, we will likely need to wait until the end of the Gaia mission for per-epoch astrometry to make comparisons. However, when this is possible it will be interesting, as Gaia EDR3 goes from July 2014 to May 2017, which means it starts when MB10364 HST data leaves off, and fills in the gap between the 2014 and 2017 HST data for all the OGLE targets.

G. GAUSSIAN PROCESS

The photometric microlensing survey data contains uncharacterized systematics in the lightcurves, which may be due to unaccounted correlated noise from astrophysical processes or data acquisition and reduction. Correlated noise can bias the results of parameter estimation. Golovich et al. (2020) fit a set of publicly released OGLE-III and OGLE-IV microlensing lightcurves using gaussian processes (GPs) to account for correlated noise; we follow that approach here. We use the *celerite* package (Foreman-Mackey et al. 2017) to implement GPs in our microlensing model.

For a thorough reference about GPs and their application to machine learning and inference, the reader may consult sources such as Rasmussen & Williams (2006). In short, a GP is composed of two parts: the noise (the

stochastic component) and the mean function (the deterministic component). The properties of the stochastic component are governed by the covariance matrix, also known as the kernel, of the GP. The notation

$$y \sim \mathcal{GP}(\mu_{\theta}(t), K_{\alpha}(t, t')) \quad (\text{G8})$$

indicates a GP with mean function μ with parameters θ and kernel K with parameters α .

When trying to infer some set of parameters θ from data

$$\mathbf{y} = (y_1(t_1) \quad \dots \quad y_N(t_N))^T \quad (\text{G9})$$

the Gaussian log-likelihood is

$$\log \mathcal{L}(\mathbf{y}|\theta, \alpha) = -\frac{1}{2} \mathbf{r}_{\theta}^T K_{\alpha}^{-1} \mathbf{r}_{\theta} - \frac{1}{2} \log |K_{\alpha}| - \frac{N}{2} \log(2\pi), \quad (\text{G10})$$

where N is the number of data points, and \mathbf{r}_{θ} is the residual vector

$$\mathbf{r}_{\theta} = (y_1 - \mu_{\theta}(t_1) \quad \dots \quad y_N - \mu_{\theta}(t_N))^T. \quad (\text{G11})$$

In the residual vector, μ_{θ} is the mean model, which in our case is the microlensing model. The kernel or covariance matrix K_{α} describes the correlated errors. If the errors are not correlated, K_{α} is diagonal and the likelihood reduces to the familiar form

$$\begin{aligned} \log \mathcal{L}(\mathbf{y}|\theta) &= -\frac{1}{2} \sum_i \left(\log[2\pi\sigma_i^2] + \frac{(y_i - \mu_{\theta}(t_i))^2}{\sigma_i^2} \right) \\ &= -\frac{1}{2} \sum_i \log[2\pi\sigma_i^2] - \frac{1}{2} \chi^2, \end{aligned} \quad (\text{G12})$$

where σ_i is the uncertainty on data point y_i and χ^2 is the “goodness of fit”.

Following Golovich et al. (2020), a damped driven simple harmonic oscillator (DDSHO) kernel κ_{DDSHO} added to a Matérn-3/2 kernel $\kappa_{M3/2}$ is used to model the correlated noise in the photometric microlensing survey lightcurves. Both these kernels are stationary, as they are a function of the differences of the times only:

$$\tau_{ij} = |t_i - t_j|. \quad (\text{G13})$$

The kernel is given by

$$K_{\alpha}(\tau_{ij}) = \kappa_{DDSHO}(\tau_{ij}) + \kappa_{M3/2}(\tau_{ij}) + \delta_{ij}\sigma_i^2. \quad (\text{G14})$$

Qualitatively, the DDSHO kernel models smooth variations, while the Matérn-3/2 captures more irregular variations.

The DDSHO kernel is given by

$$\kappa_{DDSHO}(\tau_{ij}) = S_0 \omega_0 e^{-\omega_0 \tau_{ij} / \sqrt{2}} \cos \left(\frac{\omega_0 \tau_{ij}}{\sqrt{2}} - \frac{\pi}{4} \right) \quad (\text{G15})$$

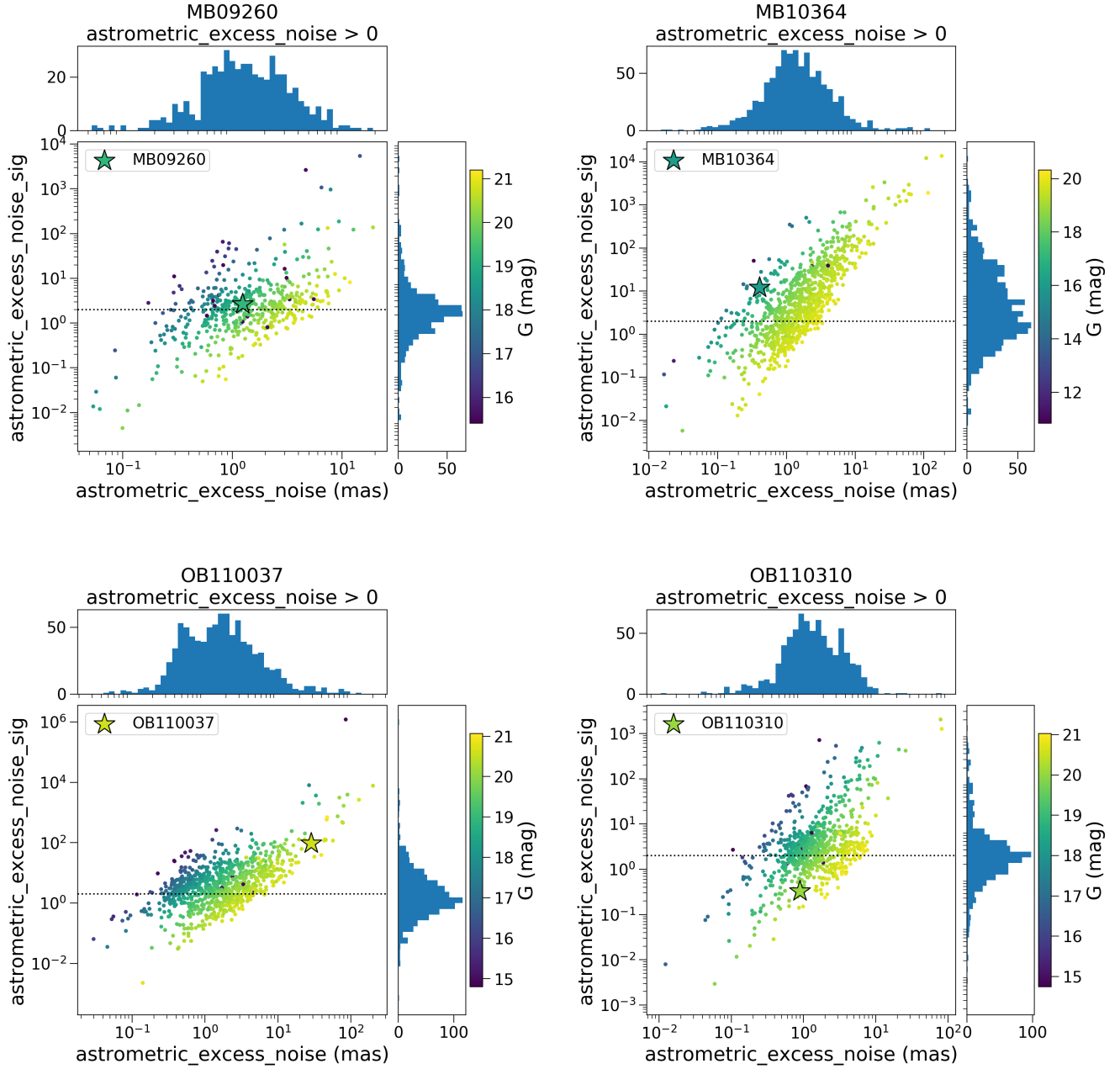


Figure 28. Astrometric excess noise vs. astrometric excess noise significance as a function of G magnitude, for sources with non-zero astrometric excess noise in the 1 deg^2 fields surrounding the microlensing targets found in Gaia. The targets are marked as stars; OB110037 is not marked as it has astrometric excess noise 0.

where S_0 controls the amplitude of the deviation from the mean model and ω_0 controls the variation frequency. This kernel has been used in asteroseismic modeling (Li et al. (2019) and references therein).

The Matérn-3/2 kernel is given by

$$\kappa_{M3/2}(\tau_{ij}) = \sigma^2 e^{-\sqrt{3}\tau_{ij}/\rho} \left(1 + \frac{\sqrt{3}\tau_{ij}}{\rho}\right) \quad (\text{G16})$$

where σ determines the amount of deviation allowed from the mean model, and ρ is the characteristic coherence scale. The Matérn-3/2 kernel has been used to model correlated noise in the lightcurves of transiting and eclipsing exoplanets (Gibson et al. 2013; Evans et al. 2015), and in particular is appropriate for modeling non-smooth behaviors (Gilbertson et al. 2020). For numerical reasons (see §4 of Foreman-Mackey et al. 2017), the Matérn-3/2 kernel is approximated

$$\kappa_{M3/2}(\tau_{ij}) = \sigma^2 \left[\left(1 + \frac{1}{\epsilon}\right) e^{-\sqrt{3}(1-\epsilon)\tau_{ij}/\rho} \left(1 - \frac{1}{\epsilon}\right) e^{-\sqrt{3}(1+\epsilon)\tau_{ij}/\rho} \right] \quad (\text{G17})$$

In the limit $\epsilon \rightarrow 0$, this is exactly the Matérn-3/2 kernel. We implement the approximation with $\epsilon = 0.01$.

The ground-based OGLE and MOA photometry are fit using the Gaussian likelihood with a full covariance matrix (Equation G10). The HST photometry and astrometry are fit using the Gaussian likelihood assuming a diagonal covariance matrix (Equation G12).

Note for MB10364, instead of fitting the MOA lightcurve using a GP, we instead fit an additive error on the ground-based photometry. During nested sampling, the GP showed some numerical instability.

H. PRIORS

The distributions for the priors π are described in this sections. $\mathcal{N}(\mu, \sigma)$ denotes a normal distribution with mean μ and standard deviation σ . $\mathcal{N}_T(\mu, \sigma, l_\sigma, u_\sigma)$ denotes a normal distribution with a low end truncation at $\mu + \sigma l_\sigma$ and a high end truncation at $\mu + \sigma u_\sigma$. $\mathcal{U}(a, b)$ denotes a uniform distribution from a to b . $\Gamma^{-1}(\alpha, \beta)$ is the inverse gamma distribution

$$\Gamma^{-1}(x; \alpha, \beta) = \frac{\beta^\alpha}{\Gamma(\alpha)} x^{-\alpha-1} \exp[-\beta/x]. \quad (\text{H18})$$

The prior distributions for each target are summarized in Table 22.

H.1. Photometry priors

The five microlensing parameters in a PSPL with parallax fit are t_0 , u_0 , t_E , $\pi_{E,E}$, and $\pi_{E,N}$.

The prior on t_0 is a normal distribution centered on the time of peak magnification in the geocentric frame, with a spread of 75 days

$$\pi(t_0) \sim \mathcal{N}(t_{peak,\oplus}, 75 \text{ days}). \quad (\text{H19})$$

Note that the time at peak magnification in the heliocentric frame t_0 is not necessarily the same as in the geocentric frame $t_{peak,\oplus}$, hence the large amount of spread in the prior.

The prior on u_0 is a Gaussian with mean 0 and standard deviation 0.5

$$\pi(u_0) \sim \mathcal{N}(0, 0.5) \quad (\text{H20})$$

which takes into account that events with smaller $|u_0|$ are more likely to be detected, and that events with $|u_0| < 1.5$ are not robustly detectable with current ground-based surveys.²⁵

The prior on t_E is a Gaussian centered at 200 days with a large spread of $\sigma = 100$ days. The distribution is truncated at -1.8σ and 3σ (20 and 500 days, respectively):

$$\pi(t_E) \sim \mathcal{N}_T(200, 50, -1.8, 10) \text{ days}. \quad (\text{H21})$$

The priors on the microlensing parallax are estimated from the population of bulge microlensing events from the PopSyCLE simulation:

$$\pi(\pi_{E,E}) \sim \mathcal{N}(-0.02, 0.12) \quad (\text{H22})$$

$$\pi(\pi_{E,N}) \sim \mathcal{N}(-0.03, 0.13). \quad (\text{H23})$$

For each dataset filter, b_{SFF} and m_{base} are also fit. For the ground-based photometry, we use a prior

$$b_{SFF,ground} \sim \mathcal{U}(0, 1.1) \quad (\text{H24})$$

where the negative blend flux implied by $b_{SFF} > 1$ allows for some extra noise such as imperfect background subtraction. Similarly for the HST astrometry, we use a uniform prior on b_{SFF}

$$b_{SFF,HST} \sim \mathcal{U}(0, 1.05). \quad (\text{H25})$$

m_{base} is a normal distribution

$$m_{base} \sim \mathcal{N}(\bar{m}_{base}, \sigma_{\bar{m}_{base}}) \quad (\text{H26})$$

where \bar{m}_{base} is the average magnitude during the unmagnified seasons, weighted by the measurement uncertainties, and $\sigma_{\bar{m}_{base}}$ is 0.1 for OGLE, 0.2 for MOA, and 0.05 for HST.

²⁵ $|u_0| = 1.5$ corresponds to a brightening of no more than around 0.1 mag. When selecting microlensing events, those with a brightening less than 0.1 mag are generally excluded in survey samples to prevent contamination from low-amplitude variables (e.g. Mróz et al. (2019)).

Table 22. Priors

Parameter	MB09260	MB10364	OB110037	OB110310	OB110462 DW	OB110462 EW
t_0 (MJD)	$\mathcal{N}(55110, 75)$	$\mathcal{N}(55460, 75)$	$\mathcal{N}(55805, 75)$	$\mathcal{N}(55810, 75)$	$\mathcal{N}(55770, 75)$	$\mathcal{N}(55770, 75)$
u_0	$\mathcal{N}(0, 0.5)$	"	"	"	"	"
t_E (days)	$\mathcal{N}_T(200, 100, -1.8, 3)$	"	"	"	"	"
$\pi_{E,E}$	$\mathcal{N}(-0.02, 0.12)$	"	"	"	"	"
$\pi_{E,N}$	$\mathcal{N}(-0.03, 0.13)$	"	"	"	"	"
$m_{base,O/M}$ (mag)	$\mathcal{N}(17.43, 0.2)$	$\mathcal{N}(15.02, 0.2)$	$\mathcal{N}(16.15, 0.1)$	$\mathcal{N}(18.41, 0.1)$	$\mathcal{N}(16.41, 0.1)$	$\mathcal{N}(16.41, 0.1)$
$b_{SFF,O/M}$	$\mathcal{U}(0, 1.1)$	"	"	"	"	"
$m_{base,H8}$ (mag)	$\mathcal{N}(17.83, 0.05)$	$\mathcal{N}(15.32, 0.05)$	$\mathcal{N}(16.33, 0.05)$	$\mathcal{N}(18.61, 0.05)$	$\mathcal{N}(19.85, 0.05)$	$\mathcal{N}(19.85, 0.05)$
$b_{SFF,H8}$	$\mathcal{U}(0, 1.05)$	"	"	"	"	"
$m_{base,H6}$ (mag)	$\mathcal{N}(20.74, 0.05)$	$\mathcal{N}(16.50, 0.05)$	$\mathcal{N}(18.33, 0.05)$	$\mathcal{N}(21.34, 0.05)$	$\mathcal{N}(22.03, 0.05)$	$\mathcal{N}(22.03, 0.05)$
$b_{SFF,H6}$	$\mathcal{U}(0, 1.05)$	"	"	"	"	"
$\log \sigma_{0,O/M}$ (mag)	$\mathcal{N}(0, 5)$	"	"	"	—	—
$\rho_{O/M}$ (days)	$\Gamma^{-1}(0.448, 0.063)$	$\Gamma^{-1}(0.448, 0.113)$	$\Gamma^{-1}(0.473, 0.162)$	$\Gamma^{-1}(0.527, 0.450)$	—	—
$\log \omega_{0,O/M}^4 S_{0,O/M}$ (mag ² days ⁻³)	$\mathcal{N}(3.53e - 04, 5)$	$\mathcal{N}(8.41e - 06, 5)$	$\mathcal{N}(3.60e - 05, 5)$	$\mathcal{N}(1.02e - 03, 5)$	—	—
$\log \omega_{0,O/M}$ (days ⁻¹)	$\mathcal{N}(0, 5)$	"	"	"	—	—
$\log_{10}(\theta_E)$ (mas)	$\mathcal{N}(-0.2, 0.3)$	"	"	"	$\mathcal{N}(0.5, 0)$	$\mathcal{N}(0.5, 0)$
π_S (mas)	$\mathcal{N}_T(0.1126, 0.0213, -2.94, 90)$	"	"	"	"	"
$x_{S0,E}$ (arcsec)	$\mathcal{U}(0.213, 0.250)$	$\mathcal{U}(0.086, 0.158)$	$\mathcal{U}(-0.034, 0.091)$	$\mathcal{U}(-0.108, -0.103)$	$\mathcal{U}(0.227, 0.233)$	$\mathcal{U}(0.227, 0.233)$
$x_{S0,N}$ (arcsec)	$\mathcal{U}(-0.697, -0.683)$	$\mathcal{U}(-0.096, -0.068)$	$\mathcal{U}(-0.122, -0.104)$	$\mathcal{U}(-0.228, -0.154)$	$\mathcal{U}(-0.235, -0.183)$	$\mathcal{U}(-0.235, -0.183)$
$\mu_{S,E}$ (mas/yr)	$\mathcal{U}(-5.96, 1.12)$	$\mathcal{U}(-7.93, -1.78)$	$\mathcal{U}(0.87, 8.05)$	$\mathcal{U}(-1.30, 0.95)$	$\mathcal{U}(-4.67, 4.82)$	$\mathcal{U}(-4.67, 4.82)$
$\mu_{S,N}$ (mas/yr)	$\mathcal{U}(-2.37, 4.17)$	$\mathcal{U}(-7.28, 3.41)$	$\mathcal{U}(-1.67, 2.94)$	$\mathcal{U}(-4.55, -0.49)$	$\mathcal{U}(-3.44, 5.84)$	$\mathcal{U}(-3.44, 5.84)$

NOTE— For definitions of the different variables, see Appendix H. There are two fits for OB110462 depending on the likelihood used, “equal weighting” (OB110462 EW) or “default weighting” (OB110462 DW). See §4.3 for details.

H.2. Gaussian Process hyperparameter priors

The ground-based photometry includes correlated noise we fit. We follow a very similar parametrization to Golovich et al. (2020) for the GP priors. The main difference is that fit in magnitude space instead of flux space, and so our priors are also in magnitudes instead of fluxes.

For σ , we use the prior

$$\log(\sigma/\text{mag}) \sim \mathcal{N}(0, 5) \quad (\text{H27})$$

which allows a wide range of lightcurve amplitude variability.

For ρ , we use the prior

$$\rho \sim \Gamma^{-1}(a, b) \quad (\text{H28})$$

where a and b are the constants that satisfy the relation

$$0.01 = \int_0^{\text{med}(\Delta t)} \Gamma^{-1}(x; a, b) dx \quad (\text{H29})$$

$$0.01 = 1 - \int_0^{\Delta T} \Gamma^{-1}(x; a, b) dx \quad (\text{H30})$$

where $\text{med}(\Delta t)$ is the median duration between observations and ΔT is the duration of full dataset. This helps

suppress values at extremely short or long timescales that might lead to ill-behaved models.²⁶

For S_0 and ω_0 we use the priors

$$\log S_0 \omega_0^4 \sim \mathcal{N}(\text{med}(\sigma_m^2), 5) \quad (\text{H31})$$

$$\log \omega_0 \sim \mathcal{N}(0, 5). \quad (\text{H32})$$

H.3. Astrometry priors

The prior on the Einstein radius θ_E is a lognormal distribution estimated from PopSyCLE for events with $t_E > 50$ or $t_E > 120$ days as

$$\pi(\log_{10}(\theta_E/\text{mas})) \sim \mathcal{N}(-0.2, 0.3) \quad (\text{H33})$$

$$\pi(\log_{10}(\theta_E/\text{mas})) \sim \mathcal{N}(0, 0.5), \quad (\text{H34})$$

respectively. We use the prior from $t_E > 120$ days for OB110462 and $t_E > 50$ days for the other 4 targets.

The prior on the source parallax π_S is estimated from the population of bulge microlensing events from the PopSyCLE simulation

$$\pi(\pi_S) \sim \mathcal{N}_T(0.1126, 0.0213, -2.9390, 90.0) \text{ mas} \quad (\text{H35})$$

which corresponds to source distances ranging from 0.5 to 20 kpc.

²⁶ See betanalpha.github.io/assets/case_studies/gaussian_processes

The prior on the source proper motion $\mu_{S,E}$ and $\mu_{S,N}$ are uniform distributions

$$\pi(\mu_{S,E}) \sim \mathcal{U}(\bar{\mu}_{S,E} - f\sigma_{\bar{\mu}_{S,E}}, \bar{\mu}_{S,E} + f\sigma_{\bar{\mu}_{S,E}}) \quad (\text{H36})$$

$$\pi(\mu_{S,N}) \sim \mathcal{U}(\bar{\mu}_{S,N} - f\sigma_{\bar{\mu}_{S,N}}, \bar{\mu}_{S,N} + f\sigma_{\bar{\mu}_{S,N}}) \quad (\text{H37})$$

where $\bar{\mu}_{S,E}$, $\bar{\mu}_{S,N}$ are the proper motions inferred from assuming straight-line motion (no parallax) from the F814W data, $\sigma_{\bar{\mu}_{S,E}}$, $\sigma_{\bar{\mu}_{S,N}}$ are the uncertainties to that fit, and f is an inflation factor. To allow a wide range of proper motions we use $f = 100$.

The prior on the source position at t_0 , $x_{0,S,E}$ and $x_{0,S,N}$, is

$$\pi(x_{0,S,E}) \sim \mathcal{U}(\min(x_E) - f\sigma_{x_E}, \max(x_E) + f\sigma_{x_E}) \quad (\text{H38})$$

$$\pi(x_{0,S,N}) \sim \mathcal{U}(\min(x_N) - f\sigma_{x_N}, \max(x_N) + f\sigma_{x_N}) \quad (\text{H39})$$

where x_E , x_N are the positions in the F814W data of the target, σ_{x_E} , σ_{x_N} is the standard deviation, and f is an inflation factor. We use $f = 5$.

I. ASTROMETRIC COLOR ANALYSIS

There are differences between the F814W and F606W astrometry. Here we illustrate with the observations of the OB110462 field only; however, all 5 fields show differences in the astrometry.

With regards to the systematic offset for OB110462, we cannot provide an explanation for it, either astrophysical or detector. We consider several ways to measure the total offset across all epochs. \overline{dx} is the average of the offsets in RA across all epochs for a particular star, and can be thought of measuring the amount of translation between F814W and F606W. $|\overline{dx}|$ is the average of the magnitude of the offsets in RA across all epochs for a particular star, and can be thought of measuring the absolute amount of translation between F814W and F606W. $|\overline{dx}|$ is the absolute value of the average of the magnitude of the offsets in RA across all epochs for a particular star, and can be thought of as measuring the total amount of deviation between F814W and F606W. Note that $|\overline{dx}|$ is distinct from $\overline{|dx|}$. The definitions for \overline{dy} , $|\overline{dy}|$, and $\overline{|dy|}$ are analogous, except they are the offsets in Dec. We also consider these quantities in units of sigma, where the differences in each epoch dx_i and dy_i are normalized by the positional uncertainties $\sigma_{x,i}$ and $\sigma_{y,i}$.

In Figure 29, we show the distributions of these quantities as a function of magnitude for stars within 30'' of the target. OB110462, while not falling in the bulk of the distribution, is not an extreme outlier. Considering how large the variation in positional differences is, especially for fainter stars, this seems well within the other positions. Hence we apply the offset for modeling and assume it is some type of systematic offset to be corrected empirically.

REFERENCES

- Abbott, B. P., Abbott, R., Abbott, T. D., et al. 2017, ApJL, 851, L16, doi: [10.3847/2041-8213/aa9a35](https://doi.org/10.3847/2041-8213/aa9a35)
- . 2020a, ApJL, 892, L3, doi: [10.3847/2041-8213/ab75f5](https://doi.org/10.3847/2041-8213/ab75f5)
- Abbott, R., Abbott, T. D., Abraham, S., et al. 2020b, ApJL, 896, L44, doi: [10.3847/2041-8213/ab960f](https://doi.org/10.3847/2041-8213/ab960f)
- Abdurrahman, F. N., Stephens, H. F., & Lu, J. R. 2021, ApJ, 912, 146, doi: [10.3847/1538-4357/abee83](https://doi.org/10.3847/1538-4357/abee83)
- Agol, E., & Kamionkowski, M. 2002, MNRAS, 334, 553, doi: [10.1046/j.1365-8711.2002.05523.x](https://doi.org/10.1046/j.1365-8711.2002.05523.x)
- Agol, E., Kamionkowski, M., Koopmans, L. V. E., & Blandford, R. D. 2002, ApJL, 576, L131, doi: [10.1086/343758](https://doi.org/10.1086/343758)
- Anderson, J. 2016, Empirical Models for the WFC3/IR PSF, Space Telescope WFC Instrument Science Report
- Anderson, J., & King, I. R. 2006, PSFs, Photometry, and Astronomy for the ACS/WFC, Instrument Science Report ACS 2006-01
- Anderson, J., Sarajedini, A., Bedin, L. R., et al. 2008, AJ, 135, 2055, doi: [10.1088/0004-6256/135/6/2055](https://doi.org/10.1088/0004-6256/135/6/2055)
- Astropy Collaboration, Robitaille, T. P., Tollerud, E. J., et al. 2013, A&A, 558, A33, doi: [10.1051/0004-6361/201322068](https://doi.org/10.1051/0004-6361/201322068)
- Astropy Collaboration, Price-Whelan, A. M., Sipőcz, B. M., et al. 2018, AJ, 156, 123, doi: [10.3847/1538-3881/aabc4f](https://doi.org/10.3847/1538-3881/aabc4f)
- Baraffe, I., Homeier, D., Allard, F., & Chabrier, G. 2015, A&A, 577, A42, doi: [10.1051/0004-6361/201425481](https://doi.org/10.1051/0004-6361/201425481)
- Batista, V., Beaulieu, J. P., Bennett, D. P., et al. 2015, ApJ, 808, 170, doi: [10.1088/0004-637X/808/2/170](https://doi.org/10.1088/0004-637X/808/2/170)
- Belczynski, K., Sadowski, A., & Rasio, F. A. 2004, ApJ, 611, 1068, doi: [10.1086/422191](https://doi.org/10.1086/422191)
- Bellini, A., Anderson, J., & Bedin, L. R. 2011, PASP, 123, 622, doi: [10.1086/659878](https://doi.org/10.1086/659878)
- Bellini, A., Libralato, M., Bedin, L. R., et al. 2018, ApJ, 853, 86, doi: [10.3847/1538-4357/aaa3ec](https://doi.org/10.3847/1538-4357/aaa3ec)
- Bennett, D. P., Becker, A. C., Quinn, J. L., et al. 2002, ApJ, 579, 639, doi: [10.1086/342225](https://doi.org/10.1086/342225)
- Bennett, D. P., Bhattacharya, A., Anderson, J., et al. 2015, ApJ, 808, 169, doi: [10.1088/0004-637X/808/2/169](https://doi.org/10.1088/0004-637X/808/2/169)

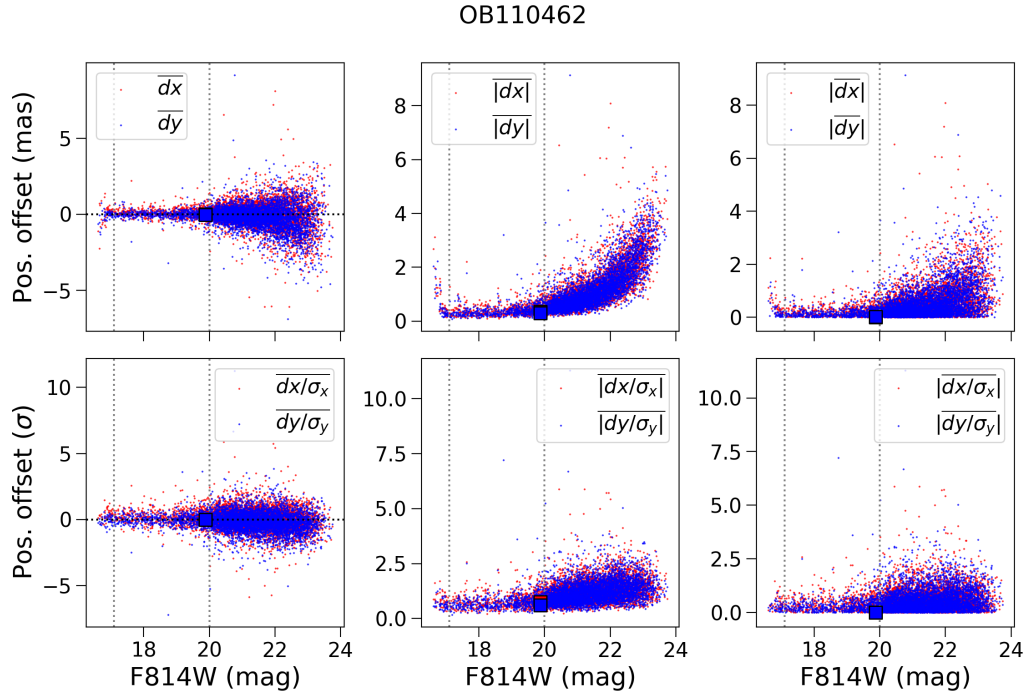


Figure 29. Positional offsets between F814W and F606W, aggregated across all epochs. Definitions are given in text of Appendix I. The squares mark OB110462. The dashed lines indicate the magnitude range of the reference stars.

- Bond, I. A., Abe, F., Dodd, R. J., et al. 2001, *MNRAS*, 327, 868, doi: [10.1046/j.1365-8711.2001.04776.x](https://doi.org/10.1046/j.1365-8711.2001.04776.x)
- Buchner, J., Georgakakis, A., Nandra, K., et al. 2014, *A&A*, 564, A125, doi: [10.1051/0004-6361/201322971](https://doi.org/10.1051/0004-6361/201322971)
- Castelli, F., & Kurucz, R. L. 2004, *ArXiv Astrophysics e-prints*
- Choi, J., Dotter, A., Conroy, C., et al. 2016, *ApJ*, 823, 102, doi: [10.3847/0004-637X/823/2/102](https://doi.org/10.3847/0004-637X/823/2/102)
- Corral-Santana, J. M., Casares, J., Muñoz-Darias, T., et al. 2016, *A&A*, 587, A61, doi: [10.1051/0004-6361/201527130](https://doi.org/10.1051/0004-6361/201527130)
- Damineli, A., Almeida, L. A., Blum, R. D., et al. 2016, *MNRAS*, 463, 2653, doi: [10.1093/mnras/stw2122](https://doi.org/10.1093/mnras/stw2122)
- Eddington, A. S. 1919, *The Observatory*, 42, 119
- Evans, I. N., Allen, C., Anderson, C. S., et al. 2019a, in *American Astronomical Society Meeting Abstracts*, Vol. 233, *American Astronomical Society Meeting Abstracts #233*, 379.01
- Evans, I. N., Allen, C., Anderson, C. S., et al. 2019b, in *AAS/High Energy Astrophysics Division*, Vol. 17, *AAS/High Energy Astrophysics Division*, 114.01
- Evans, P. A., Page, K. L., Osborne, J. P., et al. 2020, *ApJS*, 247, 54, doi: [10.3847/1538-4365/ab7db9](https://doi.org/10.3847/1538-4365/ab7db9)
- Evans, T. M., Aigrain, S., Gibson, N., et al. 2015, *MNRAS*, 451, 680, doi: [10.1093/mnras/stv910](https://doi.org/10.1093/mnras/stv910)
- Fabricius, C., Luri, X., Arenou, F., et al. 2021, *A&A*, 649, A5, doi: [10.1051/0004-6361/202039834](https://doi.org/10.1051/0004-6361/202039834)
- Fender, R. P., Maccarone, T. J., & Heywood, I. 2013, *MNRAS*, 430, 1538, doi: [10.1093/mnras/sts688](https://doi.org/10.1093/mnras/sts688)
- Feroz, F., Hobson, M. P., & Bridges, M. 2009, *MNRAS*, 398, 1601, doi: [10.1111/j.1365-2966.2009.14548.x](https://doi.org/10.1111/j.1365-2966.2009.14548.x)
- Foreman-Mackey, D., Agol, E., Ambikasaran, S., & Angus, R. 2017, *AJ*, 154, 220, doi: [10.3847/1538-3881/aa9332](https://doi.org/10.3847/1538-3881/aa9332)
- Gaia Collaboration, Brown, A. G. A., Vallenari, A., et al. 2020, *arXiv e-prints*, arXiv:2012.01533, <https://arxiv.org/abs/2012.01533>
- Gaia Collaboration, Prusti, T., de Bruijne, J. H. J., et al. 2016, *A&A*, 595, A1, doi: [10.1051/0004-6361/201629272](https://doi.org/10.1051/0004-6361/201629272)
- Gennaro, M. e. a. 2018, *WFC3 Data Handbook*, Version 4.0, Baltimore: STScI
- Gibson, N. P., Aigrain, S., Barstow, J. K., et al. 2013, *MNRAS*, 428, 3680, doi: [10.1093/mnras/sts307](https://doi.org/10.1093/mnras/sts307)
- Gilbertson, C., Ford, E. B., Jones, D. E., & Stenning, D. C. 2020, *arXiv e-prints*, arXiv:2009.01085, <https://arxiv.org/abs/2009.01085>
- Golovich, N., Dawson, W. A., Bartolić, F., et al. 2020, *arXiv e-prints*, arXiv:2009.07927, <https://arxiv.org/abs/2009.07927>
- Gould, A. 2000, *ApJ*, 535, 928, doi: [10.1086/308865](https://doi.org/10.1086/308865)
- . 2004, *ApJ*, 606, 319, doi: [10.1086/382782](https://doi.org/10.1086/382782)
- Green, G. 2018, *The Journal of Open Source Software*, 3, 695, doi: [10.21105/joss.00695](https://doi.org/10.21105/joss.00695)
- Griest, K., Alcock, C., Axelrod, T. S., et al. 1991, *ApJL*, 372, L79, doi: [10.1086/186028](https://doi.org/10.1086/186028)
- Groth, E. J. 1986, *AJ*, 91, 1244, doi: [10.1086/114099](https://doi.org/10.1086/114099)
- Hearnshaw, J. B., Abe, F., Bond, I. A., et al. 2006, in *The 9th Asian-Pacific Regional IAU Meeting*, ed. W. Sutantyo, P. W. Premadi, P. Mahasena, T. Hidayat, & S. Mineshige, 272, <https://arxiv.org/abs/astro-ph/0509420>
- Hog, E., Novikov, I. D., & Polnarev, A. G. 1995, *A&A*, 294, 287
- Hosek, Matthew W., J., Lu, J. R., Lam, C. Y., et al. 2020, *AJ*, 160, 143, doi: [10.3847/1538-3881/aba533](https://doi.org/10.3847/1538-3881/aba533)
- Hosek, Jr., M. W., Lu, J. R., Anderson, J., et al. 2015, *ApJ*, 813, 27, doi: [10.1088/0004-637X/813/1/27](https://doi.org/10.1088/0004-637X/813/1/27)
- Hunter, J. D. 2007, *Computing in Science & Engineering*, 9, 90, doi: [10.1109/MCSE.2007.55](https://doi.org/10.1109/MCSE.2007.55)
- Husser, T.-O., Wende-von Berg, S., Dreizler, S., et al. 2013, *A&A*, 553, A6, doi: [10.1051/0004-6361/201219058](https://doi.org/10.1051/0004-6361/201219058)
- Jayasinghe, T., Stanek, K. Z., Thompson, T. A., et al. 2021, *MNRAS*, 504, 2577, doi: [10.1093/mnras/stab907](https://doi.org/10.1093/mnras/stab907)
- Jonker, P. G., Kaur, K., Stone, N., & Torres, M. A. P. 2021, *arXiv e-prints*, arXiv:2104.03596, <https://arxiv.org/abs/2104.03596>
- Kains, N., Calamida, A., Sahu, K. C., et al. 2017, *ApJ*, 843, 145, doi: [10.3847/1538-4357/aa78eb](https://doi.org/10.3847/1538-4357/aa78eb)
- Kim, S.-L., Lee, C.-U., Park, B.-G., et al. 2016, *Journal of Korean Astronomical Society*, 49, 37, doi: [10.5303/JKAS.2016.49.1.037](https://doi.org/10.5303/JKAS.2016.49.1.037)
- Koester, D. 2010, *Mem. Soc. Astron. Italiana*, 81, 921
- Kreidberg, L., Bailyn, C. D., Farr, W. M., & Kalogera, V. 2012, *ApJ*, 757, 36, doi: [10.1088/0004-637X/757/1/36](https://doi.org/10.1088/0004-637X/757/1/36)
- Kroupa, P. 2001, *MNRAS*, 322, 231, doi: [10.1046/j.1365-8711.2001.04022.x](https://doi.org/10.1046/j.1365-8711.2001.04022.x)
- Kuhn, B., & Anderson, J. 2021, *WFC3/UVIS: New FLC External CTE Monitoring 2009-2020*, Space Telescope WFC Instrument Science Report
- Lam, C., & Lu, J. R. 2021a, First detection of an isolated stellar mass black hole with astrometric microlensing, *HST Proposal*
- . 2021b, First detection of an isolated stellar mass black hole with astrometric microlensing, *HST Proposal*
- Lam, C. Y., Lu, J. R., Hosek, Matthew W., J., Dawson, W. A., & Golovich, N. R. 2020, *ApJ*, 889, 31, doi: [10.3847/1538-4357/ab5fd3](https://doi.org/10.3847/1538-4357/ab5fd3)
- Li, S. S., Zang, W., Udalski, A., et al. 2019, *MNRAS*, 488, 3308, doi: [10.1093/mnras/stz1873](https://doi.org/10.1093/mnras/stz1873)
- Lindgren, L., Bastian, U., Biermann, M., et al. 2021a, *A&A*, 649, A4, doi: [10.1051/0004-6361/202039653](https://doi.org/10.1051/0004-6361/202039653)

- Lindgren, L., Klioner, S. A., Hernández, J., et al. 2021b, *A&A*, 649, A2, doi: [10.1051/0004-6361/202039709](https://doi.org/10.1051/0004-6361/202039709)
- Lu, J. R., Sinukoff, E., Ofek, E. O., Udalski, A., & Kozłowski, S. 2016, *ApJ*, 830, doi: [10.3847/0004-637X/830/1/41](https://doi.org/10.3847/0004-637X/830/1/41)
- Maeda, Y., Kubota, A., Kobayashi, Y., et al. 2005, *ApJL*, 631, L65, doi: [10.1086/491698](https://doi.org/10.1086/491698)
- Manchester, R. N., Hobbs, G. B., Teoh, A., & Hobbs, M. 2005, *AJ*, 129, 1993, doi: [10.1086/428488](https://doi.org/10.1086/428488)
- Mao, S., Smith, M. C., Woźniak, P., et al. 2002, *MNRAS*, 329, 349, doi: [10.1046/j.1365-8711.2002.04986.x](https://doi.org/10.1046/j.1365-8711.2002.04986.x)
- Marshall, D. J., Robin, A. C., Reylé, C., Schultheis, M., & Picaud, S. 2006, *A&A*, 453, 635, doi: [10.1051/0004-6361:20053842](https://doi.org/10.1051/0004-6361:20053842)
- McGill, P., Everall, A., Boubert, D., & Smith, L. C. 2020, *MNRAS*, 498, L6, doi: [10.1093/mnrasl/slaa118](https://doi.org/10.1093/mnrasl/slaa118)
- Miyamoto, M., & Yoshii, Y. 1995, *AJ*, 110, 1427, doi: [10.1086/117616](https://doi.org/10.1086/117616)
- Mróz, P., Udalski, A., Skowron, J., et al. 2019, *ApJS*, 244, 29, doi: [10.3847/1538-4365/ab426b](https://doi.org/10.3847/1538-4365/ab426b)
- Nucita, A. A., De Paolis, F., Ingrosso, G., et al. 2006, *ApJ*, 651, 1092, doi: [10.1086/507784](https://doi.org/10.1086/507784)
- Özel, F., Psaltis, D., Narayan, R., & McClintock, J. E. 2010, *ApJ*, 725, 1918, doi: [10.1088/0004-637X/725/2/1918](https://doi.org/10.1088/0004-637X/725/2/1918)
- Paczynski, B. 1986, *ApJ*, 304, 1, doi: [10.1086/164140](https://doi.org/10.1086/164140)
- . 1991, *ApJL*, 371, L63, doi: [10.1086/186003](https://doi.org/10.1086/186003)
- Penny, M. T., Gaudi, B. S., Kerins, E., et al. 2019, *ApJS*, 241, 3, doi: [10.3847/1538-4365/aaf69](https://doi.org/10.3847/1538-4365/aaf69)
- Poindexter, S., Afonso, C., Bennett, D. P., et al. 2005, *ApJ*, 633, 914, doi: [10.1086/468182](https://doi.org/10.1086/468182)
- Rasmussen, C. E., & Williams, C. K. I. 2006, *Gaussian Processes for Machine Learning*
- Robin, A. C., Reylé, C., Derrière, S., & Picaud, S. 2003, *A&A*, 409, 523, doi: [10.1051/0004-6361:20031117](https://doi.org/10.1051/0004-6361:20031117)
- Rowan, D. M., Stanek, K. Z., Jayasinghe, T., et al. 2021, *MNRAS*, 507, 104, doi: [10.1093/mnras/stab2126](https://doi.org/10.1093/mnras/stab2126)
- Rybicki, K. A., Wyrzykowski, L., Klencki, J., et al. 2018, *MNRAS*, 476, 2013, doi: [10.1093/mnras/sty356](https://doi.org/10.1093/mnras/sty356)
- Rybizki, J., Green, G., Rix, H.-W., et al. 2021, *arXiv e-prints*, arXiv:2101.11641, <https://arxiv.org/abs/2101.11641>
- Sabbi, E., Lennon, D. J., Anderson, J., et al. 2016, *ApJS*, 222, 11, doi: [10.3847/0067-0049/222/1/11](https://doi.org/10.3847/0067-0049/222/1/11)
- Sahu, K. 2009, *Detecting Isolated Black Holes through Astrometric Microlensing*, *HST Proposal*
- . 2012, *Detecting Isolated Black Holes through Astrometric Microlensing*, *HST Proposal*
- Sahu, K. C., Anderson, J., Casertano, S., et al. 2017, *Science*, 356, 1046, doi: [10.1126/science.aal2879](https://doi.org/10.1126/science.aal2879)
- Samland, M. 1998, *ApJ*, 496, 155, doi: [10.1086/305368](https://doi.org/10.1086/305368)
- Sana, H. 2017, in *The Lives and Death-Throes of Massive Stars*, ed. J. J. Eldridge, J. C. Bray, L. A. S. McClelland, & L. Xiao, Vol. 329, 110–117, doi: [10.1017/S1743921317003209](https://doi.org/10.1017/S1743921317003209)
- Sarmiento, M. H., Arévalo, M., Arviset, C., et al. 2019, in *Astronomical Society of the Pacific Conference Series*, Vol. 521, *Astronomical Data Analysis Software and Systems XXVI*, ed. M. Molinaro, K. Shortridge, & F. Pasian, 104
- Sartore, N., & Treves, A. 2010, *A&A*, 523, A33, doi: [10.1051/0004-6361/201015060](https://doi.org/10.1051/0004-6361/201015060)
- Shapiro, S. L., & Teukolsky, S. A. 1983, *Black holes, white dwarfs, and neutron stars : the physics of compact objects*
- Sharma, S., Bland-Hawthorn, J., Johnston, K. V., & Binney, J. 2011, *ApJ*, 730, 3, doi: [10.1088/0004-637X/730/1/3](https://doi.org/10.1088/0004-637X/730/1/3)
- Skilling, J. 2004, in *American Institute of Physics Conference Series*, Vol. 735, *Bayesian Inference and Maximum Entropy Methods in Science and Engineering: 24th International Workshop on Bayesian Inference and Maximum Entropy Methods in Science and Engineering*, ed. R. Fischer, R. Preuss, & U. V. Toussaint, 395–405, doi: [10.1063/1.1835238](https://doi.org/10.1063/1.1835238)
- Speagle, J. S. 2020, *MNRAS*, 493, 3132, doi: [10.1093/mnras/staa278](https://doi.org/10.1093/mnras/staa278)
- Spergel, D., Gehrels, N., Baltay, C., et al. 2015, *arXiv e-prints*, arXiv:1503.03757, <https://arxiv.org/abs/1503.03757>
- Sumi, T. 2008, in *Manchester Microlensing Conference*, ed. E. Kerins, S. Mao, N. Rattenbury, & L. Wyrzykowski, 25
- Sumi, T., Kamiya, K., Bennett, D. P., et al. 2011, *Nature*, 473, 349, doi: [10.1038/nature10092](https://doi.org/10.1038/nature10092)
- Thompson, T. A., Kochanek, C. S., Stanek, K. Z., et al. 2019, *Science*, 366, 637, doi: [10.1126/science.aau4005](https://doi.org/10.1126/science.aau4005)
- Timmes, F. X., Woosley, S. E., & Weaver, T. A. 1996, *ApJ*, 457, 834, doi: [10.1086/176778](https://doi.org/10.1086/176778)
- Tsuna, D., Kawanaka, N., & Totani, T. 2018, *MNRAS*, 477, 791, doi: [10.1093/mnras/sty699](https://doi.org/10.1093/mnras/sty699)
- Udalski, A., Szymanski, M., Kaluzny, J., et al. 1994, *AcA*, 44, 227, <https://arxiv.org/abs/astro-ph/9408026>
- Udalski, A., Szymański, M. K., & Szymański, G. 2015, *AcA*, 65, 1, <https://arxiv.org/abs/1504.05966>
- van der Walt, S., Colbert, S. C., & Varoquaux, G. 2011, *Computing in Science & Engineering*, 13, 22, doi: [10.1109/MCSE.2011.37](https://doi.org/10.1109/MCSE.2011.37)
- van Leeuwen, F., de Bruijne, J., Babusiaux, C., et al. 2021, *Gaia EDR3 documentation*, *Gaia EDR3 documentation*

- Virtanen, P., Gommers, R., Oliphant, T. E., et al. 2019, arXiv e-prints, arXiv:1907.10121.
<https://arxiv.org/abs/1907.10121>
- Walker, M. A. 1995, ApJ, 453, 37, doi: [10.1086/176367](https://doi.org/10.1086/176367)
- Wang, Y. H. 1993, Statistica Sinica, 3, 295.
<http://www.jstor.org/stable/24304959>
- WFIRST Astrometry Working Group, Sanderson, R. E., Bellini, A., et al. 2019, Journal of Astronomical Telescopes, Instruments, and Systems, 5, 044005, doi: [10.1117/1.JATIS.5.4.044005](https://doi.org/10.1117/1.JATIS.5.4.044005)
- Wiktorowicz, G., Lu, Y., Wyrzykowski, L., et al. 2020, ApJ, 905, 134, doi: [10.3847/1538-4357/abc699](https://doi.org/10.3847/1538-4357/abc699)
- Wiktorowicz, G., Wyrzykowski, L., Chruslinska, M., et al. 2019, ApJ, 885, 1, doi: [10.3847/1538-4357/ab45e6](https://doi.org/10.3847/1538-4357/ab45e6)
- Wozniak, P. R. 2000, AcA, 50, 421.
<https://arxiv.org/abs/astro-ph/0012143>
- Wyrzykowski, L., Kostrzewa-Rutkowska, Z., Skowron, J., et al. 2016, MNRAS, 458, 3012, doi: [10.1093/mnras/stw426](https://doi.org/10.1093/mnras/stw426)
- Yalinewich, A., Beniamini, P., Hotokezaka, K., & Zhu, W. 2018, MNRAS, 481, 930, doi: [10.1093/mnras/sty2327](https://doi.org/10.1093/mnras/sty2327)
- Yamaguchi, M. S., Kawanaka, N., Bulik, T., & Piran, T. 2018, ApJ, 861, 21, doi: [10.3847/1538-4357/aac5ec](https://doi.org/10.3847/1538-4357/aac5ec)
- Zurlo, A., Gratton, R., Mesa, D., et al. 2018, MNRAS, 480, 236, doi: [10.1093/mnras/sty1805](https://doi.org/10.1093/mnras/sty1805)